



**COMPUTATIONAL DESIGN OF UPPERSTAGE CHAMBER, AEROSPIKE, &
COOLING JACKET FOR DUAL-EXPANDER ROCKET ENGINE**

THESIS

David F. Martin II, 2Lt, USAF

AFIT/GAE/ENY/08-M20

**DEPARTMENT OF THE AIR FORCE
AIR UNIVERSITY
AIR FORCE INSTITUTE OF TECHNOLOGY**

Wright-Patterson Air Force Base, Ohio

APPROVED FOR PUBLIC RELEASE; DISTRIBUTION UNLIMITED

The views expressed in this thesis are those of the author and do not reflect the official policy or position of the United States Air Force, Department of Defense, or the U.S. Government.

AFIT/GAE/ENY/08-M20

**COMPUTATIONAL DESIGN OF UPPERSTAGE CHAMBER, AEROSPIKE, &
COOLING JACKET OF DUAL-EXPANDER ROCKET ENGINE**

THESIS

Presented to the Faculty

Department of ENY

Graduate School of Engineering and Management

Air Force Institute of Technology

Air University

Air Education and Training Command

In Partial Fulfillment of the Requirements for the
Degree of Master of Science in Aerospace Engineering

David F. Martin II, BS

2Lt, USAF

March 2008

APPROVED FOR PUBLIC RELEASE; DISTRIBUTION UNLIMITED

AFIT/GAE/ENY/08-M20

**COMPUTATIONAL DESIGN OF UPPERSTAGE CHAMBER, AEROSPIKE, &
COOLING JACKET OF DUAL-EXPANDER ROCKET ENGINE**

David F. Martin II, BS

2Lt, USAF

Approved:

//signed//
Richard D. Branam, Maj, USAF (Chairman)

17 Mar 08
Date

//signed//
Raymond C. Maple, Lt Col, USAF (Member)

17 Mar 08
Date

//signed//
Richard E. Huffman, Maj, USAF (Member)

17 Mar 08
Date

Acknowledgments

I would like to express my sincere appreciation to my faculty advisor, Maj Richard Branam, for his guidance and support throughout the course of this thesis effort. The insight and experience was certainly appreciated. I would also like to thank my sponsor, Mr. Michael Huggins, from the AFRL at Edwards for the support. I want to thank Capt Michael Arguello and Capt William Strain, my fellow workers, who managed to endure on this project despite themselves. I would also like to thank Thomas Lavelle at NASA Glenn for his help with NPSS. Without him the model would never have been completed. I thank Timothy O'Brien and Ronald Springer of Aerojet for their TDK and NPSS code and their help. Finally, a big thanks goes out to my family and friends who supported me through thick and thin.

David F. Martin II

Table of Contents

	Page
Table of Contents	vi
List of Figures	x
List of Tables	xii
List of Symbols	xiii
Abstract	xvi
1. Introduction	17
1.1. Motivation	17
1.2. Objectives	18
1.2.1. <i>The DEAN</i>	19
1.2.2. <i>Thrust Chamber</i>	20
1.2.3. <i>Nozzle</i>	20
1.2.4. <i>Cooling Jacket</i>	21
1.3. Preview	21
2. Background	22
2.1. Orbit Transfer Engines and Mission Requirements	22
2.1.1. <i>Baseline Engine</i>	22
2.1.2. <i>Typical Mission Requirements</i>	24
2.1.3. <i>Expander Cycles</i>	25
2.2. Thrust Chamber	26
2.2.1. <i>Rocket Engine Performance</i>	26
2.2.2. <i>Dimension of the Thrust Chamber</i>	28
2.2.3. <i>Injectors</i>	29

2.3.	Nozzle	33
2.3.1.	<i>Aerospike</i>	34
2.4.	Cooling Jacket.....	40
2.4.1.	<i>Heat Transfer</i>	40
2.4.2.	<i>Cooling Techniques</i>	43
2.4.3.	<i>Aerospike Cooling</i>	45
2.4.4.	<i>Material</i>	47
2.4.5.	<i>Aspect-Ratio</i>	48
3.	Methodology	52
3.1.	General Sizing.....	52
3.2.	Thrust Chamber	54
3.2.1.	<i>Chamber Controls</i>	54
3.2.2.	<i>Chamber Process Variables</i>	54
3.2.3.	<i>Chamber Outputs</i>	54
3.3.	Nozzle	55
3.3.1.	<i>Nozzle Controls</i>	55
3.3.2.	<i>Nozzle Process Variables</i>	55
3.3.3.	<i>Nozzle Outputs</i>	55
3.4.	Cooling Jacket.....	55
3.4.1.	<i>Cooling Jacket Controls</i>	56
3.4.2.	<i>Cooling Jacket Process Variables</i>	56
3.4.3.	<i>Cooling Jacket Outputs</i>	56

3.5.	NPSS	56
3.6.	TDK	60
3.7.	Sensitivity Analysis	61
3.8.	Beginning Frame Work.....	63
3.8.1.	<i>Cooling Channel Design</i>	64
3.8.2.	<i>Material Choice</i>	65
4.	Analysis and Results	68
4.1.	Chapter Overview	68
4.2.	Results of Simulation Scenarios	68
4.2.1.	<i>Hydrogen Cooling Jacket Results</i>	69
4.2.2.	<i>Oxygen Cooling Jacket Results</i>	73
4.2.3.	<i>Chamber/Nozzle Results</i>	76
4.2.4.	<i>TDK Nozzle</i>	77
4.3.	Investigative Objectives.....	81
4.4.	Summary	82
5.	Conclusions and Recommendations.....	84
5.1.	Chapter Overview	84
5.2.	Conclusions of Research.....	84
5.3.	Significance of Research.....	84
5.4.	Recommendations for Future Research	85
5.5.	Summary	86
Appendix A :	Lessons Learned.....	87
A.1	NPSS Lessons Learned.....	87

A.2 TDK Lessons Learned	88
Appendix B : NPSS Code	89
B.1 Final Model Code	89
B.2 Included Cooling Volume Element	105
B.3 Included Pump Element.....	114
B.4 Included Turbine Element	118
Appendix C : TDK Code	123
C.1 TDK Input for DEAN Upper Stage Engine.....	123
C.2 TDK Performance Summary for the DEAN.....	124
Appendix D : I_{sp} Calculation.....	127
Appendix E : Wall Temperatures	128
References.....	131
Vita.....	134

List of Figures

Figure	Page
Figure 1. The Dean Schematic.....	19
Figure 2. RL10B-2(with permission from Pratt & Whitney) ³	23
Figure 3. RL10B-2 Cycle Schematic (with permission from Pratt & Whitney) ³	25
Figure 4. Shear Coaxial Gas/Liquid Injector	30
Figure 5. Pintle Injector	32
Figure 6. Aerospike.....	33
Figure 7. Flow Phenomena of Plug Nozzle	35
Figure 8. Flow Phenomena of Truncated Plug Nozzle	36
Figure 9. Channel Aspect Ratio	49
Figure 10. NPSS Model Schematic	57
Figure 11. NPSS Cooling Jacket.....	59
Figure 12. Sensitivity Model.....	61
Figure 13. Initial Contour	63
Figure 14. Cooling Channel Cross-Section	64
Figure 15. Chamber/Nozzle Contour (all dimension in inches)	68
Figure 16. Hydrogen Wall Temperatures	72
Figure 17. Oxygen Wall Temperatures.....	75
Figure 18. Non-dimensional Nozzle Contour with Temperature Profile	78
Figure 19. Truncated Nozzle.....	79
Figure 20. Nozzle Contour.....	80

Figure 21. The DEAN.....	81
--------------------------	----

List of Tables

Table	Page
Table 1. Average Price per Pound of Launch Vehicles	18
Table 2. Influence on c^* ⁷	27
Table 3. Stepped Channel vs. Constant Cross-Section Channel ⁴²	51
Table 4. Chosen Parameters.....	52
Table 5. Hydrogen Sensitivity Analysis	62
Table 6. Oxygen Sensitivity Analysis.....	62
Table 7. Material Thermal Properties ¹⁹	65
Table 8. Structural Materials.....	66
Table 9. Oxygen Compatibility.....	67
Table 10. Hydrogen Channel Dimensions	70
Table 11. Hydrogen Mach Numbers.....	70
Table 12. Hydrogen Flow Temperature.....	73
Table 13. Oxygen Channel Dimensions	74
Table 14. Oxygen Mach Numbers	74
Table 15. Oxygen Flow Temperature	76
Table 16. Chamber Performance	77
Table 17. TDK Properties.....	78
Table 18. Truncation of Nozzle	79
Table 19 Hydrogen Wall Materials.....	128
Table 20 Oxygen Wall Materials.....	129

List of Symbols

Symbol

a	speed of sound, channel half spacing
A_c	combustion chamber area, cold side area
A_e	exit area
A_H	hot side area
A_t	throat area
AR	aspect ratio
A^*	characteristic area
BF	burn factor
Btu	British thermal unit
c^*	characteristic velocity
C	constant
C_g	throat region correlation coefficient
C_T	thrust coefficient
cal	calorie
CFD	computational fluid dynamics
CH_4	methane
DEAN	Dual Expander Aerospike Nozzle engine
dT/dx	derivative of the temperature with respect to position
EELV	Evolved Expendable Launch Vehicle
FESTIP	Future European Space Transportation Investigations Program
F_g	thrust
ft	foot
F_{tu}	ultimate tensile strength
GEO	geostationary orbit
gmole	6.02252×10^{23} molecules
g_0	acceleration due to gravity
GTO	geo transfer orbit
GUI	graphical user interface
h	channel height , convective heat transfer coefficient
h_c	coolant convective heat transfer coefficient
h_H	hot side convective heat transfer coefficient
ΔH_f^0	heat of oxidation
IHPRPT	Integrated High Payoff Rocket Propulsion Technology initiative
in	inch
I_{sp}	specific impulse
k	thermal conductivity
K	Kelvin
Kg	kilograms
L	length
L^*	characteristic length

lbf	ponds force
lbm	pounds mass
LEO	low earth orbit
LH ₂	liquid hydrogen
LO ₂ , LOX	liquid oxygen
m	meter
\dot{m}	mass flow rate
\overline{M}	molecular weight
M	Mach number
M _b	burnout mass
M _e	exit Mach number
M ₀	initial mass
min	minute
mm	millimeter
N	Newton's
NASA	National Air and Space Association
NIST	National Institute of Standards and Technology
NPSS TM	Numerical Propulsion System Simulation
Nu	Nusselt number
O/F	oxidizer-to-fuel ratio
P ₀	total chamber pressure
Pa	Pascal
P _a	ambient
P _b	burst pressure
P _c	chamber pressure
P _e	exit pressure
PR	pressure ratio
Pr*	reference Prandtl number
psi	pounds per square inch
q''	heat flux
q _x	heat rate x-direction
Q	parameter
r	radius
R	Rankine
R*	throat radius
\overline{R}	Universal gas constant
r _c	chamber radius
Re* _d	reference Reynolds's number
RP1	hydrocarbon fuel
s, sec	seconds
SSME	space shuttle main engine
St*	reference Stewart number
t	thickness
T _C	cold side temperature

TDK 04 TM	Two-dimensional kinematics
T_H	hot side temperature
T_0	total temperature in the chamber
T_s	temperature of the surface
t_w	wall thickness
T_{wall}	temperature of the wall
T_∞	temperature of the fluid
Δu	change in velocity
VCCW	vortex combustion cold-wall chamber
V_c	chamber volume
w	channel half width
W	watts
X	nozzle length
α	thermal diffusivity
γ	ratio of specific heat
Δ	change in
ε	expansion ratio
λ	nozzle efficiency

Abstract

To increase the performance of the current US satellite launch capability, new rocket designs must be undertaken. One concept that has been around since the 50s but yet to be utilized on a launch platform is the aerospike, or plug nozzle. The aerospike nozzle concept demonstrates globally better performance compared to a conventional bell nozzle, since the expansion of the jet is not bounded by a wall and therefore can adjust to the environment by changing the outer jet boundary. A dual-expander aerospike nozzle (DEAN) rocket concept would exceed the Integrated High Payoff Rocket Propulsion Technology initiative (IHPRPT) phase three goals. This document covers the design of the chamber and nozzle of the DEAN. The validation of the design of the DEAN are based on the model in Numerical Propulsion System Simulation (NPSSTM), added with the nozzle design from Two-Dimensional Kinematics (TDK 04TM). The result is a rocket engine that produces 57,231 lbf (254.5 kN) of thrust at an I_{sp} of 472 s. Additionally, the oxygen wall is made of silicon carbide, with a melting point of 5580 R (3100 K), and has a maximum temperature at the throat of 1625 R (902 K). The hydrogen side is made of copper, with a melting point of 2444 R (1358 K), and has a maximum wall temperature of 1224 R (680 K) at the throat. Based on these result, future investigation into this design is merited since it has the potential to save \$19 million in the cost to launch a satellite. NPSS proved to be a powerful tool in the development of rocket engines. TDK, however, was left wanting in the area of aerospike design.

COMPUTATIONAL DESIGN OF UPPERSTAGE CHAMBER, AEROSPIKE, & COOLING JACKET OF DUAL-EXPANDER ROCKET ENGINE

1. Introduction

Engineers live to design at the edge of what is possible. Since the beginning of rocketry, the bell nozzle has dominated the rocket motor design. Now the time is right to revive an old concept and couple it with new technology to break the bell's dominance. The concept is the aerospike nozzle and the dual-expander aerospike nozzle, or DEAN, is the design that will usher in an age of improved performance and cost in the space launch arena.

1.1. Motivation

The Integrated High Payoff Rocket Propulsion Technology initiative (IHDRPT)¹ is a joint government and industry effort focused on developing affordable technologies for reach capability, sustainable strategic missiles, long life or increased maneuverability spacecraft capability and high performance tactical missile capability. The objectives for the boost and orbit transfer part is to increase the specific impulse (I_{sp}), increase the thrust-to-weight ratio or the mass fraction, reduce the failure rate, and increase the reusability. All of this will lead to the end goal of a reduction in the cost of launching satellites. The goals of phase III are to increase the I_{sp} by 26 seconds and improve thrust-to-weight by 100%. The result of the program should be an increase in payload of 22% and 95% and a reduction in cost of 33% and 82% for expendable and reusable launch vehicles, respectively.

One way to determine the cost of a launch is per pound. Table 1 shows the estimated average cost per pound.

Table 1. Average Price per Pound of Launch Vehicles²

Vehicle Class	LEO		GTO	
	Western	Non-Western	Western	Non-Western
Small	\$8,445	\$3,208	\$18,841	N/A
Medium	\$4,994	\$2,404	\$12,133	\$9,843
Heavy	\$4,440	\$1,946	\$17,032	\$6,967

In a simple analysis detailed in Appendix D, for the same change in velocity (Δu) a one-second increase in I_{sp} results in a savings of 134.5 lbm (61 kg). Based on the numbers from Table 1 for medium western vehicles, this results in a savings of as much as \$671,693 a launch, or larger and more capable satellites. Moreover, that only represents a single second increase in I_{sp} so the actual savings could be dramatically greater.

1.2. Objectives

To meet the goals of IHRPT, a Dual Expander Aerospike Nozzle engine (DEAN) is being designed to provide 50,000 lbf (222.4 kN) of thrust with an I_{sp} of 464 s. This research effort focuses on the development of a thrust chamber, nozzle, and cooling jacket in an attempt to satisfy the following three goals.

1. Determine feasibility of meeting the IHRPT Phase III orbit transfer vehicle goals with the DEAN concept
2. Implement and improve upon a design process focused on the energy conversion section of a rocket engine (combustion chamber, nozzle)

3. Perform detailed design analysis of the energy transfer components (cooling jackets) making the DEAN possible

1.2.1. The DEAN

The DEAN will utilize liquid hydrogen and oxygen as the fuel and oxidizer. Each will operate in their own expander cycle powered by the heat from the thrust chamber and nozzle. The DEAN is also designed with an aerospike or plug nozzle. The DEAN has the potential to dramatically reduce the cost of launching a satellite. Figure 1 show a schematic of the Dean.

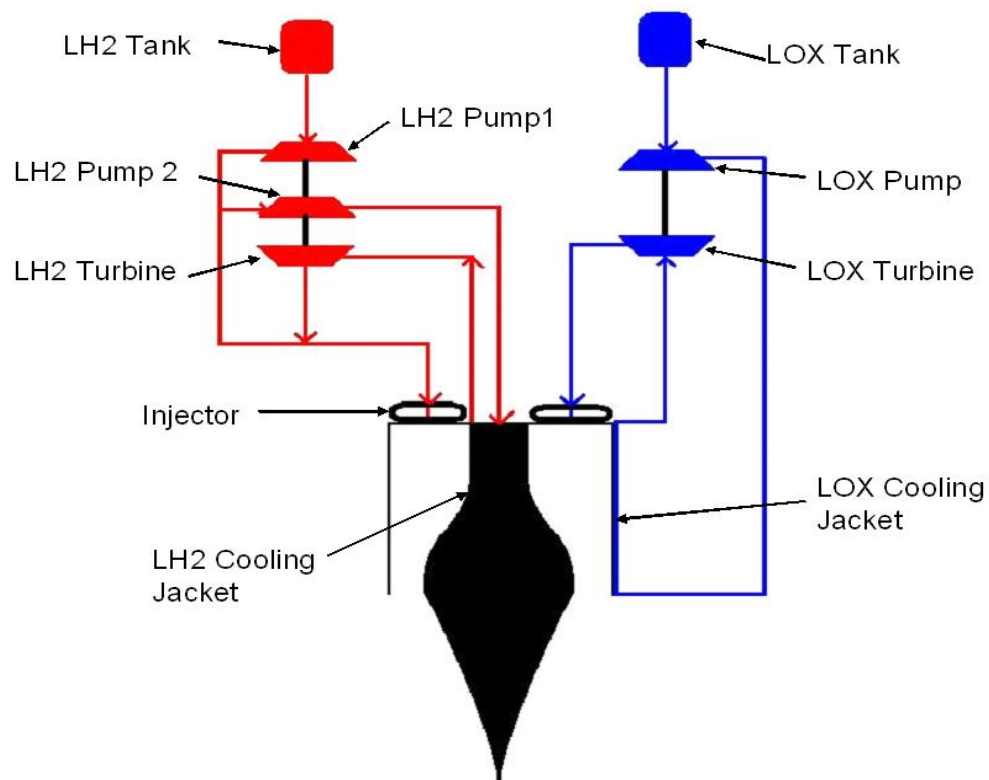


Figure 1. The Dean Schematic

Figure 1 shows that each of the fluid flows is contain their own turbo-machinery and cool a separate wall (oxygen cools the outer-wall and hydrogen cools the inner-wall). Four system design choices make the DEAN a revolutionary engine. First, the Dean

utilizes the aerospike nozzle that will dramatically reduce the weight and improved performance over a bell nozzle. Since the fuel and oxidizer are separated until injection into the chamber there is no need for inter propellant seals thus reducing a critical failure mode increasing reliability. The split flow on the fuel side reduces the required horsepower that increases the life of the turbo-machinery. Lastly, the design has the ability to be throttled.

In order to analyze the design of the DEAN, two computational programs will be used. Two-dimensional kinematics (TDK 04TM) will be used to design the contour of the nozzle. Numerical Propulsion System Simulation (NPSSTM) will be used to assess the performance of all the components of the DEAN. The thrust chamber, nozzle, and cooling jacket are the focused of this document.

1.2.2. Thrust Chamber

The thrust chamber embodies the essence of rocket propulsion: the acceleration of matter and the reaction imparting propulsive force to the vehicle. The aim is to achieve a device of maximum performance, stability, durability while minimizing the size, weight, and cost. In this report, the thrust chamber consists of the combustion chamber and the injector. The combustion chamber provides a volume for proper mixing of the propellants and length for complete combustion. The injector distributes the prescribed propellant mass flows to the chamber. The key variables for the thrust chamber are the geometry, pressure, and temperature of the chamber.

1.2.3. Nozzle

The nozzle is directly connected to the combustion chamber. The nozzle converts the enthalpy of the hot combusted gases into kinetic energy and produces the thrust of the

engine. The key variables affected by the design of the nozzle are thrust, I_{sp} , nozzle length, and expansion ratio (ϵ). Maximizing the I_{sp} is beneficial to any rocket design as shown earlier. In the design of the nozzle, the ideal length is often quite long, adding weight to the engine. Therefore, a design consideration is to minimizing the length of the nozzle while still maintaining performance near the ideal case.

1.2.4. Cooling Jacket

The combustion temperatures in the thrust chamber are extremely high. Additionally, the heat-transfer rates from the combusted gases to the wall are high. Consequently, the cooling jacket requires major design consideration. Not only does the jacket need to keep the walls cool enough to maintain their structural integrity, adequate heat must be transferred to the cooling fluids to power the turbines. The cooling jacket will be analyzed based on the temperature of the chamber wall and the temperature change in the cooling fluid.

1.3. Preview

The remainder of this report begins with review of the subjects relevant to the thrust chamber, nozzle, and cooling jacket. The methodology employed to conduct the work within this report is presented next. The results obtained from the methodology described is presented and discussed. Finally, the conclusions inferred based on the results of this report are stated and any recommendations based on the work done are declared.

2. Background

A substantial amount of work has already been completed covering the wide range of topics relating to the design in this thesis. The purpose of this Chapter is to present the prior knowledge that exists which can set benchmarks and help in the execution of the design of the DEAN. Ideas and benchmarks from these works were considered in the design of the three main elements in this thesis.

2.1. Orbit Transfer Engines and Mission Requirements

2.1.1. Baseline Engine

The DEAN was primarily designed to replace the Pratt and Whitney RL10 rocket engine. The original RL10 was designed in 1959 as an upper-stage liquid-oxygen liquid-hydrogen expander cycle rocket engine. The most current incarnations of the RL10 is the RL10B-2. The RL10B-2 features the world's largest carbon-carbon extendible nozzle. This high-expansion ratio nozzle enables the RL10B-2 to achieve a remarkable 465.5 sec of specific impulse and lift payloads of up to 30,000 lbf.³ Figure 2 shows an image of the RL10B-2.



Figure 2. RL10B-2(with permission from Pratt & Whitney) Error! Bookmark not defined.

In Figure 2, the RL10B-2 is shown inside the expandable skirt. The RL10B-2 currently powers the upper stage of the medium and heavy-lift versions of Boeing's Delta IV for Evolved Expendable Launch Vehicle (EELV), government and commercial missions.

The RL10 is also used on the Centaur upper stage. With the Titan IVB and the Centaur upper-stage, they are able to insert payloads greater than 12,700 pounds directly into geosynchronous orbit. The high-energy Centaur upper stage has evolved to become a very versatile vehicle. Performing a three-burn mission, the Centaur achieves parking

orbit with the first burn, boosts itself and the satellite to a highly elliptical orbit with second burn, and circularizes the orbit at geosynchronous altitude with the third burn⁴.

The Centaur propulsion system uses 2 RL10A-3-3A Pratt & Whitney engines, Each engine produces 16,500 lbf of thrust, a 444.4 sec nominal I_{sp} at 5.0:1 mixture ratio and an area ratio of 61:1.⁴ This series of engines has been used successfully since 1963 on the Saturn and Atlas/Centaur vehicles. The RL10A-3-3A uses an expander cycle, where all of the LH_2 is burned in the combustion chamber, except for a small amount used for autogenously pressurization and pump bearing cooling/gear box pressurization.⁴ The turbine working fluid is the supercritical hydrogen heated in the regeneratively cooled thrust chamber.

2.1.2. Typical Mission Requirements

One of the simplest and most common methods of putting a spacecraft into geostationary orbit involves three steps: launch to low earth (or parking) orbit with chemical propulsion; erect a GTO (geostationary transfer orbit) with an additional chemical stage; and perform a simultaneous circularization-and-plane-change maneuver at the apogee of the GTO.⁵

With an Atlas/Centaur class launch vehicle, the conventional path to the geostationary orbit (GEO) is a two-burn Centaur stage. The first burn establishes a slightly elliptical parking orbit and the second burn places the satellite in a geostationary transfer orbit.⁵

2.1.3. Expander Cycles

In general there are three classic engine system configurations; gas-generator cycle, expander cycle, and staged combustion cycle. The DEAN utilizes the expander cycle. The expander cycle places the turbine inline with the thrust chamber, exhausting directly into the chamber.⁸ Figure 3 shows a schematic of the expander cycles of the RL10B-2.

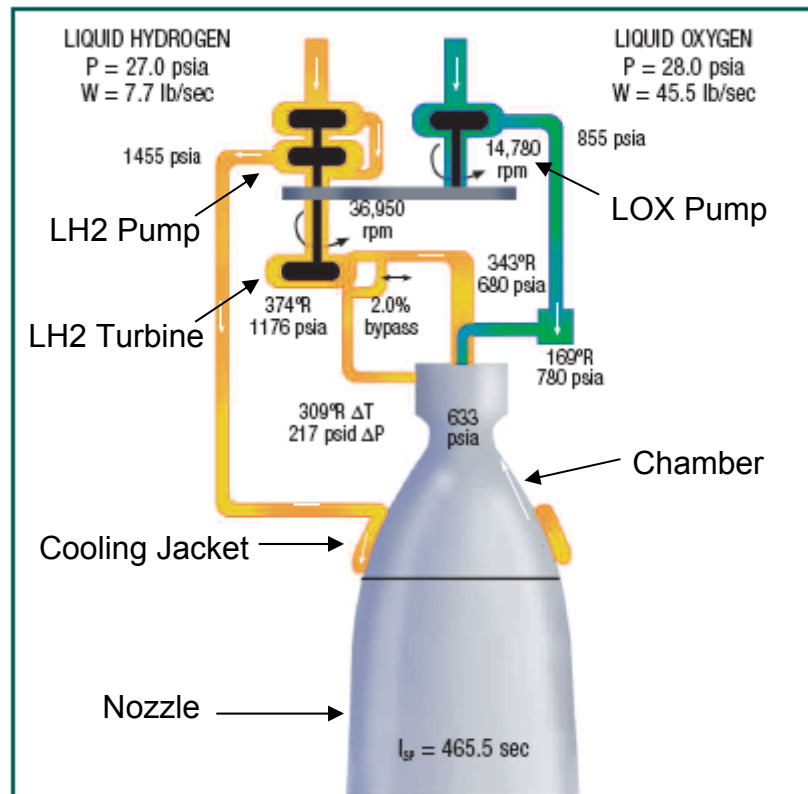


Figure 3. RL10B-2 Cycle Schematic (with permission from Pratt & Whitney)^{Error!}

Bookmark not defined.

Like in Figure 3, most expander cycles use the fuel heated through cooling of the chamber wall as the working fluid for the turbine.

The turbine powers the pumps that allow the propellants to be stored at lower pressures, thereby reducing the structural weight of the tanks. The limiting factor to the

performance of an expander cycle is the turbine inlet temperature, that in turn limits the attainable chamber pressure. Consequently, the expander engine is primarily used as a space engine where it can exhaust to a vacuum and can have a very high nozzle area ratio even though it has a lower chamber pressure.

2.2. Thrust Chamber

2.2.1. Rocket Engine Performance

A common performance parameter used to define a rocket engine is the specific impulse (I_{sp}). The I_{sp} compares the thrust of the engine to the propellant mass flow rate. Equation 1 show the I_{sp} as defined by Humble, Henry & Larson:⁶

$$I_{sp} = \frac{F}{\dot{m}g_0} \quad (1)$$

In Equation 1, F is the thrust, \dot{m} is the propellant mass flow rate, and g_0 is the acceleration due to gravity. The units for I_{sp} is seconds for both English or SI units.

In order to describe the performance of each component of the thrust chamber, two coefficients are defined. For the combustion chamber, the characteristic velocity (c^*) characterizes the influence of propellant choice through absolute maximum temperature achievable. For the nozzle, the thrust coefficient (C_T) provides the conversion of the potential energy to kinetic energy as well as the efficiency of the nozzle expansion. Equations 2 and Equation 3 for c^* and C_T comes from Hill & Peterson:⁷

$$c^* = \sqrt{\frac{1}{\gamma} \left(\frac{\gamma + 1}{2} \right)^{\frac{\gamma+1}{\gamma-1}} \frac{\bar{R} T_0}{\bar{M}}} \quad (2)$$

$$C_T = \sqrt{\frac{2\gamma^2}{\gamma-1} \left(\frac{2}{\gamma+1} \right)^{\frac{\gamma+1}{\gamma-1}} \left[1 - \left(\frac{p_e}{p_0} \right)^{\frac{\gamma-1}{\gamma}} \right]} + \frac{p_e - p_a}{p_0} \frac{A_e}{A^*} \quad (3)$$

In Equation 2, γ is the ratio of specific heats, T_0 is the total temperature in the chamber, \bar{R} is the universal gas constant, and \bar{M} is the molecular weight of the propellant. In Equation 3, p_e , p_a , and p_0 are the exit, ambient, and total chamber pressure respectively, A_e is the exit area and A^* is a characteristic area for a Mach number of one. From Equation 2, c^* is primarily a function of the combustion properties, and from equation 3, C_T is primarily a function of nozzle geometry. To demonstrate the influence of the fuel-oxidizer composition on c^* , Table 2 shows the values for three fuels with liquid oxygen.

Table 2. Influence on c^* ⁷

Oxidizer	LO ₂	LO ₂	LO ₂
Fuel	LH ₂	RP1	CH ₄
O/F	4.83	2.77	3.45
T₀₁ (K)	3250	3700	3560
Avg bulk density (kg/m³)	320	1030	830
c* (m/s)	2386	1838	1783

In Table 2 LH₂ is liquid hydrogen, RP1 is a hydrocarbon fuel and CH₄ is liquid methane. The values for Table 2 come from Hill & Peterson.⁷ In each case shown in Table 2, the O/F ratio was chosen to maximize the I_{sp} and the chamber pressure was 6.89 MPa. As apparent from the data, the molecular weights of the propellants and the values of c* depend significantly on the fuel-oxidizer combustion.

With Equations 1 through Equation 3, a simple performance analysis can be conducted. As stated by Huzle & Huang,⁸ the calculation of thrust-chamber performance is based on the theoretical propellant combustion data and the application of certain correction factors. The theoretical propellant combustion data comes from thermo-chemical computations equating the heat of reaction of the propellant combination to the rise in enthalpy of the combustion gases. The desired and actual performance of the chamber calculated from these equations drives the design of the chamber presented next.

2.2.2. *Dimension of the Thrust Chamber*

The geometry of the thrust chamber is based on the pressure, propellant type, propellant mass flow rate, and the oxidizer-to-fuel ratio (O/F) derived from the performance analysis. There are several different approaches to defining the geometry of the combustion chamber. Humble et.al.⁶ begins by finding the throat area. The mass flow at the throat must be checked for proper operation, therefore the area can be determined. Through conservation of mass, the throat area (A_t) can be found from Equation 4:

$$A_t = \frac{\dot{m}c^*}{P_c} \quad (4)$$

To insure long residence times for the mixing and chemical reactions in the thrust chamber, the Mach number must be nearly zero. The low Mach number implies that the thrust chamber pressure is nearly the stagnation pressure. Therefore, the chamber area (A_c) can be found as a multiple of the A_t , as determined by the thermo-chemistry of the propellants.⁶ The result is Equation 5:

$$\frac{A_c}{A_t} = \frac{1}{M} \left[\left(\frac{2}{\gamma + 1} \right) \left(1 + \frac{\gamma - 1}{2} M^2 \right) \right]^{\gamma + 1 / 2(\gamma - 1)} \quad (5)$$

For Equation 5 the Mach number is generally in the range of 0.1 to 0.6. Humble et.al.⁶ also derives the chamber volume (V_c) from a ratio of the A_t . The chamber must be large enough to allow complete combustion. However, the larger the chamber the greater the weight. Equation 6 uses a characteristic length (L^*) to aid in the sizing of the chamber:

$$L^* = \frac{V_c}{A_t} \quad (6)$$

In Equation 6, L^* is the thrust chamber's characteristic length. Historical data and gas dynamics are the basis for the sizing of L^* . Small values of L^* imply a small engine. The goal of the rocket designer is to minimize the size and mass of the engine. Therefore, L^* must be made as small as possible while maintaining adequate combustion efficiencies.

2.2.3. *Injectors*

The job of the injector is to atomize, mix, and ignite the fuel and oxidizer. Ultimately, the injector promotes the complete combustion of the liquid propellants. Additionally, the pressure loss across the injector is important since it takes a way from

the pressure obtained in the chamber. To better understand the mechanisms involved in the injectors, it is useful to see what work has been done in this area. Rahman & Santoro⁹ reported relevant information on predicting spray drop-sizes from liquid oxygen and gaseous hydrogen. Figure 4 shows a schematic of a coaxial injector.

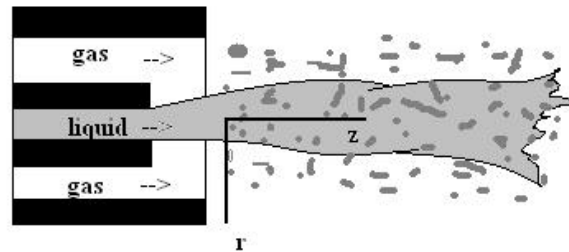


Figure 4. Shear Coaxial Gas/Liquid Injector

Atomization is of interest to the propulsion community from the standpoint of propellant injector design for liquid rockets engine combustion chambers. Atomization from a shear coaxial jet refers to the breakup of the core liquid jet by shear forces due to a co-flowing, high velocity, annular gas jet surrounding the core liquid stream.⁹ Data presented in this paper did not contain any experiments that simulate the unique propellant properties of liquid oxygen and gaseous hydrogen; such as gaseous hydrogen injection density and liquid oxygen surface tension and viscosity. Simulation of these properties is crucial to obtaining reliable atomization results that are directly relevant.

Lightfoot, Danczyk & Talley¹⁰ suggested three causes of atomization from wall-bounded films: liquid turbulence, stripping of waves, and stripping/tearing resulting from gas-phase vortices. Turbulent eddies within the liquid can interact with the interface causing it to become roughened and eventually forming ligaments. These ligaments may then break down into droplets. Results cite several important non-dimensional parameters including ratios of film height to hydraulic diameter, mean velocity to RMS

velocity fluctuations as well as a liquid Weber number based on hydraulic diameter and mean surface velocity.¹⁰ Coherent gas-phase vortices may form as a result of injector geometry features such as the gap or the lip. If the liquid's energy is sufficiently larger than the gas, then the gas-phase vortex will be displaced; otherwise, the vortex will alter the path of the liquid. In the latter case, droplets may be formed when the vortex distorts and tears liquid away from the film or when aerodynamic forces arising from the new shape of the interface strip liquid away.¹⁰ Low energy ratio simulations show waves form on the interface downstream of the lip. These waves are uniform and grow until they reach a size where the gas flow can strip mass from their crests. The uniform nature and growth of these waves implies hydrodynamic instabilities cause the droplet formation. The lip, the spacer between the oxidizer and fuel stream, seems to have very little effect on the general atomization behavior; a stronger impact is expected if the gradient of taper is small enough that the flow remains attached to the injector. Current understanding suggest the relative momentum difference between the liquid and gas particularly in the axial direction plays a large role in the film's behavior.¹⁰ At high kinetic energy ratios, gas-phase structures control the film's behavior and atomization. At low kinetic energy ratios, waves form on the surface of the film and are responsible for atomization. Experiment showed atomization due to turbulence occurred at relatively large gas velocities; suggesting the gas turbulence, not liquid turbulence, was responsible.¹⁰

Besides co-axial injectors, another type of injector that displays beneficial characteristics is the Pintle injector.¹¹ Figure 5 shows a schematic of a Pintle injector.

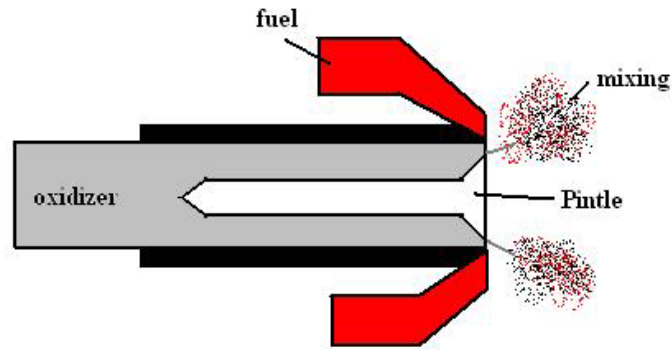


Figure 5. Pintle Injector

Dressler and Bauer found a Pintle injector design could deliver high combustion efficiency and enables implementing some unique operating features, such as deep throttling and injector face shutoff.¹¹ Design simplicity makes it ideal for low cost engines. Significantly lower development and qualification costs result because injectors can be easily adjusted and optimized by changing only two simple parts. Additionally, there has never been an instance of combustion instability in a Pintle engine during any ground or flight operations.¹¹ Either fuel or oxidizer can be centrally metered in the Pintle design. The Pintle injector's flow field induces recirculation regions.

Woodward et. al.¹² investigated combustion performance of coaxial and Pintle injectors using liquid oxygen and ethanol. Though not the exact same as the oxygen and hydrogen used for the DEAN, the results should show similar trends. The findings shows marginal liquid oxygen quality was seen to have a significant influence on combustion efficiency for both injector types.¹² Pintle injector designed specifically for orbital maneuvering system projects operated both in a stable manner and with high performance. Additionally, changes in O/F ratio resulted in changes in c^* efficiency, a point to consider when optimizing.

As shown in this section, many factors affect the design of injectors, however the work done in this document will be limited to the effect the injector will have on the combustion efficiency and pressure drop across the injector. Still this information will be useful in determining the detailed design of the injectors later.

2.3. Nozzle

The key demands on future launch systems are the reduction of Earth-to-Orbit launch costs in conjunction with an increase in the reliability and operational efficiency. Launch systems operate in a constantly changing ambient environment. A nozzle that can maintain high performance over a wide variety of ambient conditions could dramatically improve efficiency and decrease cost. The DEAN utilizes one such concept known as the aerospike or plug nozzle. A booster-stage would experience the greatest change in ambient pressure and could benefit most from the aerospike design. However, an upper-stage can benefit as well since it can encounter a change in ambient pressure depending on where it ignites. Figure 6 shows an aerospike.

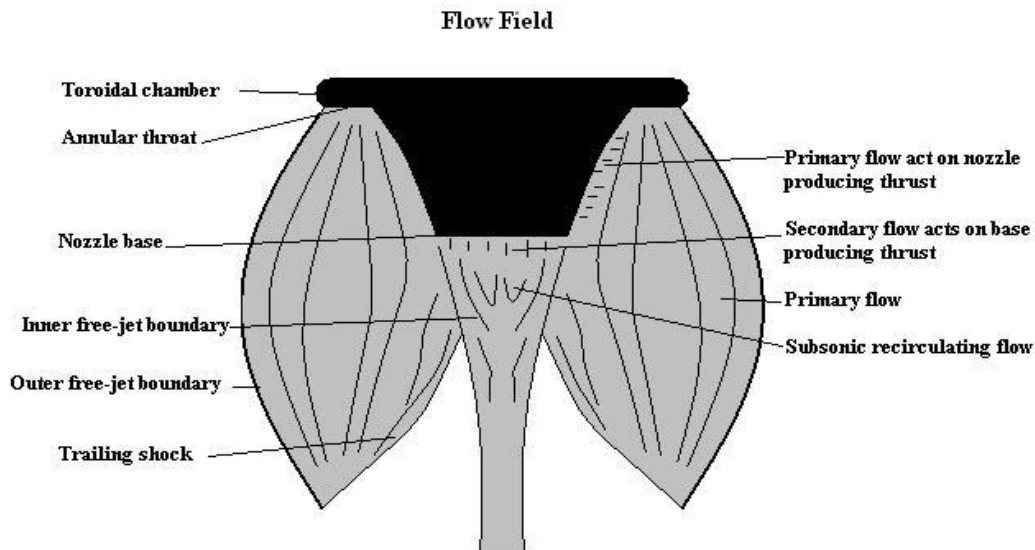


Figure 6. Aerospike

The aerospike nozzle is considered to have globally better performance when compared to a conventional bell nozzle, since the expansion of the jet is not bounded by a wall and therefore can adjust itself to the environment by changing the outer jet boundary.

2.3.1. Aerospike

Hagemann et.al.¹³ examined several nozzle concepts that could result in superior performance over conventional nozzles. The advantage of aerospike nozzles is it demonstrate altitude adaptation up to their geometrical area ratio. This results in improved performance for the entire flight envelope over the conventional bell nozzle. Additionally, for an aerospike nozzle, at lower pressure ratios an open-wake flow established at a pressure level practically equal to the ambient pressure. At a specific pressure ratio (PR), close to the design PR of a full-length nozzle, the base flow suddenly changes its character and turns over to a closed form.¹³ A constant base pressure no longer influenced by ambient pressure characterizes this flow. Shorter plug nozzles with high truncations trigger an earlier change in wake flow. At transition, the pressure within the wake approaches a value below the ambient pressure and the full base area induces a negative thrust.¹³ Beyond the transition point, pressure within the closed wake remains constant, as ambient pressure decreases. The base pressure is then higher than the ambient pressure, resulting in a positive thrust contribution.¹³

A more detailed analysis of the aerospike concept was done by Hagemann, Immich & Terhardt¹⁴ using the numerical methods of Euler and Navier-Stokes. The results showed the altitude compensation capabilities of the aerospike were indisputable, but they lose this capability for pressure ratios above the design point.¹⁴ Additional

performance losses were induced due to non-isentropic effects like shock waves. Figure 7 shows the flow over an aerospike nozzle. In Figure 7, the top picture depicts the flow field at PR below design (lower altitude), the middle picture is at the designed PR, and the lower picture is at a PR above the design point (higher altitude).

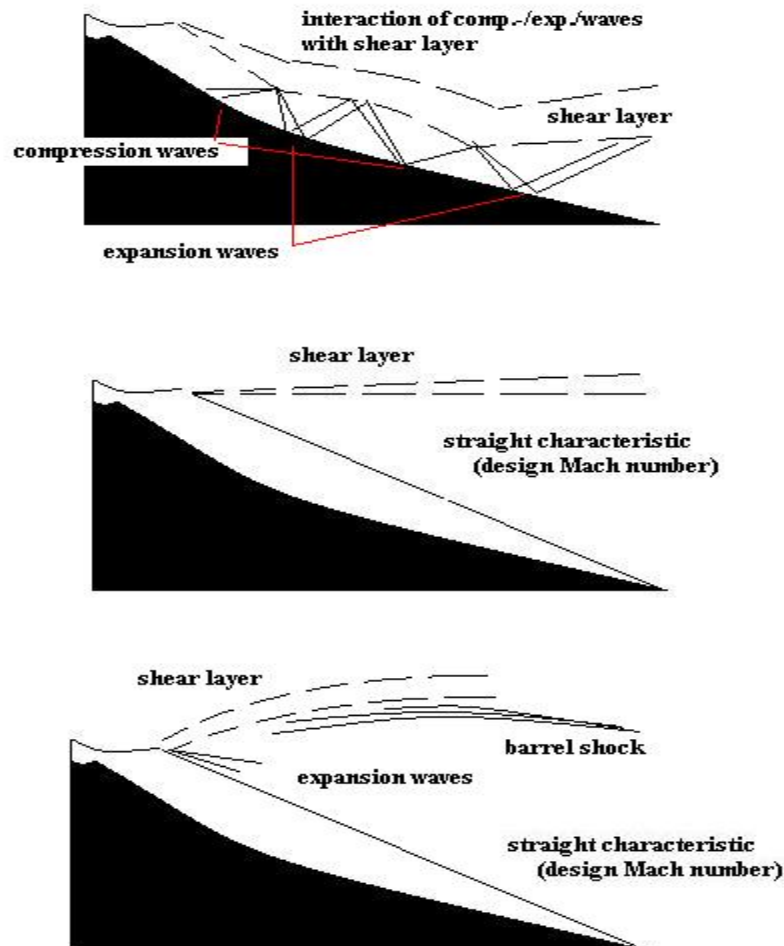


Figure 7. Flow Phenomena of Plug Nozzle

As Figure 7 illustrates, for pressure ratios lower than the design PR of a plug nozzle with a well-contoured body, the flow primarily expands along the plug body to the ambient pressure. Thus, only the first part of the nozzle contour acts as an expansion contour down to the point where the first right running characteristic that feels the

ambient pressure meets the contour.¹⁴ At the design pressure ratio, the characteristic with the design Mach number should be a straight line emanating to the tip of the central plug body, and the shear layer is parallel to the centerline. At pressure ratios above the design pressure ratio, the wall pressure distribution remains constant, and the plug nozzle behaves as a conventional nozzle, the loss of its capability of further altitude adaptation included.¹⁴

Truncation of the nozzle makes the aerospike concept more feasible, but results in further performance losses. Figure 8 shows the flow over a truncated aerospike. In Figure 8 the top drawing depicts the flow field at PR below design, the middle drawing is at the designed PR, and the lower drawing is at a PR above the design point.

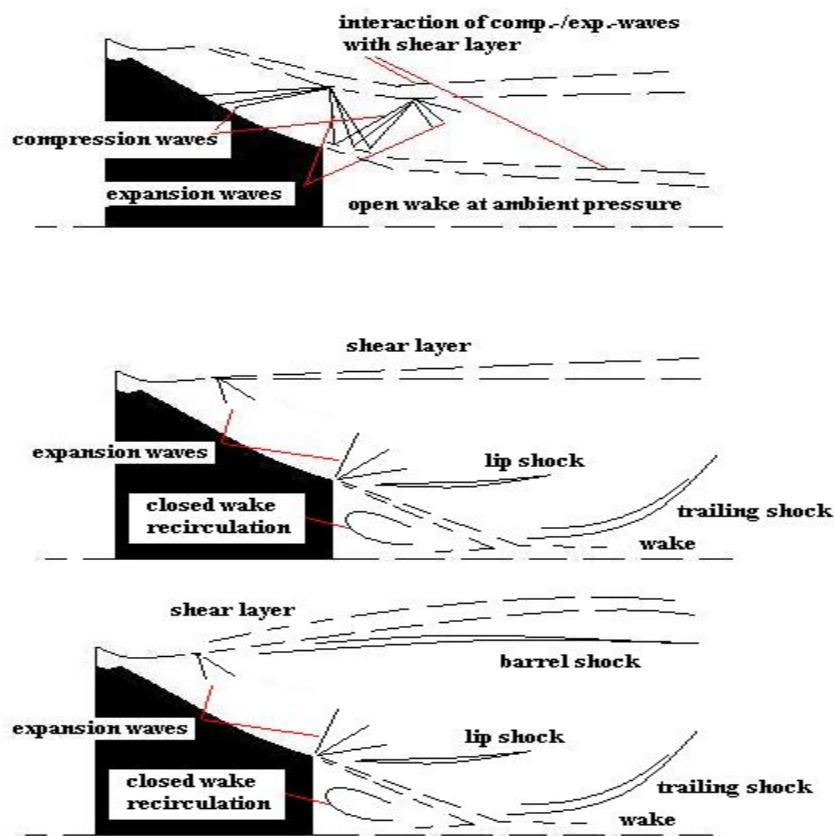


Figure 8. Flow Phenomena of Truncated Plug Nozzle

As seen in Figure 8, at lower pressure ratios an open wake flow establishes, with a pressure level practically equal to the ambient pressure. At a certain pressure ratio close to the design pressure ratio of the full-length plug nozzle, the base flow suddenly changes its character and turns over to the closed form, characterized by a constant base pressure that is no longer influenced by the ambient pressure.¹⁴ At the transition point, the pressure within the wake approaches a value that is below ambient pressure, and the full base area induces a negative thrust.¹⁴ Beyond the pressure ratio at transition, the pressure within the closed wake remains constant. A further decrease of the ambient pressure is resulting therefore in a positive thrust contribution of the total base area.¹⁴

Ambient flow also slightly degrades performance. All these losses add to several percent, making plug perform worse at high altitude when designed for a lower altitude when compared to similar bell nozzles.¹⁴ To get the most benefit, the design pressure ratio should be chosen at as high an altitude (pressure ratio) as possible.

Concerning the truncation, Ito, Fujii & Hayashi¹⁵ state the nozzle performance was believed not to be strongly affected by cutting off the nozzle because base pressure compensated for the loss of the thrust. For a full-length nozzle, flow follows the nozzle wall and smoothly moves to the wake region. For a truncated nozzle, flow separates at the trailing edge and expands. The resultant shear layer induces a trailing shock when it converges and turns the flow parallel to the axis. When truncated, the ramp area decreases due to the shorter length. Therefore, thrust from the ramp pressure reduces. The thrust generated by base pressure increases due to the increased area. Therefore, the total nozzle thrust becomes almost the same for any nozzle truncation.¹⁵ Quantitatively, the thrust coefficients of the plug nozzles have the same trend as the ideal thrust

coefficient indicating the plug nozzle operated at near peak thrust efficiency over a wide pressure ratio range. As the altitude increases, ambient pressure decreases, therefore the base pressure thrust increases. Ito et.al. have found a contoured plug nozzle had higher performance compared to a conical plug nozzle over all pressure ratios. As the pressure ratio increases, the thrust difference between the contoured and conical nozzle increases almost linearly. The advantage of a contoured nozzle becomes remarkable as the altitude increases. External flow does not influence the pressure distribution on the nozzle surface at high-pressure ratios.¹⁵

In further work done by Ito & Fujii¹⁶, they found that in the low-pressure ratio regions, the stagnation point was located at a distance from the plug base. When the pressure ratio increases, the stagnation point suddenly moves toward the plug base. The stagnation point does not move with further pressure ratio increases. The pressure ratio at which an abrupt movement occurs is the same as the pressure ratio where the characteristic transition occurs. The ambient pressure influences base pressure as long as the flow initiated from the stagnation point due to the envelope shock-wave impingement reached the base. They conclude the aerospike nozzle performance is insensitive to length of nozzle because the base pressure compensates the loss of the thrust force due to nozzle truncation.¹⁶ The characteristics of the flow at the base did not change whether the external flow was induced or not. The ambient pressure influences the base pressure when the pressure ratio is low and the base pressure becomes independent from ambient when the pressure ratio is high. The base produces positive thrust when the base pressure is independent from ambient pressure.

In contrast to Ito & Fujii conclusion on external flow effects, Nasuti & Onofri¹⁷ found the numerical analyses they performed indicates the interaction of the exhaust jet with the external air in truncated plug nozzles may significantly affect the nozzle behavior in the over-expanded regime. In particular, even in the ideal case important losses take place yielding a sudden performance drop. The presence of a finite-thickness or thick shroud substantially changes the flow behavior adding further drag in itself and yielding an overexpansion at the primary nozzle lip (edge of the outer wall). Because of this overexpansion, the exhaust jet finds a lower ambient pressure at the lip than in the still air case, and consequently adapts the flow to a lower-than-ambient pressure. This was a further cause of drag appearing in part over the plug wall and in part over the plug base. Moreover, the reduction of the value of pressure ratio for transition from open to closed wake reduced the overall nozzle performance. This reduction yielded a base drag in the range between the actual and still air transition values. Concerning the mechanism of wake transition, in the supersonic case the transition is governed by the internal shock, rather than by the last wave of the expansion fan at the primary nozzle lip.¹⁷ On the contrary, the analysis of the flow-field in the subsonic flight conditions has shown only slight changes were expected in comparison to the still air case.

Ito & Fujii¹⁸ also performed a test to determine the effects of base bleed. They found the base pressure increased due to an increase in base area and compensated for the total thrust loss due to a decrease of the ramp pressure thrust. As a result, the total nozzle thrust becomes almost the same for any nozzle truncation. When they introduced base bleed, it expanded toward low pressure and interacted with the main exhaust flow at some distance from base surface. The base bleed that promoted recirculation at the base

region produced the largest pressure thrust.¹⁸ Additionally, base bleed producing no divergent loss leads to the maximum total thrust. At low altitude (low PR) base pressure linearly decreases as the ambient pressure decreases; showing the external environment influences the base region. Pressure thrust produced by base in this region is small. At high altitude (high PR), the base pressure is constant despite a variation in altitude (decrease in ambient pressure). The base-pressure thrust increased in this region. The base pressure with and without base bleed acted in a similar manner. Conditions with bleed had a higher-pressure level than without bleed. The thrust coefficients with and without bleed had the same trends as an ideal thrust coefficient exhibits indicating the aerospike operates at nearly peak thrust efficiency over a wider range than a bell nozzle. The thrust performance with base bleed exceeded the performance without base bleed over the whole altitude range.¹⁸ The base bleed orientation with the greatest performance was at the outer region of the base, directed parallel to the nozzle axis.

2.4. Cooling Jacket

Cooling of the thrust chamber and nozzle is essential in the design of any rocket engine. Many different cooling approaches exist and some are outlined below.

2.4.1. Heat Transfer

To describe the environment in the thrust chamber, heat transfer equations are needed. An excellent source to provide an understanding of heat transfer is Incropera et.al. *Fundamentals of Heat and Mass Transfer*.¹⁹ The two major mechanisms in which the heat is transferred are through conduction and convection. Conduction is the

transport of energy in a medium due to a temperature gradient.¹⁹ A basic equation to determine the conductive heat rate is shown in Equation 7:

$$q_x = -kA \frac{dT}{dx} \quad (7)$$

In Equation 7 q_x is the heat rate with units of watts (W), k is the thermal conductivity with units W/(m*K), A is the area, and dT/dx is the derivative of the temperature. The thermal conductivity is a material constant.

Convection describes the energy transfer between a surface and a fluid moving over the surface.¹⁹ A basic equation to determine the convection heat flux is shown in Equation 8:

$$q'' = h(T_s - T_\infty) \quad (8)$$

In Equation 8 q'' is the heat flux with units of W/m², h is the convective heat transfer coefficient with units W/(m²K), and T_s and T_∞ are the temperature of the surface and fluid respectively. Unlike the thermal conductivity, which is a material constant, the convective heat transfer coefficient depends on numerous fluid properties, surface conditions and flow conditions.

Some of the constants used in the heat transfer equations have to be experimentally determined. Von Glahn²⁰ proposed correlation treating nozzle heat transfer with a cooled approach section. This concept applies to both low and high Reynolds number regions. It also applies to the entire nozzle, whether convergent or divergent. The proposed correlation consists of a fully turbulent pipe-flow heat-transfer equation modified by suitable nozzle geometry parameters.²⁰

Schacht, Quentmeyer, & Jones²¹ conducted a gas-side heat-transfer experiment over a wide range of chamber pressures with an emphasis on the accurate determination of hot gas-side heat-transfer rates in the regimes of high heat flux. Equation 9 adequately correlates the data at specific locations in the nozzle:

$$St * Pr^{0.7} = C \cdot Re_d^{-0.2} \quad (9)$$

In Equation 9 St^* , Pr^* , and Re_d^* are Stanton, Prandtl, and Reynolds number respectively and C is a constant. The constant varies with axial location and is less than 0.026 for all locations except the chamber. The constant at the throat was 42% less than the widely used value of 0.026.

Boldman, Schmidt, & Gallagher²² showed the heat transfer at a given station in nozzles generally exhibits two distinct depressions from the predicted levels based on a turbulent pipe flow type of correlation. The larger of these depressions occurs at lower Reynolds numbers and was assumed the result of laminarization of the initially turbulent boundary layer. The smaller of these depressions, which occurred at high Reynolds numbers, was assumed the result of reduced turbulent transport associated with a turbulent boundary layer in an accelerating flow.

An experimental investigation conducted by Quentmeyer & Roncace²³ determined the hot-gas-side heat transfer characteristics for a liquid-hydrogen-cooled, subscale, plug-nozzle rocket test apparatus. The throat region correlation coefficient (C_g) for a Nusselt number correlation of the form in Equation 10:

$$Nu = C_g Re^{0.8} Pr^{0.3} \quad (10)$$

The averaged value is 0.023 for the Rigimesh faceplate and 0.026 for the platelet faceplate.

2.4.2. *Cooling Techniques*

There are several techniques used to cool the chamber and nozzle. The most common include regenerative cooling, dump cooling, film cooling, transpiration cooling, and ablative cooling. Regenerative cooling is most relevant to the DEAN and the technique further studied.

Preclik et. al.²⁴ showed the development of the wall heat flux is not a quick process, but spreads out from the injector down to the convergent nozzle entrance. The calorimeter data also highlighted the flow and burning characteristics of the present, co-axial injection elements. These elements affect the level of the overall wall heat load approximately 25%. Two principles for reducing the hot gas side heat transfer rates, i.e. wall element mixture ratio trimming and gaseous hydrogen wall film cooling, were investigated in more detail. The tests clearly indicated wall film cooling employing the current slot design is much more efficient and effective when compared to wall element mixture-ratio trimming. With typical film cooling mass flow rates, the wall heat loads could be decreased by 20%. Moreover, under the presence of a coolant film, the individual flow characteristics of the different injection elements become less important.

Kim et. al.²⁵ conducted a test of a regeneratively cooled chamber with film cooling. From the experimental results with the film cooling mass flow rate at 10.5% of the main fuel mass flow rate, maximum heat flux at the nozzle throat was measured to be 30% lower than without film cooling at the nominal operating condition. The numerical analysis resulted in this case showing a 13% decrease. The film cooling mass flow rate

increased as the characteristic velocity decreased. When the mass flow rate of film cooling was 10.5% of the total fuel mass flow rate, the characteristic velocity is measured to be 1.2% lower than without film cooling at the design point.

In research by Naragi, Dunn, & Coats,²⁶ the effectiveness of regenerative dual-circuit cooling designs was studied. The dual-circuit showed reduced wall temperatures at the throat area for the space shuttle main engine (SSME) and for an RP1-LOX engine. A lower coolant pressure drop accomplished the reduction in wall temperature and resulted in lower coolant pumping power requirements. The overall result is a higher performing engine capable of delivering a greater payload to orbit.

Chiaverini, Sauer, & Munson²⁷ used a vortex combustion cold-wall chamber (VCCW) to study the heat transfer problem. They found the chamber sidewall heating rates did not display a significant dependence on chamber pressure, apparently due to the similar effects of elevated pressure on both thermal radiation (acting to heat the wall) and convective cooling from the outer vortex.

Immich & Caporicci²⁸ conducted an investigations within the FESTIP technology program on the high aspect ratio coolant channel and micro fin cooling channel chamber. These technologies have been selected as promising technologies, which can be expected to lead to considerable reductions of the combustion chamber wall temperature by improving the coolant side heat transfer significantly. This could be achieved by an increased heat transfer surface and by taking particular advantage of an enhanced fin effect. The concept was to increase the total number of cooling channels and to introduce microstructures at the coolant-side channel bottom.

Schmidt, Popp, & Frohlich²⁹ stated an improvement of coolant side heat transfer and consequently a decrease of the chamber wall temperature has only very minor effect on the increase of heat flux to the coolant, because the driving temperature difference cannot be changed much by reducing the wall temperature. A doubling of the coolant-side heat transfer, by higher coolant velocity, coolant side surface roughening or fins in the cooling channel etc., would only increase the heat flux to the coolant by about 6-7%. Increases of heat flux in the chamber by lower chamber diameter and consequently higher heat flux is another possibility. Reducing the chamber contraction ratio could increase the heat flux with a resulting 10-15 K (18-27 R) coolant temperature rise, but only if the chamber is elongated to keep L^* constant, which also increases the engine length.²⁹ The associated increase in cooling and combustion pressure drop would also increase the required hydrogen pump discharge pressure. This again would reduce the overall benefit for the cycle to a marginal improvement. On the other hand, from the injector side a certain face area is required, also limiting the possibility of employing such a measure. Roughening of the hot gas side surface of the chamber and nozzle would also increase the heat flux into the coolant. This has been demonstrated by the aging effect of chambers, running at their thermal limits.²⁹ The most straightforward design measure for increased heat transfer is the increased surface roughness of the hot gas side surface.

2.4.3. Aerospike Cooling

The aerospike adds additional challenges when it comes to cooling the nozzle since it is surrounded by the exhaust flow, whereas the Bell nozzle is exposed to the ambient surroundings on one side. In Sorge, Carmicino, & Nocito³⁰ a cooled linear plug

nozzle was constructed so hot gas tests could be carried out and performance measured. They chose a two-dimensional nozzle shape and a copper alloy on all the parts exposed to hot gas flow. In addition, to promote the heat transfer, ribs were placed on the duct surfaces exposed to the heat flux near the throat. The results have showed the experiment was able to ensure a maximum wall temperature on the gas side of 750 K (1350 R), a maximum wall temperature on the liquid side of 450 K (810 R) and, a water bulk temperature rise of about 298 K (537 R), with a pressure drop per circuit equal to 31 atm.³⁰ Even though this experiment uses water, the technique can be applied to any cooling fluid.

Kumakawa et.al.³¹ conducted a test with nickel plating on the hot-gas side. This test showed the heat flux was 30% lower than without nickel. A cross-flow condition of water suppressed the burnout on the ribbed surface more than the parallel flow condition. Combustion performance and heat transfer characteristics for the truncated conical plug nozzle were quite similar to those of conventional conical nozzles.

From Wang³² the highest level of heating occurs near the thruster outlet, on the ramp surface. The next highest level of heating occurs on the plug-base where the reverse-jet brings in the hot plume gases torch the surface. The relief comes from aspirating cold inner-base airflow into the plug-base region. The airflow penetrates as far as the base center. The pumping effect of the engine plume causes this aspiration.³² The heating on the plug sidewall is caused by the hot engine flow spilling off the side of the ramp, also known as the plume spillage heating.

Tsutsumi et.al.³³ observed the maximum heat-flux region is located where the jets from adjacent modules interact. The heat flux also increased at the module exit. The

downstream part of the module exit is exposed to a lower heat load. The heat-flux distribution over the linear aerospike nozzle is correlated with the viscous-inviscid interaction in the near-surface flow field. The heat flux increases remarkably at the region where the module outflows interact due to the downwash of module outflow to the nozzle surface. Moreover, since the ambient air is entrained into the vortex flow over the nozzle surface, a lower heat-flux region appears.

2.4.4. Material

Selection of the materials for the cooling jacket tends to drive many aspects of the design process. Peer & Minick³⁴ describes an advanced combustion chamber designed by Pratt & Whitney. The most significant feature is the use of a new copper alloy coupled with an improved processing technique. Their tubes can withstand repeated exposure to fabrication temperatures in excess of 1250 K (2260 R) and still retain yield strength five times greater than other copper alloys used in current rocket thrust chambers.³⁴ The tubular configuration of the chamber provides up to 40 percent more actual surface area due to the circular tube crowns and therefore, more heat transfer capability with lower thermal strain (increased life) than smooth wall hot-side fabricated channel configurations³⁴. The tubular construction also provides improved pressure drop characteristics over rectangular channel designs.

Schoenman³⁵ discusses the intensive effort to develop materials that can operate at higher temperatures over the last decade. A nominal target value of 2500 K (4460 R) has been established for the new materials of construction. The iridium/rhenium layered wall and the silicon/carbon composite are the most mature and can be considered for flight

applications. Iridium/rhenium materials can operate in temperatures 2477 K (4459 R) while silicon/carbon can operate in 1866 K (3359 R) temperatures.³⁵

Kumakawa et. al.³⁶ showed carbon-carbon and silicon/carbon composites have potential for use as lightweight materials exposed to temperatures in excess of 1700 K (3060 R). The exposed heat fluxes dictate whether active cooling would be required for these materials. Aerospoke nozzles made of composite would be exposed to severe operating conditions in a hot gas flow, including hot spots caused by shock interactions. Thus, an actively cooled composite is necessary in this case and considered a prime candidate for the aerospoke-nozzle wall structure

A significant challenge will be choosing materials to accommodate the liquid oxygen expander cycle of this concept. Gloyer, Knuth, & Crawford³⁷ designed a liquid oxygen cooled gas generator. They found copper, nickel and some steels can be used adequately with oxygen. These metals are used since they do not react with oxygen that would cause catastrophic failure. They also concluded the design appears to be limited to a single operating point design due to the liquid oxygen boiling sensitivity to factors such as O/F ratio, mass flow, temperature and pressure. For wider operating ranges, alternative designs which avoid two-phase flow would be preferred.

2.4.5. Aspect-Ratio

Changing the area of the chamber affects the heat transfer characteristics. This can be done through the aspect-ratio (AR) of the cooling circuit and/or the addition of ribs. The heat energy requirements of the turbo-pumps dictate longer combustion chambers.³⁸ Size limitations create the need for a different method to increase heat extraction. Increasing the area exposed to the hot-gas by using combustor ribs fulfilled

this requirement. The ribs increased the total area exposed to the hot-gas by 80% in his research, and thus enhanced the heat energy level imparted to the coolant working fluid³⁸.

An investigation was conducted by Carlile³⁹ to determine the effectiveness of using high-aspect-ratio cooling passages to improve the life and reduce the coolant pressure drop in high-pressure rocket thrust chambers. Figure 9 show the difference between a low and high aspect ratio channel (AR).

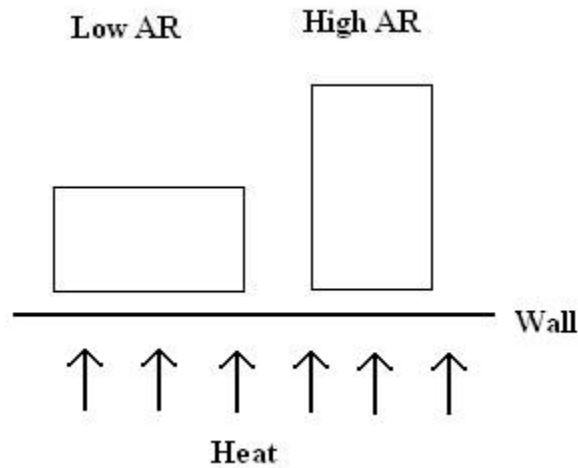


Figure 9. Channel Aspect Ratio

Figure 9 shows that the low AR channel is generally wider with more surface area along the wall while the high AR is taller with less surface area. The coolant pressure drop for the high-aspect-ratio chamber was reduced in increments to one-half the baseline chamber by reducing the coolant mass flow. The result still showed a reduction in the hot-gas-side wall temperature. The data indicated the hot-gas-side wall temperatures for the high-aspect-ratio chamber could have been reduced substantially further by using aspect ratios greater than 5.0.

Wadel & Meyer⁴⁰ found by increasing the cooling channel surface area through increasing aspect ratios, heat from the hot-gas-side wall is more efficiently transferred to

the coolant. The increased height and number of the ribs also enhance the heat transfer from the chamber liner to the coolant (i.e. enhanced fin effect). Therefore, it is possible to fabricate chambers with sufficiently greater total flow area to reduce pressure drop over a conventional design, and still gain an increase in the heat transfer capability.

In Neuner et.al.⁴¹ paper, laboratory experiments with large scale cooling channel models were described. The purpose of the experiments was to determine the impact of high-aspect ratio channels on curvature induced heat transfer enhancing phenomena. As a general result, secondary flow structures were clearly identified, even in channels with an aspect ratio of 8.0. These vortex phenomena have been found to enhance the heat transfer both in convex and concave side heated bends. Nevertheless, they appear only in and not far downstream of the corresponding curvatures.

The results of a parametric study on cooling channel geometry showed as the channel geometry changes, the coolant heat transfer coefficient dominates the heat transfer rate as compared to the area terms.⁴² In general, a small flow area tends to increase heat transfer; however, the pressure loss across the coolant channel restricts the extent the area can be reduced. Higher aspect ratio cooling channels are advantageous in balancing the pressure loss requirements with the heat transfer demands. The maximum allowable chamber pressure is limited by the survivable gas wall temperature. With respect to pressure loss and over all engine mass, a stepped-channel configuration proves to be superior to an invariant channel while maintaining the thermal performance of the regenerative cooling jacket. Evidence of this was presented by Schuff et.al. and is shown in Table 3.

Table 3. Stepped Channel vs. Constant Cross-Section Channel⁴²

	Constant Cross- Section	Stepped
P_{in} (psi)	2299	1838
P_{out} (psi)	1762	1680
ΔP_c (psi)	537	158
ΔT_c (R)	766	737
Engine Mass (lbm)	327	274

Table 3 shows a ΔP_c and ΔT_c decreased of 340% and 4%, respectively, from the constant cross-section to the stepped channel. Schuff et.al.⁴² state near the throat the gas side heat transfer coefficient increases significantly and as a result the wall temperature also increases. To adequately deal with the high heat transfer rate, the geometry remained the same as defined for the baseline case in this region. In the reduced combustion gas heat transfer regions upstream and downstream of the throat we increased the channel cross-sectional area to decrease the pressure drop and maintain a combustion gas side wall temperature less than at the throat. Consequently, increasing the channel cross-sectional area, decreased the coolant heat transfer coefficient h_c , therefore the stepped-channel case presented a tradeoff in performance parameters, temperature rise (ΔT_c) and pressure drop (ΔP_c) of the coolant along the entire length of the channels.

3. Methodology

This section will outline the methodology implemented to design the thrust chamber, nozzle, and cooling jacket of the DEAN. To begin the process, the performance goals outlined in the introduction establish a baseline engine derived from basic rocket equations.

3.1. General Sizing

The design started with the determination of a solution space for the size of the engine. The size of the engine begins with the choosing of initial parameters; the fuel and oxidizer, the oxidizer-to-fuel ratio (O/F), the chamber pressure (P_c), and expansion ratio (ϵ). As stated in the introduction, the DEAN will be powered by hydrogen and oxygen. Table 4 shows the remaining initial values to start the process.

Table 4. Chosen Parameters

O/F	ϵ	P_c (MPa/psi)
7	125	12/1740

The values in Table 4 are chose to maximize the I_{sp} of the design. The pressure and expansion ratio were chosen based on other like designs such as the RL-10. The exit Mach number (M_e) was found using ϵ and the ratio a specific heat (γ) in Equation 11:

$$\varepsilon = \frac{1}{M_e} \left[\left(\frac{2}{\gamma+1} \right) \left(1 + \frac{\gamma-1}{2} M_e^2 \right) \right]^{\frac{\gamma+1}{2\gamma-2}} \quad (11)$$

The value for γ is for a combusted flow and was assumed at 1.2 for the initial estimates. The exit Mach number along with the chamber pressure and γ were used in Equation 12 to determine the exit pressure:

$$P_e = P_c \left[1 + \frac{\gamma-1}{2} M_e^2 \right]^{\frac{\gamma}{1-\gamma}} \quad (12)$$

Based on the chemical reaction, the characteristic exhaust velocity (c^*) can be found using Equation 13:

$$c^* = \frac{\eta_{c^*} \sqrt{\gamma R T_c}}{\gamma \left(\frac{2}{\gamma+1} \right)^{\frac{\gamma+1}{2\gamma-2}}} \quad (13)$$

In Equation 13, the chamber temperature and the gas constant come from the chemical kinetics of the hydrogen and oxygen. The c^* efficiency (η_{c^*}) is set to a realistic value based on flow conditions and empirical evidence. From the results of Equation 11-13, the theoretical I_{sp} can be found using Equation 14:

$$I_{sp} = \lambda \left\{ \frac{c^* \gamma}{g_o} \sqrt{\left(\frac{2}{\gamma-1} \right) \left(\frac{2}{\gamma+1} \right)^{\frac{\gamma+1}{\gamma-1}} \left[1 - \left(\frac{P_e}{P_c} \right)^{\frac{\gamma-1}{\gamma}} \right]} + \frac{c^* \varepsilon}{g_o P_c} (P_e - P_a) \right\} \quad (14)$$

In Equation 14, λ is the nozzle efficiency and is set to a reasonable number based on other models. The ambient pressure is set to zero for a vacuum providing a maximum value. With the I_{sp} and the thrust, the mass flow can be calculated from Equation 1. The geometry of the combustion chamber can then be calculated as outlined in section 2.2.2.

3.2. Thrust Chamber

The purpose of the thrust chamber is to combine and combust the fuel and oxidizer. Several variables are involved in the design of the thrust chamber. Below are the input variables that cannot be changed (controls), variables that can be changed by the designer to produce the desired results (process variables), and the results used to determine the validity of the design (outputs).

3.2.1. Chamber Controls

The constant variables in the design of the chamber are the mass flow rate of the hydrogen and oxygen. The values for these mass flow rates come from a combination of the requirements of the overall cycle balance and sizing.

3.2.2. Chamber Process Variables

The changing variables include several key geometric aspects of the chamber. The primary aspects are the radius and length of the chamber. In the NPSS model, these variables are the radius and volume of the chamber. Additionally, the contours of the chamber can change to get desired results. These include the outer chamber wall and the inner spike

3.2.3. Chamber Outputs

The output variables used to evaluate the results are the pressure and temperature of the chamber. The pressure and temperature must be within material limits so the structural integrity of the chamber remains intact. However, with higher values, the performance of the rocket is generally better.

3.3. Nozzle

The purpose of the nozzle is to expand the flow and produce thrust. Below are the controls variables, process variables, and output results affecting the design of the nozzle.

3.3.1. Nozzle Controls

The variables held constant in the design of the nozzle are the nozzle outputs. These include the pressure, temperature, and mass flow.

3.3.2. Nozzle Process Variables

The variables that change are again the geometry of the nozzle. For the nozzle, this includes the throat area, ϵ , and the length. Additionally, the operating altitude is set by varying the ambient pressure input. The throat area is constrained by the area of the chamber and the limit of the Mach number at the throat equal to one. However, the area of the throat can be changed to accommodate both the chamber and nozzle but must maintain the mass flow.

3.3.3. Nozzle Outputs

The overall performance statistics characterizing the success of this effort are the I_{sp} and the thrust. The desire is to have the I_{sp} and thrust close to, if not more than the goal values listed in Chapter 1.

3.4. Cooling Jacket

The cooling jacket cools the walls of the thrust chamber and transports the proper energy to the turbines. Below are the control variables, process variables, and output results affecting the design of the cooling jacket.

3.4.1. Cooling Jacket Controls

The constant set for the cooling jacket come from the requirements of the turbo-machinery. These include the mass flow rate of the coolant, the inlet temperature, and the inlet and outlet pressures.

3.4.2. Cooling Jacket Process Variables

The process variables to be examined in the design space include the geometry of the cooling jacket. In NPSS, these are the area, volume, and number of channels. Another important parameter includes the surface area of the cooling jacket that transfers the heat. The geometry of the cooling jacket is dependent on the geometry of the chamber and nozzle. However, these geometries, such as the cross-sectional area of the channels, can be modified to meet the requirements of the cooling jacket.

3.4.3. Cooling Jacket Outputs

The analysis will focus on the wall and outlet temperatures of the cooling jacket in evaluating the performance. The wall temperature must remain low enough to prevent the wall from melting while the outlet temperature must be high enough to ensure sufficient power is transferred to the turbines.

3.5. NPSS

After defining the performance parameters of the engine, the data was input into NPSS to perform a power balance and pressure budget. The power balance and pressure budget confirms the validity of the DEAN design. Additionally, the NPSS codes has a high fidelity resulting in more accurate compared with the initial estimates. Additionally, changes to the design can be made quickly with the effects of the changes apparent.

NPSS was developed by NASA Glenn Research Center, in conjunction with the U.S. aero propulsion industry and the Department of Defense, to grow technologies capable of supporting detailed aerothermomechanical computer simulations of complete aircraft engines. NPSS can realistically model the physical interactions taking place throughout an engine, accelerating the concept-to-production development time and reducing the need for expensive full-scale tests and experiments.⁴³

A rocket engine was built in NPSS using elements to define the various components. Figure 10 shows a schematic layout of the NPSS model used to define the DEAN that is based on the schematic to the DEAN show in Figure 1.

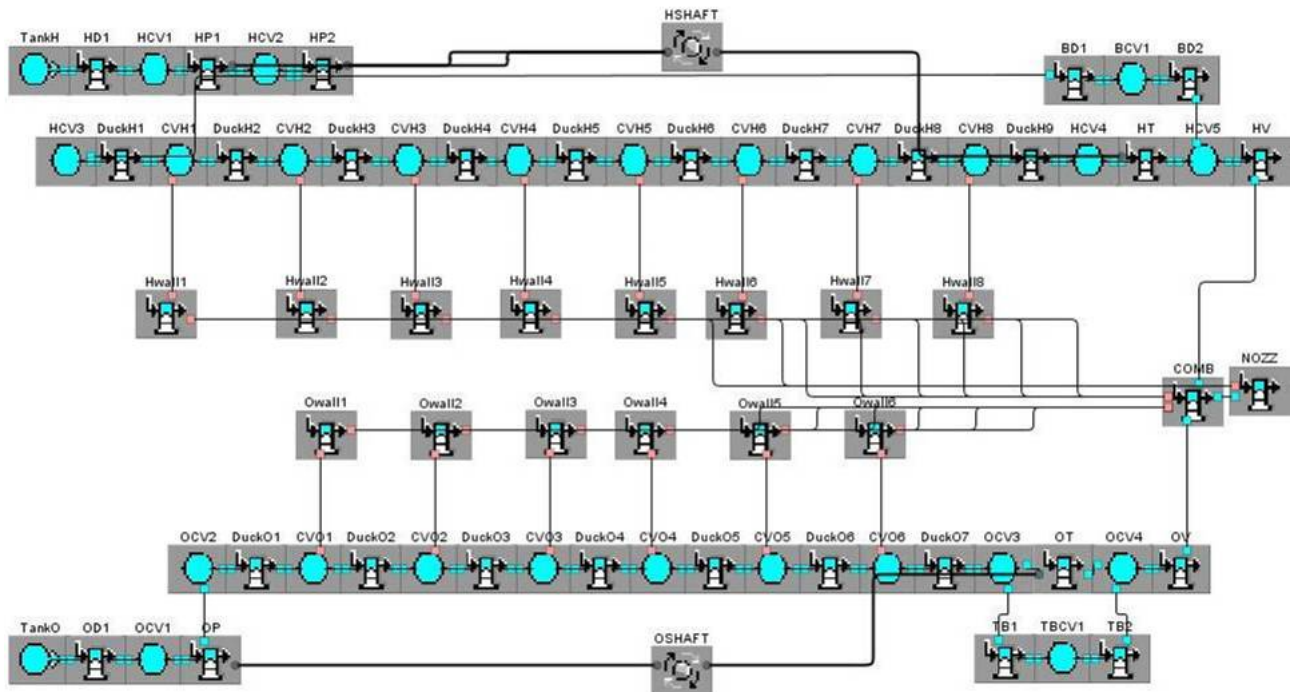


Figure 10. NPSS Model Schematic

As Figure 10 illustrates, each block represents an element and the elements are linked to one another through link ports. NPSS comes with defined elements for both air

breathing and rocket engines. Additionally, new elements can be programmed by the user. Each element has a set of input/output variables, independent/dependent variables, and equations. The user defines the input variables, though not all inputs need to be defined. Additionally, in the model, the composition of the flow, such as oxygen, and the thermodynamic data pack are defined. The inputs defined by the user, and the inputs of the composition and thermodynamic data, are used by the equations, with changing of the independent and dependent variables as defined in the element, to determine the outputs. The elements are linked through *linkPorts*. There are link ports for fluid and heat flow. Each element defines which type, and how many ports the element has.

The full model used for the DEAN is presented in Appendix B. For the combustion chamber, labeled *COMB* in Figure 10, was modeled using the *RocketComb1* element. This element requires inputs of chamber radius, chamber volume, and the composition of the oxidizer and fuel inlet, and outlet. Additionally, guesses for the oxidizer-fuel ratio (OFR), chamber temperature, chamber pressure, and weight flow are required. The aerospike nozzle, labeled *NOZZ* in Figure 10, is modeled with the element *RocketNozzle* and requires inputs of the throat area, area ratio (ϵ), and ambient pressure.

The cooling jacket model requires the use of three elements; one for a pressure drop, one for change in energy, and one for the transfer of thermal energy, because of the way NPSS works. Figure 11 shows one of the cooling jackets of the NPSS model.

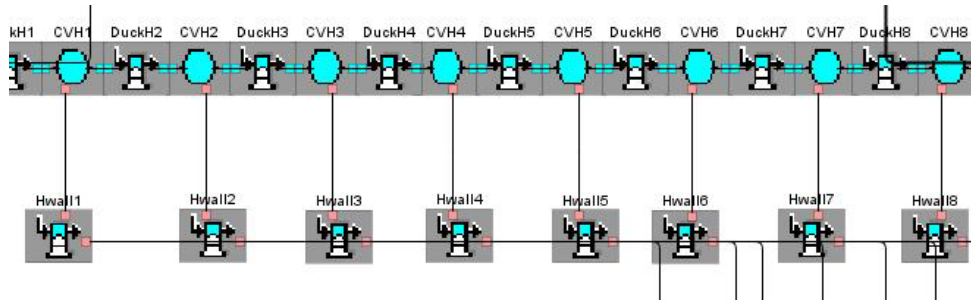


Figure 11. NPSS Cooling Jacket

The *Valve04* element modeled the pressure drop of the cooling fluid. The elements *DuckH2* in Figure 11 is an example of a *Valve04* element in the DEAN model. The *Valve04* element requires an input of the cross-sectional area and friction factor. Furthermore, a guess at the weight flow is required. The *CoolingVolume* element was used to model the change in energy of the flow. The elements *CVH1* and *CVH2* in Figure 11 are examples of this element in the DEAN model. The *CoolingVolume* element requires inputs of the volume, area, and number of channels. In addition, a guess at the total pressure and total specific enthalpy. The *Wall2* element was used to model the heat transfer from the chamber to the cooling fluid. The elements *Hwall1* and *Hwall7* in Figure 11 are examples of this element in the DEAN model. This element requires an input of the specific heat (c_p), thermal coefficient (k), and the density. Additionally, a guess of the wall temperature is required.

Other elements used in the DEAN model are the *Starter*, *Pump*, *Turb02*, and *Shaft* elements. In Figure 10, *OTNK* is an example of a *Starter* element. These elements begin and end mass flow respectively. These elements require a temperature and pressure as inputs. The *Pump* element models a fluid pump and is used for such elements as *OP* in Figure 10. This element requires an input of weight flow, gear ratio, efficiency, and

pressure rise. To model a turbine the *Turb02* element was used. One such element shown in Figure 10 is *HT*. This element requires an input of weight flow, efficiency, and pressure ratio. The *Pump* and *Turb02* element are linked by the *Shaft* element which balances the power. In Figure 10, *HSHAFT* is a *Shaft* element. This element only requires an input of the revolutions per minute (rpm).

To allow mass flow from one to another, elements are linked with *UnReactedFluidPorts*. These ports do not require any specific imports, however the user may define a parameter. Heat is passed between elements using *ThermalPorts*. Inputs for these ports include a radius of curvature, cross-sectional flow area, and a surface area.

3.6. TDK

The Two-Dimensional Kinetics (TDK) code was used to establish the contour of the aerospike nozzle. The results of this code will aid in the inputs for the nozzle in NPSS and help confirm the results obtained.

The TDK computer program represents the culmination of work done by many people over the last 35 plus years. A series of contracts funded through NASA and the ICRPG (now JANNAF) resulted in TDK becoming the JANNAF Standard Code for predicting the nozzle performance in liquid propellant rocket engines in 1967.⁴⁴ Currently, TDK is property of and under development by Software and Engineering Associates, Inc. (SEA).

The TDK program is composed of seven modules, ODE, SCAP, ODK, TRANS, MOC, BLM, and MABL. These modules allow for a complete two dimensional non-

equilibrium nozzle performance calculation with a boundary layer. Each module requires one set of inputs and can be used alone, in part, or in combination with the other modules.

3.7. Sensitivity Analysis

A sensitivity analysis on the cooling jacket was performed to focus the design changes in the cooling jacket parameters. To accomplish this, a simplified NPSS model was created with a single wall circuit for both hydrogen and oxygen flow. Figure 12 show the schematic of the sensitivity model.

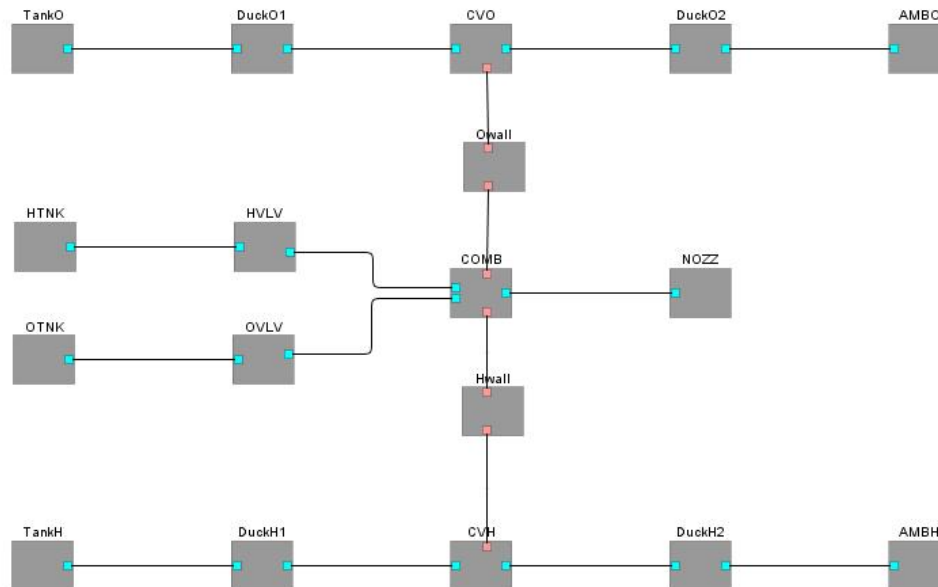


Figure 12. Sensitivity Model

The primary outputs that would be used to judge the merit of the design are the final temperature of the flow and the temperature of the wall. The final temperature must be great enough to allow the turbine to produce the required amount of horsepower to drive the pumps. The wall temperature must be sufficiently low to insure structural stability of the material. The parameters that were controlled are the mass flow, change

in pressure, cross-sectional area, and surface area. Equation 15 was used to compute the sensitivity of each parameter:

$$Sensitivity = \frac{\Delta T}{\Delta Q / Q} \quad (15)$$

In Equation 15, Q represents the parameter that was changed and T is the temperature. Table 5 and Table 6 show the initial values and the results of the sensitivity analysis.

Table 5. Hydrogen Sensitivity Analysis

Hydrogen	Original	New	T _{out} initial	T _{out} new	T _{wall} initial	T _{wall} new	T _{out} sensitivity	T _{wall} sensitivity
mdot	10.0	9.06	221.6	223.7	729.7	766.2	-22.1	-382.5
ΔP	500	700	221.6	221.2	729.7	730.2	-1.18	1.25
Cross Area	1	1.5	221.6	220.5	729.7	916.9	-2.28	374.4
Surface Area	50	55	221.6	223.9	729.7	729.1	22.4	-6.51

Table 6. Oxygen Sensitivity Analysis

Oxygen	Original	New	T _{out} initial	T _{out} new	T _{wall} initial	T _{wall} new	T _{out} sensitivity	T _{wall} sensitivity
mdot	10.0	8.44	281.1	285.1	1656	2066.1	-25.9	-2629.4
ΔP	500	700	281.1	281.2	1656	1665.5	0.313	23.75
Cross Area	1	1.5	281.1	280.4	1656	1780.6	-1.38	249.14
Surface Area	50	55	281.1	282.8	1656	1855.6	17.7	1995.6

The initial values in Table 5 and Table 6 were chosen as realistic round numbers for ease of analysis. The highlighted boxes are those that affect the temperature of the fluid and wall the most. From Table 5, a change in mass flow results in a proportionally

large change, in the opposite direction, in both the flow and wall temperature.

Additionally, a change in cross-sectional area results in a substantial change in wall temperature in the same direction. A change in surface area results in a considerable change in the flow temperature in the same direction.

From Table 6, a change in oxygen mass flow has a similar effect on the flow and wall temperature as the hydrogen mass flow. Furthermore, a change in the surface area has a significant change in both flow and wall temperature in the same direction.

Plainly, the mass flow, cross-sectional and surface area have the largest effect on the final temperature of the flow and the wall temperature.

3.8. Beginning Frame Work

The inputs to the NPSS model require many geometric inputs. Therefore, a general frame for the chamber was developed to begin the process of defining the geometry inputs for NPSS. Figure 13 shows the chamber framework.

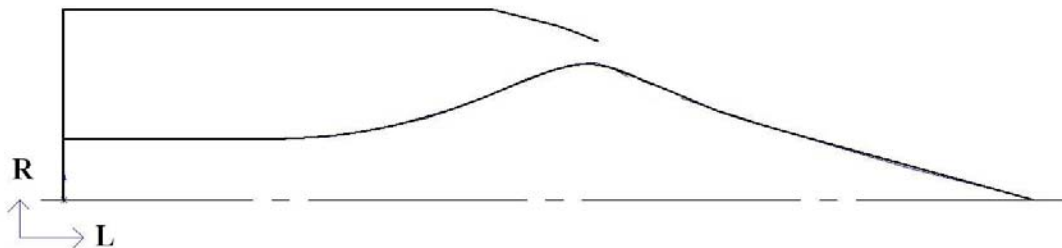


Figure 13. Initial Contour

The contour illustrated in Figure 13 helped to visualize the design of the chamber. With the framework of the chamber and nozzle; the geometry, such as the radius and length, could be adjusted based on the needs of the design. The changes would then be used to determine inputs into NPSS such as the surface area for a *ThermalPort*.

3.8.1. Cooling Channel Design

Another aspect affected by the contour of the chamber is the design of the cooling channels. The number and size of the cooling channels is constrained by the radius of the chamber at each point. Initially both milled channel and tubular channels were considered but the milled channels proved to be superior in performance and manufacturability. Figure 14 shows the cross-section used to define the cooling channel geometry.

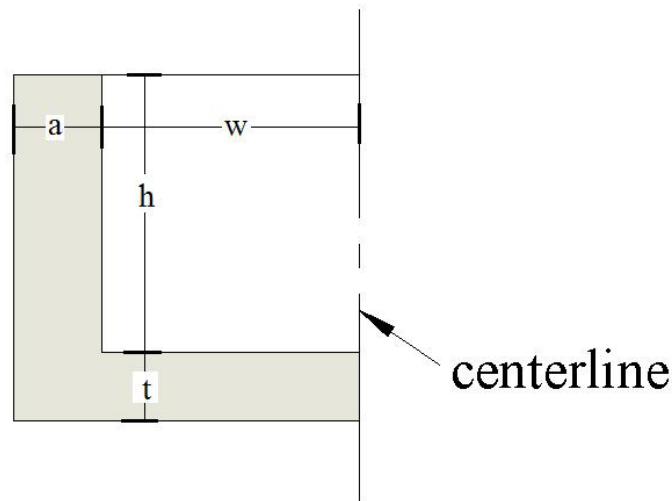


Figure 14. Cooling Channel Cross-Section

The channel depicted in Figure 14 represents half of the actual channel where it is mirrored about the centerline. The shaded region represents the solid material while the clear area is where the fluid flows. The parameter 'a' represents the half spacing between channels, 'w' is the half width, 't' is the thickness between the chamber wall and the channel, 'h' is the height of the channel. To determine the number of channels that will fit, the circumference of the chamber is divided by twice the sum of 'a' and 'w', since one channel is represented by two times their lengths.

Changing the thickness directly influences the hot and cold side wall-temperature. The ratio between ‘a’ and ‘w’ determines the total surface area of the channels thereby influencing the wall temperature and the temperature of the fluid as indicated in the sensitivity analysis. Changing the height of the chamber affects the cross-sectional area of the channel thus affecting the wall and fluid temperature as well.

3.8.2. *Material Choice*

The methodology for choosing the materials was based on the properties presented here. The material of the chamber must deal with extreme thermal and pressure forces. To handle the heat, materials with high thermal conductivity and elevated melting points were considered. These include metals like copper and nickel as well as composites like silicon carbide. Table 7 shows a list of materials and their important properties.

Table 7. Material Thermal Properties¹⁹

Material	Melting Point (R)	50% of Melting (R)	Thermal Conductivity (Btu/in*R*s)
Copper	2444.4	1222.2	0.005377
Beryllium	2790	1395	0.002682
Chromium	3812.4	1906.2	0.001257
Cobalt	3184.2	1592.1	0.00133
Iridium	4896	2448	0.001971
Molybdenum	5209.2	2604.6	0.001851
Nickel	3110.4	1555.2	0.001216
Rhodium	4024.8	2012.4	0.002012
Silicon	3033	1516.5	0.001985
Silver	2223	1111.5	0.005753
Tungsten	6588	3294	0.002333
Niobium	4933	2045	0.00072
Silicon Carbide	5580	2790	0.006571
Carbon/Carbon	4091.4	5045.7	0.02615

The 50% melting point temperature in Table 7 will be the values the wall temperature is compared to in order to determine if the material is viable given that the strength of the material should remain unchanged up to that point.

Surrounding the cooling jacket will be a structural jacket to withstand the pressure. Materials for this task will need high tensile strength to handle the pressure and low density to minimize the weight. Table 8 displays materials considered for structural support.

Table 8. Structural Materials

Material	F_{tu} (ksi)	Density (slugs/ft³)
Al 7075-T6	80	5.4
Copper	33	17
High-strength Steel	180	15.2
Nickel	110	17
Titanium	170	8.7
Tungsten	600	37
Carbon Fiber	30.5	2.72

The values in Table 8 are average values and for materials like carbon fiber, are highly dependent on the specific usages and manufacture. Another consideration for the material choice is how it reacts with oxygen. According to a NASA report,⁴⁵ materials used in an oxygen environment should have a low heat of combustion and a comparatively low burn factor. Equation 16 shows how burn factor can be defined:

$$BF = \frac{\Delta H_f^0}{\alpha} \quad (16)$$

In Equation 16, ΔH_f^0 is the heat of oxidation and α is the thermal diffusivity. Table 9 shows to compare material compatibility with oxygen.

Table 9. Oxygen Compatibility

Material	Heat of Combustion⁴⁵ (cal/g)	Heat of Formation⁴⁶ (kcal/gmole)	Thermal Diffusivity¹⁹ (m²/s)	Burn Factor
Copper	585	41.8	117	0.357
Aluminum	7425	400.4	97.1	4.12
Cobalt	970	57.1	26.6	2.15
Molybdenum	1458	182.65	53.7	3.40
Nickel	980	57.3	23	2.49
Tungsten	1093	140.94	68.3	2.06
Titanium	4710	225.5	9.32	24.19

Aluminum and Titanium are metals known to be highly reactive with oxygen. Copper and Nickel are generally unreactive with oxygen. The values in Table 9 for these materials are used as baselines to evaluate other materials. For example, Tungsten's burn factor is close to copper, therefore it would be considered compatible with oxygen. On the other hand, Molybdenum has a burn factor closer to aluminum and consequently would be considered to be reactive with oxygen. On the composite side, Schoenman⁴⁵ states that silicon carbide is compatible with use in oxygen environments.

4. Analysis and Results

4.1. Chapter Overview

This Chapter presents the results obtained from NPSS and TDK for the DEAN described in the methodology of Chapter three. The NPSS model of the DEAN consists of five major components; the oxygen turbo machinery, the oxygen cooling jacket, the hydrogen turbo machinery, the hydrogen cooling jacket, and the chamber/nozzle. The turbo machinery is analyzed in related documents by Capt Michael Arguello⁴⁷ for the hydrogen side and Capt William Strain⁴⁸ for the oxygen side. Presented below are the results pertaining to the cooling jackets and the chamber/nozzle. The code that produced these results is presented in Appendix C.

4.2. Results of Simulation Scenarios

The chamber and nozzle contour was defined to determine the geometric inputs for NPSS and visualize the design of the DEAN. Figure 15 shows the final contour of the chamber/nozzle used in the NPSS model.

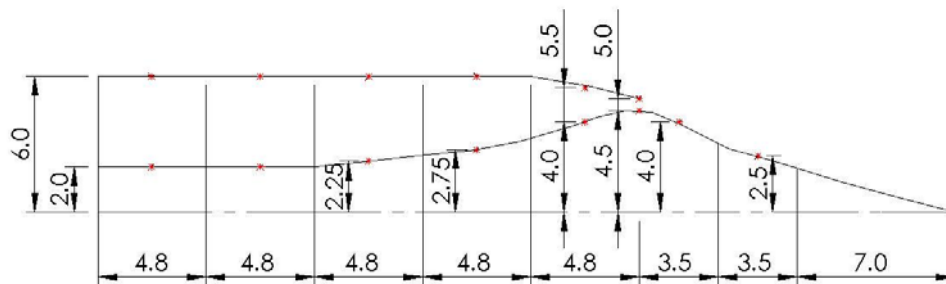


Figure 15. Chamber/Nozzle Contour (all dimension in inches)

Figure 15 shows the chamber/nozzle split into several segments. Splitting the contour into segments allowed for a profile of the wall and fluid temperature along the length of the contour. The chamber is split into five equal length sections with an additional section at the throat since that point usually experiences the most extreme temperatures. The nozzle is split into three sections with the two equal length sections being cooled and the last section not cooled. The mid-points shown in Figure 15 represent the points where the geometry for the elements are defined for each section.

4.2.1. Hydrogen Cooling Jacket Results

The hydrogen cooling-jacket performs the task of cooling the inner chamber wall and part of the nozzle while providing energy to the hydrogen turbine to power the pumps. The hydrogen flow is split 50/50 after the first pump as shown in Figure 10. The result is a mass flow of 7.55 lbm/s (3.42 kg/s) for cooling. The cooling jacket consists of the elements between the second pump and turbine. The *DuckH#* elements are *Valve04* elements and are responsible for the pressure drop in the jacket. The pressure drops from 4050 psi (27.9 MPa) at the exit of the second pump to 3625 psi (25 MPa) at the inlet of the turbine. The friction factor (K) of the elements is set to allow for a constant pressure drop through the jacket.

The *CoolingVolume* elements attracted to the *Wall2* elements allow for the heat transfer from the chamber to the fluid. These elements consist of *CVH#* and *Hwall#* elements. There are a total of 314 channels with the dimensions of the channels changing for each element as revealed in Table 10.

Table 10. Hydrogen Channel Dimensions

Element	r (in)	a (in)	w (in)	h (in)	A (in ²)	AR
CVH1	2.5	0.01	0.015	0.02	0.19	1.33
CVH2	4	0.01	0.03	0.02	0.38	0.67
CVH3	4.5	0.01	0.035	0.02	0.44	0.57
CVH4	4	0.01	0.03	0.02	0.38	0.67
CVH5	2.75	0.01	0.0175	0.03	0.33	1.71
CVH6	2.25	0.01	0.0125	0.04	0.31	3.2
CVH7	2	0.01	0.01	0.05	0.31	5
CVH8	2	0.01	0.01	0.05	0.31	5

The variables in Table 10 correspond to Figure 14, r is the radius and A is the total cross-sectional area of the cooling flow. The change in dimension in Table 10 represents the change in priority of the channel along the contour of the chamber. At the throat, *CVH3*, the AR is lowest to allow for maximum heat transfer and minimum wall temperature. At the end of the flow, *CVH8*, the concern is preventing the flow from going supersonic. A shock wave in the channel would greatly increase the pressure loss and may also cause damage to the structure. Table 11 shows the Mach number for each element.

Table 11. Hydrogen Mach Numbers

Element	P (psi)	T (R)	V (ft/s)	a (ft/s)	Mach #
CVH1	4002	145.3	1630	4556.4	0.35
CVH2	3954	270.6	1336	4338.5	0.30
CVH3	3907	276.6	1185	4333	0.27
CVH4	3860	415.7	1972	4689.1	0.42
CVH5	3813	477.2	2584	4870.7	0.53
CVH6	3766	524.9	3029	5012.1	0.60
CVH7	3719	567.4	3278	5137.1	0.63
CVH8	3672	609.7	3532	5260.7	0.67

In Table 11, the pressure, temperature and velocity are the exit properties of each element. The values for speed of sound (a) come from the National Institute of Standards

and Technology (NIST)⁴⁹ database for hydrogen for the specific pressure and temperature. The greatest Mach number is 0.67 at the end of the cooling jacket and is not high enough to cause any issues associated with shock waves. The Mach number is not a issue for hydrogen till around 0.9, therefore there is some leeway were this is concerned.

The heat flow and heating coefficients used to calculate the wall temperature are outputs from the NPSS model. However, the wall temperature NPSS calculates is only a balance of heat in and out of the wall and does not take into account material properties. To calculate the wall temperature for different materials another calculation is required. The calculation balances the three heat equations shown in Equation 17 originating from Equations 7 and Equation 8:

$$q = h_H A_H (T_H - T_{WH}) = k A_H \left(\frac{T_{WH} - T_{WC}}{t} \right) = h_C A_C (T_{WC} - T_C) \quad (17)$$

In Equation 17, q , h_H , h_C , A_H , A_C , T_H , and T_C come from the NPSS model. The value for k is dependent of the material chosen, and t is set to 0.02 in (0.508 mm) for the design of the cooling jacket. The results for various materials are presented in Appendix E. Figure 16 shows the graph of the wall temperature for copper along the axial coordinate.

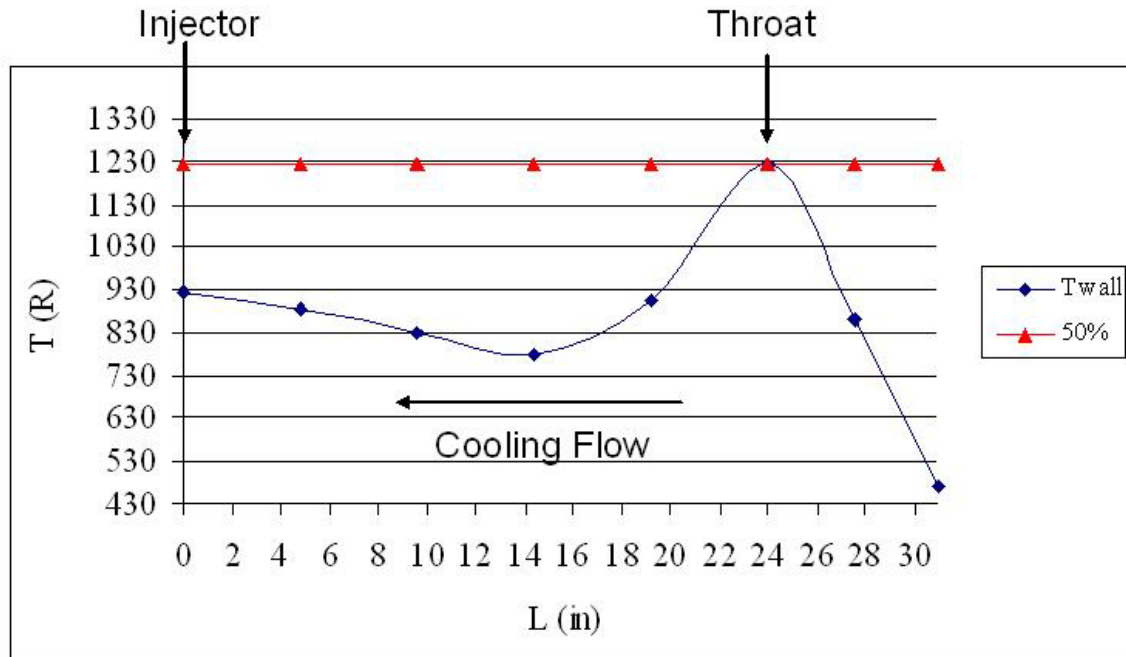


Figure 16. Hydrogen Wall Temperatures

In Figure 16, the injector faceplate is at zero and the beginning of the cooling circuit in the nozzle is at 31 in (0.787 m) (the hydrogen travels from right to left). The throat is at 24 in (0.61 m). As expected the hottest wall temperature is at the throat at 1224 R (680 K). The 50% melting point for copper is 1222 R (678 K). The calculated temperature of the wall is within a percent of the 50% melting point of copper, hence in the current configuration the wall temperature maintains a reasonable level during normal operation.

The final requirement for the cooling jacket to meet is the temperature of the flow entering the turbine. Table 12 shows the outlet temperature of each element.

Table 12. Hydrogen Flow Temperature

Element	T (R)
CVH1	145.3
CVH2	270.6
CVH3	276.6
CVH4	415.7
CVH5	477.2
CVH6	524.9
CVH7	567.4
CVH8	609.7

Table 12 shows the temperature into the cooling jacket is 145.3 R (80.7 K) at the subsequent rise in temperature to The result is a temperature raise of 464.3 R (257.9 K). The temperature into the turbine is 609.7 R (338.7 K) that allowed the turbine to produce 3573 hp, adequate to power the hydrogen pumps.

4.2.2. Oxygen Cooling Jacket Results

The oxygen cooling-jacket is responsible for cooling the outer chamber wall and providing energy to the oxygen turbine to power the pump. Unlike the hydrogen, 100% of the oxygen flows through the jacket as illustrated in Figure 10. The result is a mass flow of 106 lbm/s (48.08 kg/s) for cooling. The cooling jacket consists of the elements between the pump and turbine. The *DuckO#* elements perform the same task of pressure drop like the *DuckH#* elements. The pressure drops from 4635 psi (31.9 MPa) at the exit of the pump to 3666 psi (25.2 MPa) at the inlet of the turbine.

The elements of *CVO#* and *Owall#* elements perform the same as *CVH#* and *Hwall#* elements. The oxygen cooling-jacket has 785 channels with the dimensions of the channels changing for each element as revealed in Table 13.

Table 13. Oxygen Channel Dimensions

Element	r (in)	a (in)	w (in)	h (in)	A (in²)	AR
CVO1	5	0.01	0.01	0.03	0.47	3
CVO2	5.5	0.01	0.012	0.04	0.75	3.33
CVO3	6	0.01	0.014	0.04	0.88	2.86
CVO4	6	0.01	0.014	0.04	0.88	2.86
CVO5	6	0.01	0.014	0.04	0.88	2.86
CVO6	6	0.01	0.014	0.05	1.1	3.57

The variables in Table 13 are the same as Table 10. The change in dimension in Table 13 are due to the same factors that influence the change in AR seen in Table 10. Table 14 shows the Mach number for each element.

Table 14. Oxygen Mach Numbers

Element	P (psi)	T (R)	V (ft/s)	a (ft/s)	Mach #
CVO1	4497	179.3	448.2	3186.3	0.14
CVO2	4359	303.9	379.8	1980.1	0.19
CVO3	4221	379.6	428.1	1497.1	0.28
CVO4	4084	452.2	576.2	1326.1	0.43
CVO5	3947	531.4	758.3	1321.6	0.57
CVO6	3809	616.8	764.3	1354.6	0.56

In Table 14, the pressure, temperature and velocity are the exit properties of each element. The values for speed of sound are for oxygen at the specified pressure and temperature. The greatest Mach number is 0.57 at *CVO5* and is not high enough to cause any issues as stated earlier with the hydrogen side. The Mach number becomes an issue at around 0.6 for oxygen. Therefore, this design is at the high end of what is expectable.

The wall temperature for the oxygen side is computed using Equation 17 similar to the hydrogen side. The results for various materials are presented in Appendix E. Figure 17 shows the graph of the wall temperature for silicon carbide along the axial coordinate.

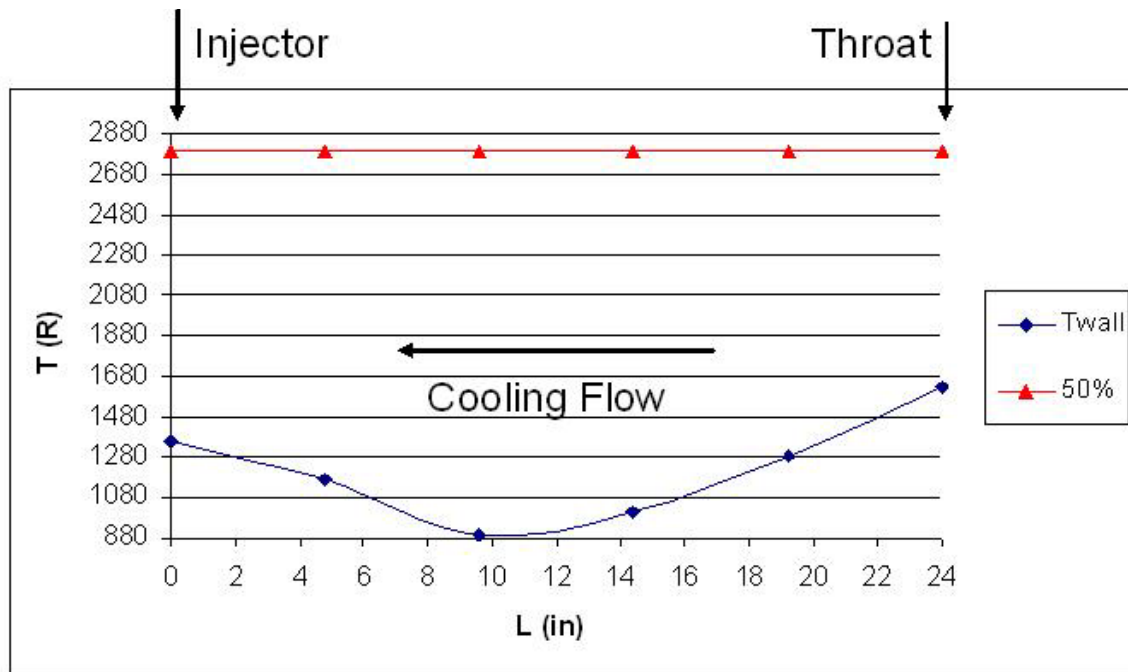


Figure 17. Oxygen Wall Temperatures

In Figure 17 the injector faceplate is at 0 inches and the beginning of the cooling circuit in the throat is at 24 inches (0.61 m) (the oxygen travels from right to left). Silicon carbide is an expensive and exotic material, however, lower cost alternatives were unable to meet the performance requirements. Additionally, silicon carbide is known to work well with oxygen, that was a consideration outlined in section 3.8.2. Silicon carbide has been successfully tested with an actively cooled configuration.⁵⁰ Therefore, it is manufacturable although it may be expensive. Another material that might work is tungsten. According to the burn factor presented in Chapter three, tungsten should be compatible with oxygen but the manufacture may present problems.

As expected the hottest wall temperature is at the throat at 1625 R (902 K). The 50% melting point for silicon carbide is 2790 R (1550 K). The calculated temperature of the wall is 34 % lower than the 50% melting point of silicon carbide; hence, in the current

configuration the wall temperature maintains a reasonable level during normal operation and allows room for growth.

The final requirement for the cooling jacket to meet is the temperature of the flow entering the turbine. Table 15 shows the outlet temperature of each element.

Table 15. Oxygen Flow Temperature

Element	T (R)
CVO1	179.3
CVO2	303.9
CVO3	379.6
CVO4	452.2
CVO5	531.4
CVO6	616.8

Table 15 reveals the temperature into the cooling jacket is 179.3 R (99.6 K) and increases along the jacket to a final temperature of 616.8 R (342.6 K). The result is a temperature rise of 437.4 R (243 K) in the jacket. The temperature out of the cooling jacket allowed the turbine to produce 2587 hp, sufficient to power the oxygen pump.

4.2.3. Chamber/Nozzle Results

The hydrogen and oxygen flow into the chamber and combust, and then expand through the nozzle. The elements of interest are the *COMB* and *NOZZ* elements as depicted in Figure 10. The *COMB* element has an input of C_O2_H2 as the composition to designate that the reaction is of hydrogen and oxygen and the radius of the chamber is 6 inches. The *NOZZ* element has inputs of 15.9 in² for the throat area, 125 for the expansion ratio, and 0.1 psi for the ambient pressure. Both elements have thermal ports that are connected to *Wall2* elements for heat transfer. The inputs for radius of curvature,

flow area, and surface area (areaHx in the code) come from Figure 15. The results for these elements are presented in Table 16.

Table 16. Chamber Performance

O/F	7.03			
P_c	1739.1	<i>psi</i>	12	<i>MPa</i>
T_c	6586.3	<i>R</i>	3659	<i>K</i>
F_g	57231.9	<i>lbf</i>	254	<i>kN</i>
Total mass flow	121.1	<i>lbm/s</i>	54.9	<i>kg/s</i>
Hydrogen mass flow	15.1	<i>lbm/s</i>	6.8	<i>kg/s</i>
Oxygen mass flow	106	<i>lbm/s</i>	48.1	<i>kg/s</i>
I_{sp}	472.7	<i>sec</i>		

Table 16 show this model meets the thrust and I_{sp} goals set forth in Chapter 1. Specifically, the thrust goal is 50,000 lbf (222.4 kN), while the result from the DEAN NPSS model is 57,231 lbf (254 kN). This is a 14% increase in thrust over the goal. The I_{sp} goal is 464 sec whereas the DEAN Isp from the NPSS model is 472.7 sec. This is a 1.9% increase in I_{sp} over the goal. The increase of the thrust and I_{sp} over the goal values shows the model performs better than expected. Additionally, the values for the chamber are close to the initial parameters shown in Table 4. The O/F is 7.03 in the model while the initial value was seven. The chamber pressure of 1739 psi (12 MPa) is within one psi of the initial selection. This demonstrates the initial assumptions were sound and the NPSS chamber model performs close to what was projected.

4.2.4. TDK Nozzle

TDK 04 determined the contour of the nozzle. The code developed for the DEAN is given in Appendix C. In developing the code, the goal was to match many of the chamber properties, such as pressure and temperature, to the NPSS model. TDK then generated a nozzle based on these properties and non-dimensionalized by the throat

radius. The contour is then incorporated into the design. The code developed results in the following parameters in Table 17.

Table 17. TDK Properties

P_c	1739	<i>psi</i>	12	<i>Mpa</i>
T_c	6586	<i>R</i>	3659	<i>K</i>
O/F	7			
Mdot	121.1	<i>lbm/s</i>	54.9	<i>kg/s</i>
F_g	66167	<i>lbf</i>	294	<i>kN</i>
I_{sp}	546	<i>s</i>		

Table 17 illustrates the chamber properties for NPSS and TDK are the same. However, the I_{sp} and thrust calculated by TDK is much larger than the NPSS model. Some difference is due to the differences in methods of TDK and NPSS. Nevertheless, the TDK I_{sp} is still above the theoretical limit of 500 sec for an O_2/H_2 engine. This is explained by the fact that the presented I_{sp} is that of the entire control volume TDK used to make calculations and therefore is inflated. Still, the definition of the control volume is unclear in the output so real I_{sp} remains unknown. The nozzle contour was still used for NPSS since the mass flows matched. Figure 18 shows the non-dimensional contour with a temperature profile.

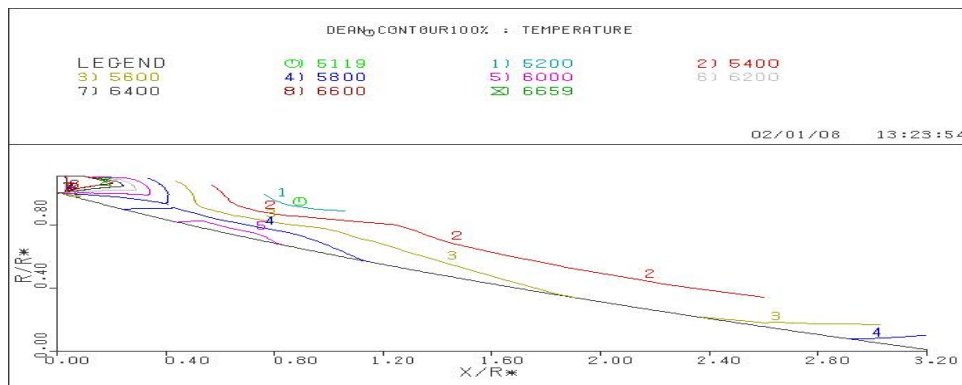


Figure 18. Non-dimensional Nozzle Contour with Temperature Profile

Figure 18 reveals the length of the nozzle is about three times the radius at the throat. Additionally, Figure 18 shows the change in temperature along the nozzle contour and is the reason for part of the nozzle being actively cooled due to the decrease in the temperature of the flow.

Truncation is ending the nozzle before the flow is fully expanded. Figure 19 show a truncated nozzle.

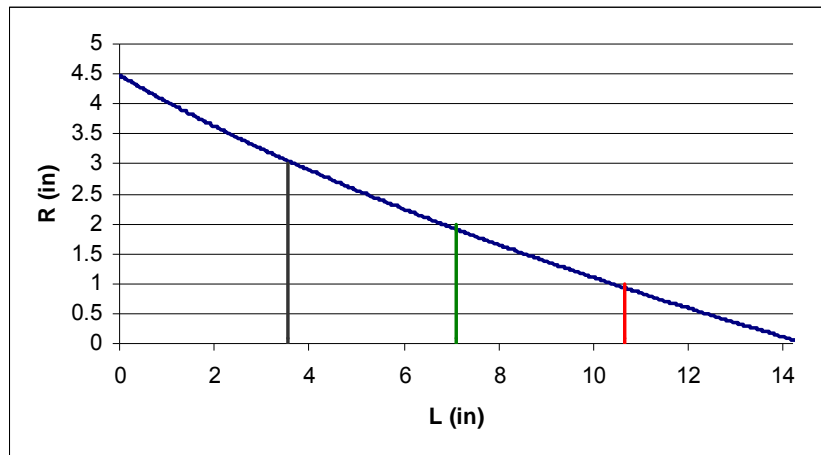


Figure 19. Truncated Nozzle

In Figure 19, the red line denotes a length of 75% of a fully contoured nozzle, the green line 50% and the black line 25%. To determine the affect of truncation, a model where the ratio of length to throat radius varies was created. Table 18 shows the relation of nozzle length to I_{sp} and mass.

Table 18. Truncation of Nozzle

L	I_{sp} (s)	ΔI_{sp} (s)	Mass (lbm)	ΔMass
100%	546		1.05	
75%	548	2	0.96	8.5%
50%	545	-1	0.65	38%
25%	537	-9	0.38	64%

The mass in Table 18 assumes niobium, 0.3096 lbm/in^3 (8570 kg/m^3), is used for the entire nozzle with a throat radius of one inch. Niobium (columbium) is chosen since it is the material for the un-cooled section of the nozzle and results in quicker calculations. Table 18 indicated truncation of the nozzle by 75% results in a 0.4% increase in I_{sp} and a 8.5% decrease in mass. Why the I_{sp} increased may be due to the same factors causing the I_{sp} to be inflated over the theoretical maximum. Further reduction in length behaved as expected with a 0.2% and 1.6% decrease in I_{sp} with a 38% and 64% decrease in weight for 50% and 25% of the total length respectively. The results indicate truncation of the nozzle has little impact on I_{sp} . However, as indicated in Chapter 1, even a small change in I_{sp} has a major impact on the capabilities of the launch vehicle. Therefore, at this point the design will utilize the full-length nozzle. Figure 20 illustrates the full-length nozzle contour for the DEAN design.

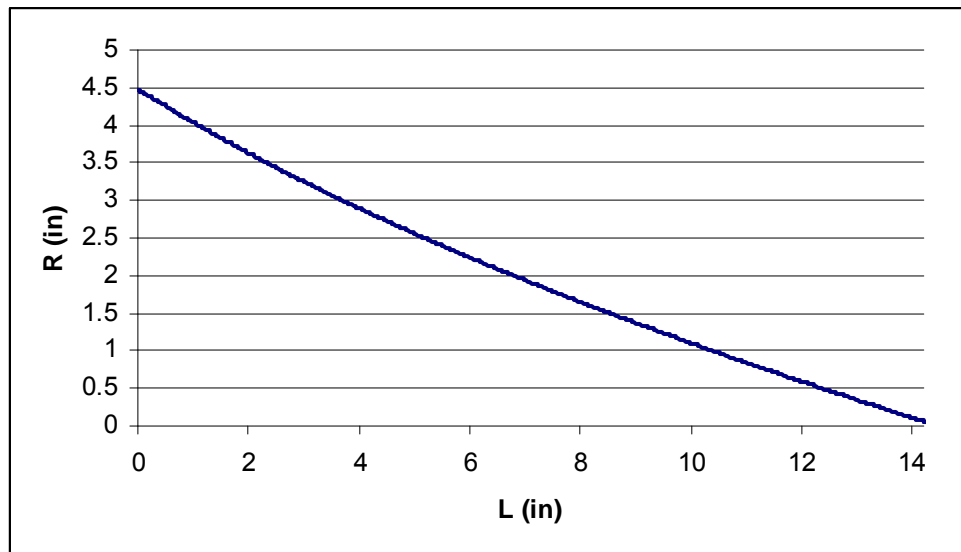


Figure 20. Nozzle Contour

The contour in Figure 20 comes from the contour of the TDK code presented in Appendix C. This code matches the chamber pressure, chamber temperature, and mass

flow between NPSS and TDK outputs. The non-dimensional contour in this code is dimensioned with the throat radius of 4.46 in. With an outer radius of five inches, the throat area is 15.9 in^2 , which is the area input in NPSS.

4.3. Investigative Objectives

This investigation tried to meet three objectives:

1. Determine feasibility of meeting the IHRPT Phase III orbit transfer vehicle goals with the DEAN concept
2. Implement and improve upon a design process focused on the energy conversion section of a rocket engine (combustion chamber, nozzle)
3. Perform detailed design analysis of the energy transfer components (cooling jackets) making the DEAN possible

The result of the NPSS model showed that this model is able to meet the IHRPT Phase III goals and detailed to analysis of the energy conversion and energy transfer components. The result is the conceptual solid model of the DEAN shown in Figure 21.

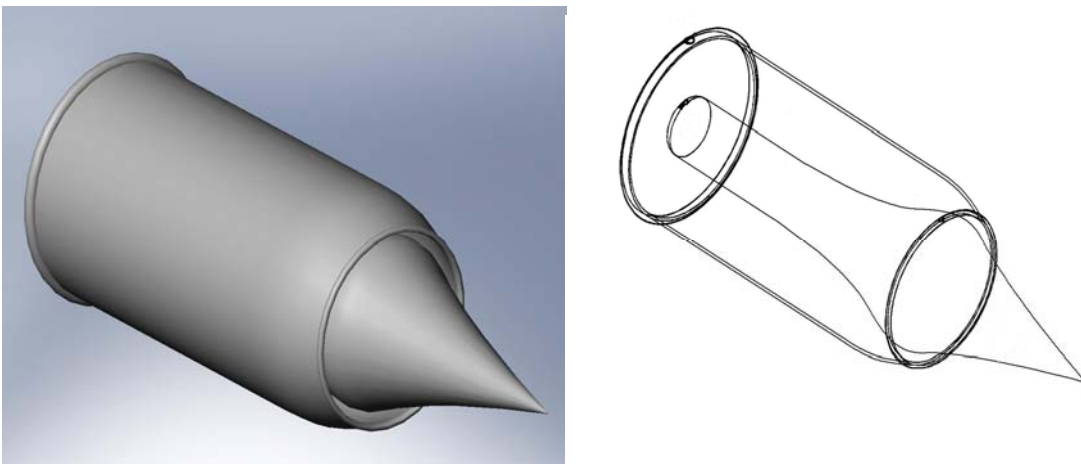


Figure 21. The DEAN

The left portion of Figure 21 shows the solid model while the right portion depicts a line drawing showing the inside of the chamber. Figure 21 illustrates the full-length aerospike nozzle developed by TDK and the chamber designed by NPSS. The outer wall of the chamber consists of a silicon carbide cooling jacket with an estimated mass of 5.96 lbm (2.7 kg). Around the cooling jacket is a structural jacket. The structural jacket is sized as a pressure vessel using Equation 18:

$$t_w = \frac{P_b r_c}{F_{tu}} \quad (18)$$

In Equation 18, t_w is the wall thickness, r_c is the radius of the chamber, F_{tu} is the ultimate tensile strength of the material, and P_b is the burst pressure. The burst pressure is the chamber pressure multiplied by a factor of safety, in the case of the DEAN, the factor of safety is 1.5. Different materials were evaluated to minimize thickness and weight. Aluminum 7075-T6, with an F_{tu} of 80 ksi (555.1 MPa), was judged the best with a thickness of 0.2 in (0.5 cm) and a mass of 13.2 lbm (6 kg). The cooled part of the nozzle and inner wall is composed of copper resulting in a mass of about 69 lbm (31.3 kg). The un-cooled portion of the nozzle is niobium and has a mass of 2.3 lbm (1.05 kg). The total mass of the chamber/nozzle is estimated at 90.5 lbm (41.05 kg). Combined with the oxygen turbo machinery at 137.3 lbm (62.3 kg) and hydrogen turbo machinery of 251.1 lbm (113.9 kg) results in an estimated total mass of 478.9 lbm (217.2 kg) for the DEAN rocket engine concept. This results in a thrust to weight ratio of 119:1.

4.4. Summary

NPSS was used to model the DEAN. This model resulted in several significant results. The DEAN model produces 57,231 lbf (254 kN) of thrust with an I_{sp} of 472.7

sec. The hydrogen cools the inner wall of the chamber and part of the nozzle with a mass flow of 7.55 lbm/sec (3.42 kg/sec). The cooling jacket increases the flow temperature by 464 R (257.8 K). The walls are made of copper and have a maximum temperature of 1224 R (680 K) at the throat. The oxygen cools the outer wall of the chamber with a mass flow of 106 lbm/sec (48.1 kg/sec). The cooling jacket increases the flow temperature by 437.4 R (243 K). The cooling channels walls consist of silicon carbide and have a maximum temperature of 1625 R (902.8 K) at the throat. Due to the accuracy of NPSS, it is expected that the numbers presented would closely match the results and actual working engine.

5. Conclusions and Recommendations

5.1. Chapter Overview

The DEAN is a dual-expander aerospike nozzle design providing superior performance to the current upper stage fleet. The conclusion and recommendations based on the work done in this document are presented here.

5.2. Conclusions of Research

Based on the results presented in Chapter 4, the DEAN would meet and exceed the IHPRT phase III goals. Additionally, a dual-expander cycle with separate turbines for the fuel and oxidizer flow is possible since the amount of heat captured from the chamber is sufficient to increase the flows to the required temperature. Additionally, though the learning curve is steep, NPSS has proven to be a powerful tool in the development of rocket engines. TDK was easier to learn in comparison, however, its ability to model aerospike nozzles was left wanting due to the confusing I_{sp} result.

5.3. Significance of Research

The work contained within this document could result in significant gains in performance for the Delta and Atlas platforms. Based on the current Centaur upper stage, the DEAN model would result in a 28.3 s increase in I_{sp} . This could result in as much as a 3,806 lbm (1726 kg) increase in satellite mass to orbit. In addition, the DEAN has the potential to save around \$19 million per launch based on the savings per I_{sp} presented in Chapter 1.

5.4. Recommendations for Future Research

The work presented in this document is for the initial design concepts. Therefore, it is recommended further research be done based on this model of the DEAN to complete the design process. For one, the discrepancy between the I_{sp} from the NPSS and TDK model should be resolved. Work was done on an elements for NPSS that allows NPSS to run TDK. At this point the element has not successfully run. Getting this element to run should result in a improve idea of the I_{sp} of the DEAN design and whether truncation of the nozzle is necessary.

Even though NPSS is a powerful tool, it has some limitation. For example, it cannot show the effects the curvature of the chamber will have on the cooling jacket and the combustion. Therefore, a detailed analysis of the flow within the cooling jacket to confer the properties of the flow obtained from NPSS. This would include a CFD analysis of the fluid flow to depict the flow filed in the chamber as well as the cooling jackets. The CFD model will result in a high fidelity model for the properties of the chamber and their effect on the cooling jacket.

Furthermore, in this document the incorporation of the injector design only resulted in the assumption of the pressure drop across the injector and efficiency of combustion. A detailed investigation on the benefits of a Pintle or Coaxial injectors into the DEAN design should be undertaken. This will determine the type of injector that should be used on the design and a detailed design of the injectors.

The work done in this document only details a design at a single point. Therefore, further work on the DEAN should involve on investigation on off-design conditions. This is required to outline the ability for the model to meet throttling requirements. To

ensure the DEAN design is the best it can be, and optimization of the current design should be undertaken. The optimization would determine the aspects of each component that results in the overall best engine design. Aspects to consider are, but not limited to, the amount of truncation of the nozzle, optimal O/F and ϵ , and material choices for the walls.

Another aspect of the design to consider is the possible use of fuels other than hydrogen. One fuel the space command has expressed interest in is the use of methane since it is easier to store than liquid hydrogen..

5.5. Summary

In conclusion, with the incorporation of state of the art turbo machinery, and the use of the aerospike nozzle, the proposed upper stage design of the DEAN achieves a performance that could radically enhance the current space launch fleet. The DEAN model resulted in 57,231 lbf (254 kN) of thrust, 14% over the goal, and an I_{sp} of 472.7 sec, 1.9% increase over the goal. In addition, the walls of the chamber and nozzle were adequately cooled to prevent the failure and provided the necessary energy to the fuel and oxidizer turbine.

Appendix A : Lessons Learned

In the execution of the experiment detailed in this report, several lessons were learned. Most of these lessons deal with the use of NPSS and TDK.

A.1 NPSS Lessons Learned

NPSS is a great tool, though the learning curve is steep. First, it is best not to use the graphic-user-interface (GUI) when coding. The GUI is useful when viewing the schematic of the code, editing, and viewing the results of the code. However, when using it to write the code it often adds needless lines confusing more than enhancing the code.

A major revelation was the elements are defined by '.int' files and were located in a folder within NPSS. Before this revelation, the coefficients NPSS uses were confusing, seemed unrelated to any known coefficients, and were not explained anywhere in the documentation provided with NPSS. However, in the '.int' files, the equations in each element are defined and the coefficient values were revealed. Though the user input coefficients were convoluted, the results of the inputs were predictable.

One drawback is NPSS only uses English units. The use of English units can unduly confuse the problem. It would have been useful to include either SI elements, or elements able to use either unit.

The caveat to all this is NPSS allows for the user to code there own '.int' files. Therefore, any complication can be overcome with the user creating their own elements. However, this effort takes away from the actual design since time is spent fixing NPSS. Additionally, learning NPSS is difficult enough, let alone creating new elements.

A.2 TDK Lessons Learned

TDK is a powerful program for analyzing nozzles. One useful thing would have been graphing of the chamber as well as the nozzle. One realization in using the code was TDK is very sensitive to the wall contour. Unlike some programs continuing to work even if the physics are impossible, TDK aborts the code if the wall fails. This can be frustrating when trying to design a nozzle since the contour is unknown often leaving the researcher with a mystery as to the fix to the problem.

The ability for TDK to model aerospike nozzles is relatively unique. However, the aerospike is a feature of the scramjet modeling capability. Some complications arise since the scramjet is an aero-device while the aerospike is a rocket device. This creates confusion since the scramjet burns with air while the aerospike does not use air. It is recommended future releases of TDK have a separate aerospike function.

Appendix B : NPSS Code

This is the NPSS code that defines the DEAN model. This code requires the use of modified elements developed by Tom Lavelle at NASA Glen. When opened in NPSS these files will generate data presented in this report.

B.1 Final Model Code

```
//=====
// Air Force Institute of Technology
// 2950 Hobson Way, Bldg 641
// Wright Patterson AFB, OH 45433
//
// David F. Martin II, 2Lt., USAF
//=====
//=====
// Goals
//=====
real mdot = 121.25;
real P_c = 1740.5;
real O_F = 7;
real A_throat = 15.9;
real epsilon = 125;

#include "Pump.int";
#include "Turb02.int";
#include "CoolingVolume.int";
real mdotO = 106;
real mdotH = 15.1;
real Wall_temp = 900;
//=====
// Chamber
//=====
setDefaultComposition("C_O2_H2");

RocketComb1 COMB {
  comp = "C_O2_H2";
  radius_tc = 6.0;
  volume = 2075.44;
  Fu_I.comp = "HYDROGEN";
  FI_oxid.comp = "OXYGEN";
  ThermalOutputPort Hx_zoneO1 {
    areaFlow = 32*PI;
    areaHx = 180.96;
    radCurv = parent.radius_tc;
  };
  ThermalOutputPort Hx_zoneO2 {
    areaFlow = .COMB.Hx_zoneO1.areaFlow;
    areaHx = .COMB.Hx_zoneO1.areaHx;
```

```

        radCurv = parent.radius_tc;
    };
    ThermalOutputPort Hx_zoneO3 {
        areaFlow = 97.193;
        areaHx = .COMB.Hx_zoneO1.areaHx;
        radCurv = parent.radius_tc;
    };
    ThermalOutputPort Hx_zoneO4 {
        areaFlow = 89.339;
        areaHx = .COMB.Hx_zoneO1.areaHx;
        radCurv = parent.radius_tc;
    };
    ThermalOutputPort Hx_zoneO5 {
        areaFlow = 44.76;
        areaHx = 165.88;
        radCurv = 5.5;
    };
    ThermalOutputPort Hx_zoneO6 {
        areaFlow = A_throat+3;
        areaHx = 3.14;
        radCurv = 5;
    };
    ThermalOutputPort Hx_zoneH1 {
        areaFlow = 32*PI;
        areaHx = 60.32;
        radCurv = 2;
    };
    ThermalOutputPort Hx_zoneH2 {
        areaFlow = .COMB.Hx_zoneH1.areaFlow;
        areaHx = .COMB.Hx_zoneH1.areaHx;
        radCurv = .COMB.Hx_zoneH1.radCurv;
    };
    ThermalOutputPort Hx_zoneH3 {
        areaFlow = 97.19;
        areaHx = 67.86;
        radCurv = 2.25;
    };
    ThermalOutputPort Hx_zoneH4 {
        areaFlow = 89.33;
        areaHx = 82.94;
        radCurv = 2.75;
    };
    ThermalOutputPort Hx_zoneH5 {
        areaFlow = 44.76;
        areaHx = 120.64;
        radCurv = 4;
    };
    ThermalOutputPort Hx_zoneH6 {
        areaFlow = A_throat+3;
        areaHx = 2.83;
        radCurv = 4.5;
    };
}

```

```

RocketNozzle NOZZ {
  Ath = A_throat;
  AR = epsilon;
  Ps = 0.01;
  ThermalOutputPort Hx_zoneH7 {
    areaFlow = A_throat*2;
    areaHx = 87.96;
    radCurv = 4;
  };
  ThermalOutputPort Hx_zoneH8 {
    areaFlow = A_throat*4;
    areaHx = 54.98;
    radCurv = 2.5;
  };
}

//=====
// Opump
//=====
setDefaultComposition("OXYGEN");
Element Starter TankO {}

Element Valve04 OD1 {
  Across = 2;
  K = 0.0116;
}

Element CoolingVolume OCV1 {
  UnReactedFluidInputPort FI_I;
  UnReactedFluidOutputPort FI_O;
  volume = 10;
  Aphys = 2.112;
}

Element Pump OP {
  gearRatio = 1;
  W = mdotO;
  eff = 0.773;
  PRdes = 103;
}

Element CoolingVolume OCV2 {
  UnReactedFluidInputPort FI_I;
  UnReactedFluidOutputPort FI_O;
  volume = 10;
  Aphys = 1.71;
}

//=====
// Cooling Jacket1
//=====
Element Valve04 DuckO1 {
  Across = 0.47;
  K = 0.0888;
}

```

```

Element CoolingVolume CVO1 {
  UnReactedFluidInputPort FI_I {OFR = 1;};
  UnReactedFluidOutputPort FI_O {OFR = 1;};
  ThermalOutputPort Hx_zone1 {areaHx = 1.57;};
  volume = 0.05;
  n_channels = 785;
  Aphys = 0.47;
}

Element Valve04 DuckO2 {
  Across = .CVO1.Aphys;
  K = 0.0879;
}

Element CoolingVolume CVO2 {
  UnReactedFluidInputPort FI_I {OFR = 1;};
  UnReactedFluidOutputPort FI_O {OFR = 1;};
  ThermalOutputPort Hx_zone1 {areaHx = 90.43;};
  volume = 3.62;
  n_channels = .CVO1.n_channels;
  Aphys = 0.75;
}

Element Valve04 DuckO3 {
  Across = .CVO2.Aphys;
  K = 0.165;
}

Element CoolingVolume CVO3 {
  UnReactedFluidInputPort FI_I {OFR = 1;};
  UnReactedFluidOutputPort FI_O {OFR = 1;};
  ThermalOutputPort Hx_zone1 {areaHx = 105.5;};
  volume = 4.22;
  n_channels = .CVO1.n_channels;
  Aphys = 0.88;
}

Element Valve04 DuckO4 {
  Across = .CVO3.Aphys;
  K = 0.172;
}

Element CoolingVolume CVO4 {
  UnReactedFluidInputPort FI_I {OFR = 1;};
  UnReactedFluidOutputPort FI_O {OFR = 1;};
  ThermalOutputPort Hx_zone1 {areaHx = 105.5;};
  volume = 4.22;
  n_channels = .CVO1.n_channels;
  Aphys = 0.88;
}

Element Valve04 DuckO5 {
  Across = .CVO4.Aphys;

```

```

    K = 0.127;
}

Element CoolingVolume CVO5 {
    UnReactedFluidInputPort FI_I {OFR = 1;};
    UnReactedFluidOutputPort FI_O {OFR = 1;};
    ThermalOutputPort Hx_zone1 {areaHx = 105.5;};
    volume = 4.22;
    n_channels = .CVO1.n_channels;
    Aphys = 0.88;
}

Element Valve04 DuckO6 {
    Across = .CVO5.Aphys;
    K = 0.0968;
}

Element CoolingVolume CVO6 {
    UnReactedFluidInputPort FI_I {OFR = 1;};
    UnReactedFluidOutputPort FI_O {OFR = 1;};
    ThermalOutputPort Hx_zone1 {areaHx = 105.5;};
    volume = 5.28;
    n_channels = .CVO1.n_channels;
    Aphys = 1.10;
}

Element Valve04 DuckO7 {
    Across = .CVO6.Aphys;
    K = 0.125;
}

Element Wall2 Owall1 {
    ThermalInputPort CoolSide1;
    ThermalInputPort HotSide1;
}
Element Wall2 Owall2 {
    ThermalInputPort CoolSide1;
    ThermalInputPort HotSide1;
}
Element Wall2 Owall3 {
    ThermalInputPort CoolSide1;
    ThermalInputPort HotSide1;
}
Element Wall2 Owall4 {
    ThermalInputPort CoolSide1;
    ThermalInputPort HotSide1;
}
Element Wall2 Owall5 {
    ThermalInputPort CoolSide1;
    ThermalInputPort HotSide1;
}
Element Wall2 Owall6 {
    ThermalInputPort CoolSide1;
    ThermalInputPort HotSide1;
}

```

```

}
//=====================================================

Element CoolingVolume OCV3 {
    UnReactedFluidInputPort FI_I;
    UnReactedFluidOutputPort FI_O1, FI_O2;
    volume = 10;
    Aphys = 26.42;
}
//=====================================================
// OT bypass
//=====================================================
Element Valve04 TB1 {
    Across = 2;
    K = 194.5;
}

Element CoolingVolume TBCV1 {
    UnReactedFluidInputPort FI_I;
    UnReactedFluidOutputPort FI_O;
    volume = 10;
    Aphys = 2;
}

Element Valve04 TB2 {
    Across = 2;
    K = 194.5;
}
//=====================================================
Element Turb02 OT {
    Wflow = 95;
    FI_O.Aphys = 14.85;
    eff = .949;
    PR = 1.8;
}

Element CoolingVolume OCV4 {
    UnReactedFluidInputPort FI_I1 {OFR = 1;};
    UnReactedFluidInputPort FI_I2 {OFR = 1;};
    UnReactedFluidOutputPort FI_O {OFR = 1;};
    volume = 10;
    Aphys = 14.85;
}

Element Valve04 OV {
    Across = 2;
    K = 0.5255;
}

Element Shaft OSHAFT {
    ShaftInputPort Sh_I1, Sh_I2;
    Nmech = 32000;
}
//=====================================================

```

```

// Hpump
//=====
setDefaultComposition("HYDROGEN");
Element Starter TankH {}

Element Valve04 HD1 {
    Across = 2;
    K = 0.0336;
}

Element CoolingVolume HCV1 {
    UnReactedFluidInputPort FI_I;
    UnReactedFluidOutputPort FI_O;
    volume = 10;
    Aphys = 2;
}

Element Pump HP1 {
    gearRatio = 1;
    W = mdotH;
    eff = .8;
    PRdes = 45;
}

Element CoolingVolume HCV2 {
    UnReactedFluidInputPort FI_I;
    UnReactedFluidOutputPort FI_O1, FI_O2;
    volume = 10;
    Aphys = 2;
}
//=====
// Bypass
//=====
Element Valve04 BD1 {
    Across = 2;
    K = 4;
}

Element CoolingVolume BCV1 {
    UnReactedFluidInputPort FI_I;
    UnReactedFluidOutputPort FI_O;
    volume = 10;
    Aphys = 2;
}

Element Valve04 BD2 {
    Across = 2;
    K = 4;
}
//=====
Element Pump HP2 {
    gearRatio = 1;
    W = mdotH/2;
    eff = .83;
}

```

```

    PRdes = 2;
}

Element CoolingVolume HCV3 {
    UnReactedFluidInputPort FI_I;
    UnReactedFluidOutputPort FI_O;
    volume = 10;
    Aphys = 2;
}

//=====
// Cooling Jacket2
//=====

Element Valve04 DuckH1 {
    Across = 0.19;
    K = 0.0633;
}

Element CoolingVolume CVH1 {
    UnReactedFluidInputPort FI_I {};
    UnReactedFluidOutputPort FI_O {};
    ThermalOutputPort Hx_zone1 {
        areaHx = 32.97;
    };
    volume = .66;
    n_channels = 314;
    Aphys = 0.19;
}

Element Valve04 DuckH2 {
    Across = .CVH1.Aphys;
    K = 0.0474;
}

Element CoolingVolume CVH2 {
    UnReactedFluidInputPort FI_I {};
    UnReactedFluidOutputPort FI_O {};
    ThermalOutputPort Hx_zone1 {
        areaHx = 65.94;
    };
    volume = 1.32;
    n_channels = 314;
    Aphys = 0.38;
}

Element Valve04 DuckH3 {
    Across = .CVH2.Aphys;
    K = 0.114;
}

Element CoolingVolume CVH3 {
    UnReactedFluidInputPort FI_I {};
    UnReactedFluidOutputPort FI_O {};
    ThermalOutputPort Hx_zone1 {

```



```

        areaHx = 2.2;
    };
    volume = 0.04;
    n_channels = 314;
    Aphys = 0.44;
}

Element Valve04 DuckH4 {
    Across = .CVH3.Aphys;
    K = 0.149;
}

Element CoolingVolume CVH4 {
    UnReactedFluidInputPort FI_I {};
    UnReactedFluidOutputPort FI_O {};
    ThermalOutputPort Hx_zone1 {
        areaHx = 90.43;
    };
    volume = 1.81;
    n_channels = 314;
    Aphys = 0.38;
}

Element Valve04 DuckH5 {
    Across = .CVH4.Aphys;
    K = 0.0773;
}

Element CoolingVolume CVH5 {
    UnReactedFluidInputPort FI_I {};
    UnReactedFluidOutputPort FI_O {};
    ThermalOutputPort Hx_zone1 {
        areaHx = 52.74;
    };
    volume = 1.58;
    n_channels = 314;
    Aphys = 0.33;
}

Element Valve04 DuckH6 {
    Across = .CVH5.Aphys;
    K = 0.0511;
}

Element CoolingVolume CVH6 {
    UnReactedFluidInputPort FI_I {};
    UnReactedFluidOutputPort FI_O {};
    ThermalOutputPort Hx_zone1 {
        areaHx = 37.68;
    };
    volume = 1.51;
    n_channels = 314;
    Aphys = 0.31;
}

```

```

Element Valve04 DuckH7 {
  Across = .CVH6.Aphys;
  K = 0.041;
}

Element CoolingVolume CVH7 {
  UnReactedFluidInputPort FI_I {};
  UnReactedFluidOutputPort FI_O {};
  ThermalOutputPort Hx_zone1 {
    areaHx = 30.14;
  };
  volume = 1.51;
  n_channels = 314;
  Aphys = 0.31;
}

Element Valve04 DuckH8 {
  Across = .CVH7.Aphys;
  K = 0.0379;
}

Element CoolingVolume CVH8 {
  UnReactedFluidInputPort FI_I {};
  UnReactedFluidOutputPort FI_O {};
  ThermalOutputPort Hx_zone1 {
    areaHx = .CVH7.Hx_zone1.areaHx;
  };
  volume = .CVH7.volume;
  n_channels = 314;
  Aphys = .CVH7.Aphys;
}

Element Valve04 DuckH9 {
  Across = .CVH8.Aphys;
  K = 0.0351;
}

Element Wall2 Hwall1 {
  ThermalInputPort CoolSide1;
  ThermalInputPort HotSide1;
}
Element Wall2 Hwall2 {
  ThermalInputPort CoolSide1;
  ThermalInputPort HotSide1;
}
Element Wall2 Hwall3 {
  ThermalInputPort CoolSide1;
  ThermalInputPort HotSide1;
}
Element Wall2 Hwall4 {
  ThermalInputPort CoolSide1;
  ThermalInputPort HotSide1;
}

```

```

Element Wall2 Hwall5 {
    ThermalInputPort CoolSide1;
    ThermalInputPort HotSide1;
}
Element Wall2 Hwall6 {
    ThermalInputPort CoolSide1;
    ThermalInputPort HotSide1;
}
Element Wall2 Hwall7 {
    ThermalInputPort CoolSide1;
    ThermalInputPort HotSide1;
}
Element Wall2 Hwall8 {
    ThermalInputPort CoolSide1;
    ThermalInputPort HotSide1;
}
//=====================================================
Element CoolingVolume HCV4 {
    UnReactedFluidInputPort FI_I;
    UnReactedFluidOutputPort FI_O;
    volume = 10;
    Aphys = 2;
}

Element Turb02 HT {
    Wflow = mdotH/2;
    FI_O.Aphys = 2;
    eff = .9;
    PR = 1.85;
}

Element CoolingVolume HCV5 {
    UnReactedFluidInputPort FI_I1, FI_I2;
    UnReactedFluidOutputPort FI_O;
    volume = 10;
    Aphys = 2;
}

Element Valve04 HV {
    Across = 2;
    K = 2;
}

Element Shaft HSHAFT {
    ShaftInputPort Sh_I1, Sh_I2, Sh_I3;
    Nmech = 110000;
}
//=====================================================
//links
//=====================================================
linkPorts("COMB.FI_tc", "NOZZ.FI_I", "C1");

linkPorts("TankO.FI_O", "OD1.FI_I", "O1");
linkPorts("OD1.FI_O", "OCV1.FI_I", "O2");

```

```
linkPorts("OCV1.FI_O", "OP.FI_I", "O3");
linkPorts("OP.FI_O", "OCV2.FI_I", "O4");
```

```
linkPorts("OCV2.FI_O", "DuckO1.FI_I", "O5");
linkPorts("DuckO1.FI_O", "CVO1.FI_I", "O6");
linkPorts("CVO1.FI_O", "DuckO2.FI_I", "O7");
linkPorts("DuckO2.FI_O", "CVO2.FI_I", "O8");
linkPorts("CVO2.FI_O", "DuckO3.FI_I", "O9");
linkPorts("DuckO3.FI_O", "CVO3.FI_I", "O10");
linkPorts("CVO3.FI_O", "DuckO4.FI_I", "O11");
linkPorts("DuckO4.FI_O", "CVO4.FI_I", "O12");
linkPorts("CVO4.FI_O", "DuckO5.FI_I", "O13");
linkPorts("DuckO5.FI_O", "CVO5.FI_I", "O14");
linkPorts("CVO5.FI_O", "DuckO6.FI_I", "O15");
linkPorts("DuckO6.FI_O", "CVO6.FI_I", "O16");
linkPorts("CVO6.FI_O", "DuckO7.FI_I", "O17");
linkPorts("DuckO7.FI_O", "OCV3.FI_I", "O18");
```

```
linkPorts("OCV3.FI_O2", "TB1.FI_I", "T1");
linkPorts("TB1.FI_O", "TBCV1.FI_I", "T2");
linkPorts("TBCV1.FI_O", "TB2.FI_I", "T3");
linkPorts("TB2.FI_O", "OCV4.FI_I2", "T4");
```

```
linkPorts("OCV3.FI_O1", "OT.FI_I", "O19");
linkPorts("OT.FI_O", "OCV4.FI_I1", "O20");
linkPorts("OCV4.FI_O", "OV.FI_I", "O21");
linkPorts("OV.FI_O", "COMB.FI_oxid", "O22");
```

```
linkPorts("OP.Sh_O", "OSHAFT.Sh_I1", "SO1");
linkPorts("OT.Sh_O", "OSHAFT.Sh_I2", "SO2");
```

```
linkPorts("CVO1.Hx_zone1", "Owall1.CoolSide1", "W1");
linkPorts("COMB.Hx_zoneO6", "Owall1.HotSide1", "W2");
linkPorts("CVO2.Hx_zone1", "Owall2.CoolSide1", "W3");
linkPorts("COMB.Hx_zoneO5", "Owall2.HotSide1", "W4");
linkPorts("CVO3.Hx_zone1", "Owall3.CoolSide1", "W5");
linkPorts("COMB.Hx_zoneO4", "Owall3.HotSide1", "W6");
linkPorts("CVO4.Hx_zone1", "Owall4.CoolSide1", "W7");
linkPorts("COMB.Hx_zoneO3", "Owall4.HotSide1", "W8");
linkPorts("CVO5.Hx_zone1", "Owall5.CoolSide1", "W9");
linkPorts("COMB.Hx_zoneO2", "Owall5.HotSide1", "W10");
linkPorts("CVO6.Hx_zone1", "Owall6.CoolSide1", "W11");
linkPorts("COMB.Hx_zoneO1", "Owall6.HotSide1", "W12");
```

```
linkPorts("TankH.FI_O", "HD1.FI_I", "F1");
linkPorts("HD1.FI_O", "HCV1.FI_I", "F2");
linkPorts("HCV1.FI_O", "HP1.FI_I", "F3");
linkPorts("HP1.FI_O", "HCV2.FI_I", "F4");
linkPorts("HCV2.FI_O1", "HP2.FI_I", "F5");
```

```
linkPorts("HCV2.FI_O2", "BD1.FI_I", "B1");
linkPorts("BD1.FI_O", "BCV1.FI_I", "B2");
linkPorts("BCV1.FI_O", "BD2.FI_I", "B3");
linkPorts("BD2.FI_O", "HCV5.FI_I2", "B4");
```

```

linkPorts("HP2.Fl_O", "HCV3.Fl_I", "F6");
linkPorts("HCV3.Fl_O", "DuckH1.Fl_I", "F8");

linkPorts( "DuckH1.Fl_O", "CVH1.Fl_I", "H2" );
linkPorts( "CVH1.Fl_O", "DuckH2.Fl_I", "H3" );
linkPorts( "DuckH2.Fl_O", "CVH2.Fl_I", "H4" );
linkPorts( "CVH2.Fl_O", "DuckH3.Fl_I", "H5" );
linkPorts( "DuckH3.Fl_O", "CVH3.Fl_I", "H6" );
linkPorts( "CVH3.Fl_O", "DuckH4.Fl_I", "H7" );
linkPorts( "DuckH4.Fl_O", "CVH4.Fl_I", "H8" );
linkPorts( "CVH4.Fl_O", "DuckH5.Fl_I", "H9" );
linkPorts( "DuckH5.Fl_O", "CVH5.Fl_I", "H10" );
linkPorts( "CVH5.Fl_O", "DuckH6.Fl_I", "H11" );
linkPorts( "DuckH6.Fl_O", "CVH6.Fl_I", "H12" );
linkPorts( "CVH6.Fl_O", "DuckH7.Fl_I", "H13" );
linkPorts( "DuckH7.Fl_O", "CVH7.Fl_I", "H14" );
linkPorts( "CVH7.Fl_O", "DuckH8.Fl_I", "H15" );
linkPorts( "DuckH8.Fl_O", "CVH8.Fl_I", "H16" );
linkPorts( "CVH8.Fl_O", "DuckH9.Fl_I", "H17" );
linkPorts( "DuckH9.Fl_O", "HCV4.Fl_I", "H18" );

linkPorts("HCV4.Fl_O", "HT.Fl_I", "F12");
linkPorts("HT.Fl_O", "HCV5.Fl_I", "F13");
linkPorts("HCV5.Fl_O", "HV.Fl_I", "F15");
linkPorts("HV.Fl_O", "COMB.Fu_I", "F16");

linkPorts("HP1.Sh_O", "HSHAFT.Sh_I1", "SH1");
linkPorts("HT.Sh_O", "HSHAFT.Sh_I2", "SH2");
linkPorts("HP2.Sh_O", "HSHAFT.Sh_I3", "SH3");

linkPorts("CVH1.Hx_zone1", "Hwall1.CoolSide1", "W13");
linkPorts("NOZZ.Hx_zoneH8", "Hwall1.HotSide1", "W14");
linkPorts("CVH2.Hx_zone1", "Hwall2.CoolSide1", "W15");
linkPorts("NOZZ.Hx_zoneH7", "Hwall2.HotSide1", "W16");
linkPorts("CVH3.Hx_zone1", "Hwall3.CoolSide1", "W17");
linkPorts("COMB.Hx_zoneH6", "Hwall3.HotSide1", "W18");
linkPorts("CVH4.Hx_zone1", "Hwall4.CoolSide1", "W19");
linkPorts("COMB.Hx_zoneH5", "Hwall4.HotSide1", "W20");
linkPorts("CVH5.Hx_zone1", "Hwall5.CoolSide1", "W21");
linkPorts("COMB.Hx_zoneH4", "Hwall5.HotSide1", "W22");
linkPorts("CVH6.Hx_zone1", "Hwall6.CoolSide1", "W23");
linkPorts("COMB.Hx_zoneH3", "Hwall6.HotSide1", "W24");
linkPorts("CVH7.Hx_zone1", "Hwall7.CoolSide1", "W25");
linkPorts("COMB.Hx_zoneH2", "Hwall7.HotSide1", "W26");
linkPorts("CVH8.Hx_zone1", "Hwall8.CoolSide1", "W27");
linkPorts("COMB.Hx_zoneH1", "Hwall8.HotSide1", "W28");
//=====
//Guesses
//=====
COMB.OFR = O_F / (1 + O_F);
COMB.Tt_tc = 6550;
COMB.Pt_tc = P_c;
COMB.Fl_tc.W = mdot;

```

TankO.Pt = 46;
TankO.Tt = 150;

OD1.W = mdotO;
OV.W = mdotO;
DuckO1.W = mdotO;
DuckO2.W = mdotO;
DuckO3.W = mdotO;
DuckO4.W = mdotO;
DuckO5.W = mdotO;
DuckO6.W = mdotO;
DuckO7.W = mdotO;
TB1.W = mdotO-95;
TB2.W = mdotO-95;

OCV1.Pt = 45;
OCV1.ht = 66;
OCV2.Pt = 4635;
OCV2.ht = 66;
CVO1.Pt = 4497;
CVO1.ht = 66;
CVO2.Pt = 4359;
CVO2.ht = 66;
CVO3.Pt = 4221;
CVO3.ht = 66;
CVO4.Pt = 4083;
CVO4.ht = 66;
CVO5.Pt = 3945;
CVO5.ht = 66;
CVO6.Pt = 3807;
CVO6.ht = 66;
OCV3.Pt = 3663;
OCV3.ht = 66;
TBCV1.Pt = 2849;
TBCV1.ht = 66;
OCV4.Pt = 2035;
OCV4.ht = 66;

Owall1.T = Wall_temp;
Owall2.T = Wall_temp;
Owall3.T = Wall_temp;
Owall4.T = Wall_temp;
Owall5.T = Wall_temp;
Owall6.T = Wall_temp;

TankH.Pt = 46;
TankH.Tt = 40;

HD1.W = mdotH;
HV.W = mdotH;
BD1.W = mdotH/2;
BD2.W = mdotH/2;
DuckH1.W = mdotH/2;

```

DuckH2.W = mdotH/2;
DuckH3.W = mdotH/2;
DuckH4.W = mdotH/2;
DuckH5.W = mdotH/2;
DuckH6.W = mdotH/2;
DuckH7.W = mdotH/2;
DuckH8.W = mdotH/2;
DuckH9.W = mdotH/2;

```

```

HCV1.Pt = 45;
HCV1.ht = 66;
HCV2.Pt = 2035;
HCV2.ht = 66;
BCV1.Pt = 2008;
BCV1.ht = 66;
HCV3.Pt = 4080;
HCV3.ht = 66;
CVH1.Pt = 4034;
CVH1.ht = 66;
CVH2.Pt = 3988;
CVH2.ht = 66;
CVH3.Pt = 3942;
CVH3.ht = 66;
CVH4.Pt = 3896;
CVH4.ht = 66;
CVH5.Pt = 3850;
CVH5.ht = 66;
CVH6.Pt = 3804;
CVH6.ht = 66;
CVH7.Pt = 3758;
CVH7.ht = 66;
CVH8.Pt = 3712;
CVH8.ht = 66;
HCV4.Pt = 3663;
HCV4.ht = 66;
HCV5.Pt = 1980;
HCV5.ht = 66;

```

```

Hwall1.T = Wall_temp;
Hwall2.T = Wall_temp;
Hwall3.T = Wall_temp;
Hwall4.T = Wall_temp;
Hwall5.T = Wall_temp;
Hwall6.T = Wall_temp;
Hwall7.T = Wall_temp;
Hwall8.T = Wall_temp;

```

```

//Solver will adjust these variables
Independent H_valve {
    varName = "HP1.eff";
    autoSetup = TRUE;
}

```

```

Independent O_valve {

```

```

varName = "OP.eff";
autoSetup = TRUE;
}
//=====================================================
// Solver
//=====================================================
solver.solutionMode = "STEADY_STATE";
presolverSequence = {};
solverSequence = {"NOZZ", "TankO", "OD1", "OP", "DuckO1",
"DuckO2", "DuckO3", "DuckO4", "DuckO5", "DuckO6", "DuckO7", "TB1", "TB2", "OT", "OV",
"TankH", "HD1", "HP1", "BD1", "BD2", "HP2", "DuckH1", "DuckH2", "DuckH3",
"DuckH4", "DuckH5", "DuckH6", "DuckH7", "DuckH8", "DuckH9", "HT", "HV",
"COMB", "OCV1", "OCV2", "CVO1", "CVO2", "CVO3", "CVO4", "CVO5", "CVO6", "OCV3",
"TBVCV1",
"OCV4", "OSHAFT", "Owall1", "Owall2", "Owall3", "Owall4", "Owall5", "Owall6",
"HCV1", "HCV2", "BCV1", "HCV3", "CVH1", "CVH2", "CVH3", "CVH4", "CVH5",
"CVH6", "CVH7", "CVH8", "HCV4", "HCV5", "HSHAFT", "Hwall1", "Hwall2", "Hwall3",
"Hwall4", "Hwall5", "Hwall6", "Hwall7", "Hwall8"}

DataViewer CaseRowViewer Chamber {
    titleBody = "";
    titleVars = {}
    variableList = {"COMB.Pt_tc", "COMB.Tt_tc", "COMB.OF", "NOZZ.Fg",
"NOZZ.lsp", "NOZZ.W" };
}

DataViewer CaseRowViewer CoolO {
    titleBody = "";
    titleVars = {}
    variableList = {"CVO1.FI_I.Tt", "CVO1.FI_O.Tt", "CVO2.FI_O.Tt",
"CVO3.FI_O.Tt", "CVO4.FI_O.Tt", "CVO5.FI_O.Tt", "CVO6.FI_O.Tt"};
}

DataViewer CaseRowViewer CoolH {
    titleBody = "";
    titleVars = {}
    variableList = {"CVH1.FI_I.Tt", "CVH1.FI_O.Tt", "CVH2.FI_O.Tt",
"CVH3.FI_O.Tt", "CVH4.FI_O.Tt", "CVH5.FI_O.Tt", "CVH6.FI_O.Tt", "CVH7.FI_O.Tt",
"CVH8.FI_O.Tt"};
}

postsolverSequence = {"Chamber", "CoolO", "CoolH"};
autoSolverSetup();

solver.maxIterations = 5000;
solver.maxJacobians = 5000;

run();
Chamber.display();
CoolO.display();
CoolH.display();
cout << "Oxygen =====<<endl;
cout << "mass Flow " << CVO1.Wavg << " lbm/sec" << endl;
cout << "max temp " << Owall1.T << " R, " << Owall6.T << " R"<< endl;

```



```

cout << "velocity6 " << CVO6.Fl_O.V << " ft/s" << endl;
cout << "velocity5 " << CVO5.Fl_O.V << " ft/s" << endl;
cout << "velocity4 " << CVO4.Fl_O.V << " ft/s" << endl;
cout << "Sum Q " << Owall1.Qout+Owall2.Qout+Owall3.Qout+Owall4.Qout+Owall5.Qout
+Owall6.Qout << " Btu/sec" << endl;
cout << "Total SA " << CVO1.Hx_zone1.areaHx+CVO2.Hx_zone1.areaHx+
CVO3.Hx_zone1.areaHx+CVO4.Hx_zone1.areaHx+CVO5.Hx_zone1.areaHx+
CVO6.Hx_zone1.areaHx << " in^2" << endl << endl;
cout << "OP massFlow " << OP.W << " lbm/s, OP PR " << OP.PR << endl;
cout << "ONmech " << OSHAFT.Nmech << " rpm" << endl;
cout << "OT massFlow " << OT.Wflow << " lbm/s, " << " OT PR " << OT.PR << endl;
cout << "OT power " << OT.pwr << " hp, OP power " << OP.pwr << " hp" << endl;
cout << "Hydrogen =====<< endl;
cout << "mass Flow " << CVH1.Wavg << " lbm/sec" << endl;
cout << "max temp " << Hwall3.T << " R" << endl;
cout << "velocity8 " << CVH8.Fl_O.V << " ft/s" << endl;
cout << "velocity7 " << CVH7.Fl_O.V << " ft/s" << endl;
cout << "velocity6 " << CVH6.Fl_O.V << " ft/s" << endl;
cout << "Sum Q " << Hwall1.Qout+Hwall2.Qout+Hwall3.Qout+Hwall4.Qout+Hwall5.Qout
+Hwall6.Qout+Hwall7.Qout+Hwall8.Qout << " Btu/sec" << endl;
cout << "Total SA " << CVH1.Hx_zone1.areaHx+CVH2.Hx_zone1.areaHx+
CVH3.Hx_zone1.areaHx+CVH4.Hx_zone1.areaHx+CVH5.Hx_zone1.areaHx+
CVH6.Hx_zone1.areaHx+CVH7.Hx_zone1.areaHx+CVH8.Hx_zone1.areaHx <<
" in^2" << endl << endl;
cout << "HP1 massFlow " << HP1.W << " lbm/s, HP1 PR " << HP1.PR << endl;
cout << "HP2 massFlow " << HP2.W << " lbm/s, HP2 PR " << HP2.PR << endl;
cout << "HNmech " << HSHAFT.Nmech << " rpm" << endl;
cout << "HT massFlow " << HT.Wflow << " lbm/s " << " HT PR " << HT.PR << endl;
cout << "HT pwr " << HT.pwr << " hp, HP1 pwr " << HP1.pwr << " hp, HP2 pwr " <<
HP2.pwr << " hp" << endl;

```

B.2 Included Cooling Volume Element

```

#ifndef __COOLINGVOLUME__
#define __COOLINGVOLUME__

//*****
// * NASA Glenn Research Center
// * 21000 Brookpark Rd
// * Cleveland, OH 44135
// *
// *****

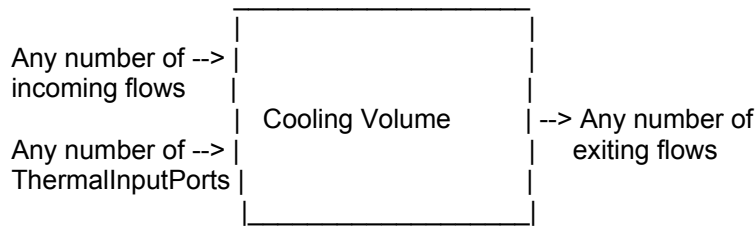
//#include "/NPSS/dev/Rockets/Common/RocketIncludes.npss"
#include <InterpIncludes.ncp>

class CoolingVolume extends Element{

//-----
// ***** DOCUMENTATION *****
//-----
/*
title =
"

```

COOLING VOLUME ELEMENT



```

",
",
*/

```

description = isA() + " performs mass and energy storage calculations. Also allows for heat transfer.";

```

usageNotes =
"

```

- The cooling volume element accounts for mass and energy storage at a volume location in space.
- Any number of FluidInput, FluidOutput, and Thermal ports can be requested by the user at run time. These ports are then connected to the model using the usual linkPorts command.
- The user may also specify an external heat transfer that is applied to the element. Note that this energy will come from outside the simulation and will break continuity of energy for the overall system.
- The purpose of this element is to calculate mass and energy derivatives that are used by the solver to balance the conditions and this location in space.
- The element has two default solver independents and two default solver states.
- In steady-state mode the solver will vary enthalpy and pressure until the mass and energy derivatives are zero (mass in = mass out, energy in = energy out).
- In transient mode, the pressure and enthalpy will be varied until the calculated internal energy and density equal the integrated energy and density.
- To nullify the transient effects of this element in an otherwise transient solution, set the solution mode of the element to steady state. Ex: elementName.solutionMode = 'STEADY-STATE'. Note that this element does

have solutionMode as a variable. However, giving the above command will set all of the pertinent solver objects to 'STEADY-STATE'.

```

",
;

//-----
// ***** SETUP VARIABLES *****
//-----
real Aphys{
  IOstatus = INPUT; units = INCH2;
  description = "Representative cross sectional area (used to calculate statics)";
  trigger = 1;
}
string comp{
  description = "Composition of the volume";
  trigger = 1;
}
real drhotqdt{
  value = 0.0; IOstatus = OUTPUT; units = LBM_PER_FT3_SEC;
  description = "Time derivative of total density";
}
real dutqdt{
  value = 0.0; IOstatus = OUTPUT; units = BTU_PER_LBM_SEC;
  description = "Time derivative of total specific internal energy";
}
int _Hset {
  value = FALSE; IOstatus = INPUT; units = NONE;
  description = "Used internally to determine if enthalpy has been set (User Should Not Touch)";
  hide(1);
}
real ht{
  IOstatus = OUTPUT; units = BTU_PER_LBM;
  description = "Total specific enthalpy";
  trigger = 1;
}
real HtIn{
  value = 0.0; IOstatus = OUTPUT; units = BTU_PER_SEC;
  description = "Total energy flowing in to the volume through the ports";
}
real HtOut{
  value = 0.0; IOstatus = OUTPUT; units = BTU_PER_SEC;
  description = "Total energy flowing out of the volume through the ports";
}
string inportList[];
inportList {
  description = "list of all fluid input ports";
  ptrType = "UnReactedFluidInputPort";
}
int n_channels {
  value = 0.0; IOstatus = INPUT; units = NONE;
  description = "Number of channels in the cooling volume";
}
string outportList[];
outportList {

```

```

description = "list of all fluid output ports";
ptrType = "UnReactedFluidOutputPort";
}
int _Pset {
value = FALSE; IOstatus = INPUT; units = NONE;
description = "Used internally to determine if pressure has been set (User Should Not Touch)";
hide(1);
}
real Pt{
IOstatus = OUTPUT; units = PSIA;
description = "Total pressure";
trigger = 1;
}
real Qnet{
value = 0.0; IOstatus = OUTPUT; units = BTU_PER_SEC;
description = "Net heat tranfers out of the volume through thermal ports";
}
real Qext{
value = 0.0; IOstatus = INPUT; units = BTU_PER_SEC;
description = "External heat transfer supplied by user (note that this value breaks conservation
of energy";
}
real s_Qnet {
value = 1.0; IOstatus = INPUT; units = NONE;
description = "Heat transfer scale factor (on Q_net only)";
}
real rhot{
value = 0.0; IOstatus = INPUT; units = LBM_PER_FT3;
description = "Density based on total conditions";
}
real ut{
value = 0.0; IOstatus = INPUT; units = BTU_PER_LBM;
description = "Total specific internal energy";
}
real volume{
value = 0.0; IOstatus = INPUT; units = INCH3;
description = "Volume";
}
real Wavg{
value = 0.0; IOstatus = OUTPUT; units = LBM_PER_SEC;
description = "Average mass flowing through each port";
}
real Win{
value = 0.0; IOstatus = OUTPUT; units = LBM_PER_SEC;
description = "Total mass flowing into the volume";
}
real Wout{
value = 0.0; IOstatus = OUTPUT; units = LBM_PER_SEC;
description = "Total mass flowing out of the volume";
}

//-----
// ***** SETUP PORTS, FLOW STATIONS, SOCKETS, TABLES *****
//-----

```

```

// FLUID PORTS

UnReactedFlowStation FI_vol{
    description = "Internal station used to calculate volume properties";
}

// FUEL PORTS

// BLEED PORTS

// THERMAL PORTS
string HxPorts[];
HxPorts {
    description = "Array of Thermal ports";
    ptrType = "ThermalOutputPort";
}

// FLOW STATIONS

// SOCKETS

//-----
// ***** INTERNAL SOLVER SETUP *****
//-----

//-----
// ***** ADD SOLVER INDEPENDENTS & DEPENDENT *****
//-----
Independent ind_Pt {
    varName = "Pt";
    autoSetup = TRUE;
    description = "Varies the volume total pressure";
}

Independent ind_ht {
    varName = "ht";
    autoSetup = TRUE;
    description = "Varies the volume total specific enthalpy";
    indepRef = "100.";
}

Integrator integ_rho {
    stateName = "rhot";
    derivativeName = "drhotqdt";
    eq_rhs = "Win";
    eq_lhs = "Wout";
    autoSetup = TRUE;
    description = "Balances the volume mass storage";
}

Integrator integ_U {
    stateName = "ut";
    derivativeName = "dutqdt";
}

```

```

eq_rhs = "HtIn + Qnet + Qext";
eq_lhs = "HtOut";
autoSetup = TRUE;
//eq_Ref = "100.";
description = "Balances the volume energy storage";
}

//-----
// ***** VARIABLE CHANGED METHODOLOGY *****
//-----

//-----
// ***** OPTION VARIABLE SETUP *****
//-----

//-----
// ***** PERFORM ENGINEERING CALCULATIONS *****
//-----

//-----
// calculate function
//-----
void calculate() {
    int i;

    //-----
    // set the working area
    //-----
    FI_vol.Aphys = Aphys;

    //-----
    // Heat Transfer Calculations
    //-----

    //-----
    // Determine the average flow rate
    //-----
    Wavg = 0.0;
    int iport;
    for ( iport = 0; iport < inportList.entries(); iport = iport + 1 ) {
        Wavg = Wavg + inportList[iport]->W;
    }
    for ( iport = 0; iport < outportList.entries(); iport = iport + 1 ) {
        Wavg = Wavg + outportList[iport]->W;
    }
    Wavg = Wavg / 2.;

    real Wc = Wavg;
    real Ac = Aphys;

    //-----
    // Compute the hydraulic diameter
    //-----

```

```

real D_hyd = 2. *( Ac / PI / n_channels )**0.5;
Qnet = 0;

//-----
// Loop through the thermal ports calculating the heat flux
//-----
for ( iport = 0; iport < HxPorts.entries(); iport = iport + 1 ) {

    //-----
    // determine the heat transfer coefficient for the heat
    // flow through Hx_zone1
    //-----
    real hc = s_Qnet * 0.023 *( abs( Wc )/ Ac )**0.8
        * FI_vol.kt**0.6 *( FI_vol.Cpt / FI_vol.mut )**0.4
        / D_hyd**0.2;

    //-----
    // Compute the heat transfer rates
    // Note that the area here is total for all coolant channels
    //-----
    real Q = hc * HxPorts[iport]->areaHx * ( HxPorts[iport]->MassTemp - FI_vol.Tt );

    //-----
    // Set the coefficients and rates in the corresponding thermal
    // ports connected to the hot-wall and the outer wall
    //-----
    HxPorts[iport]->HeatTransferCoef = hc;
    HxPorts[iport]->HeatTransferRate = Q;

    //-----
    // add the heat transfer rates to the volume overall Qhxdt
    //-----
    Qnet = Qnet + Q;

}

//-----
// Create some working variables and initialize values for
// summations
//-----
real Wt;
Win = 0.0;
Wout = 0.0;
HtIn = 0.0;
HtOut = 0.0;

//-----
// Grab the total density and internal energy from the working
// station
// These values are calculated by the station when Pt and ht are
// set
//-----
rhot = FI_vol.rhot;
ut = FI_vol.ut;

```

```

//-----
// Sum up energy and flow over the incoming ports
//-----
// int i;
for ( i=0; i < inportList.entries() ; i = i + 1 ) {
    Wt = inportList[i]->W;
    if ( Wt >= 0.0 ) {
        Win = Win + Wt;
        HtIn = HtIn + Wt * inportList[i]->ht;
    }
    else {
        Wout = Wout - Wt;
        HtOut = HtOut - Wt * ht;
    }
}

//-----
// Sum up energy and flow over the exiting ports
//-----
for ( i=0; i < outportList.entries(); i = i + 1 ) {
    Wt = outportList[i]->W;
    if ( Wt >= 0.0 ) {
        Wout = Wout + Wt;
        HtOut = HtOut + Wt * ht;
    }
    else {
        Win = Win - Wt;
        HtIn = HtIn - Wt * outportList[i]->ht;
    }
}

//-----
// calculate the state-derivatives
//-----
drhotqdt = ( Win - Wout )/ volume*12*12*12;
dutqdt = ( HtIn + Qnet + Qext - HtOut - ut * ( Win - Wout ) ) / ( rhot * volume/12/12/12 );
}

//-----
// VERIFY function (same as for basic Volume class)
//-----
int verify()
{
    //-----
    // set the composition in all the stations
    //-----
    int i;
    for ( i = 0; i < inportList.entries(); i = i + 1 ) {
        inportList[i]->comp = FI_vol.comp;
    }
    for ( i = 0; i < outportList.entries(); i = i + 1 ) {

```



```

        outportList[i]->comp = FI_vol.comp;
    }

    //-----
    // check to be sure the volume has a reasonable value
    //-----
    if (volume <= 0.0000 ) {
        cerr << "verify failed because volume has not been set" << endl;
        return FALSE;
    }

    return TRUE;
}

//-----
// variable changed function
//-----
void variableChanged( string name, any oldValue ){
    int i;

    //-----
    // Put the enthalpy and pressure, which are probably set in the
    // solver to all the stations and ports
    //-----
    if ( name == "comp" ) {

        FI_vol.comp = comp;

        //int i;
        for ( i = 0; i < inportList.entries(); i = i + 1 ) {
            inportList[i]->comp = comp;
        }
        for ( i = 0; i < outportList.entries(); i = i + 1 ) {
            outportList[i]->comp = comp;
        }
    }
}

//-----
// ***** PREPASS FUNCTION *****
//-----
void prePass() {

    // Set the conditions in the volume and all the ports. The
    // static conditions in the ports will depend on their flow
    // and area.
    int i;

    FI_vol.setTotal_hP(ht, Pt);

    for (i=0; i<inportList.entries(); i = i + 1) {
        inportList[i]->setTotal_hP(ht, Pt); }
}

```

```

for (i=0; i<outportList.entries(); i = i + 1) {
    outportList[i]->setTotal_hP(ht, Pt); }
}

// -----
// ***** POSTCREATE FUNCTION *****
// -----
void postcreate( string name ) {
    //-----
    // allow for the creation of ports at run time
    //-----
    if ( name->hasInterface( "ThermalOutputPort" )) {
        HxPorts.append(name);
    }
    if ( name->hasInterface( "UnReactedFluidInputPort" )) {
        inportList.append(name);
    }
    if ( name->hasInterface( "UnReactedFluidOutputPort" )) {
        outportList.append( name );
    }
}

}

//dumpMaps("maps.out");

#endif

```

B.3 Included Pump Element

```

#ifndef __PUMP__
#define __PUMP__

//*****
// * NASA Glenn Research Center
// * 21000 Brookpark Rd
// * Cleveland, OH 44135
// *
// *****

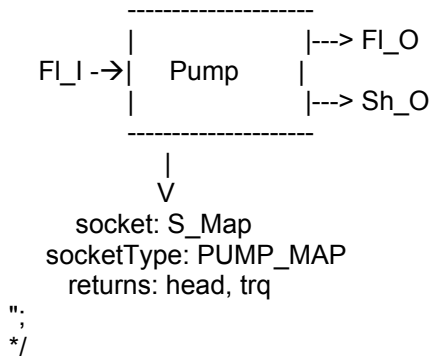
//#include "NPSS/dev/Rockets/Common/RocketIncludes.npss"
#include <InterpIncludes.ncp>

class Pump extends Element{

//-----
// ***** DOCUMENTATION *****
//-----

/*
    title =
    "      PUMP ELEMENT

```



description = isA() + " calculates the performance of a rocket pump element.";

usageNotes =
"

- This element works by determining the exit conditions based on either user supplied or subelement calculated values of torque and head.
- The element takes weight flow as input and determines an exit pressure.
- There is a default solver independent and dependent available that will vary the weight flow until the calculated exit pressure matches the exit pressure seen at the port.
- The user must supply an initial guess for the weight flow.
- The inertia is kept in the mechanical port. The user should set the value directly there (Sh_O.inertia).

",
;

```

//-----
// ***** SETUP VARIABLES *****
//-----
real dht {
  value = 0.0; IOstatus = OUTPUT; units = BTU_PER_LBM;
  description = "Actual specific enthalpy change";
}
real dhtIdeal {
  value = 0.0; IOstatus = OUTPUT; units = BTU_PER_LBM;
  description = "Ideal specific enthalpy change";
}
real eff {
  value = 0.0; IOstatus = OUTPUT; units = NONE;
  description = "Compressor efficiency";
}
real gearRatio {
  value = 1.0; IOstatus = OUTPUT; units = NONE;

```

```

    description = "Gear ratio on mechanical connection";
}
real head {
    value = 0.0; IOstatus = OUTPUT; units = INCH;
    description = "Pump head diameter";
}
real Nmech {
    value = 0.0; IOstatus = OUTPUT; units = RPM;
    description = "Rotational speed (after gear ratio applied)";
}
real PR {
    value = 0.0; IOstatus = OUTPUT; units = NONE;
    description = "Pressure ratio calculated from pump characteristics";
}
real PRg{
    value = 0.0; IOstatus = OUTPUT; units = NONE;
    description = "Guess for pressure ratio calculated from fluid ports";
}
real pwr {
    value = 0.0; IOstatus = OUTPUT; units = HORSEPOWER;
    description = "Compressor power";
}
real trq {
    value = 0.0; IOstatus = OUTPUT; units = FT_LBF;
    description = "Compressor torque";
}
real W {
    value = 0.0; IOstatus = INPUT; units = LBM_PER_SEC;
    description = "Compressor weight flow";
}
real PRdes;
//-----
// ***** SETUP PORTS, FLOW STATIONS, SOCKETS, TABLES *****
//-----

// FLUID PORTS

UnReactedFluidInputPort FI_I{
    description = "Incoming flow";
};

UnReactedFluidOutputPort FI_O{
    description = "Exiting flow";
};
UnReactedFlowStation FI_Otemp{
    description = "Exiting flow";
};

// FUEL PORTS

// BLEED PORTS

// THERMAL PORTS

```

```

// MECHANICAL PORTS

ShaftOutputPort Sh_O {
    description = "Mechanical connection";
}

// FLOW STATIONS

UnReactedFlowStation FI_Oi {
    description = "Ideal exit conditions";
}

// SOCKETS

Socket S_map {
    allowedValues = { "trq", "head" }
    socketType= "PUMP_MAP";
    description = "Pump performance map";
}

//-----
// ***** ADD SOLVER INDEPENDENTS & DEPENDENT *****
//-----
Independent ind_W {
    varName = "W";
    autoSetup = TRUE;
    description = "Varies the weight flow";
}

Dependent dep_PR {
    eq_lhs = "PR";
    eq_rhs = "PRdes";
    autoSetup = TRUE;
    description = "Compares the pressure ratios calculated from the ports and the map";
}
//-----
// ***** VARIABLE CHANGED METHODOLOGY *****
//-----

//-----
// ***** OPTION VARIABLE SETUP *****
//-----
Option switchDes {
    allowedValues = { DESIGN, OFFDESIGN } //default is DESIGN
    description = "Design mode switch indicator [DESIGN / OFFDESIGN]";
    trigger = 0;
    rewritableValues = FALSE; // Enables converter optimization.
}

//-----
// ***** PERFORM ENGINEERING CALCULATIONS *****
//-----
void calculate() {

```

```

//-----
// Set the weight flows in the ports
//-----
FI_I.W = W;
FI_O.W = W;

//-----
// Determine the mechanical speed from the shaft and gear ratio
//-----
Nmech = gearRatio * Sh_O.Nmech;
PR = FI_O.Pt / FI_I.Pt;

real Sout = FI_I.s;
//real PtOut = PR * PtIn;
FI_Otemp.setTotalSP( Sout, FI_O.Pt );
real htIdealOut = FI_Otemp.ht;

//-----
// Set the exit conditions (done to get ht right)
//-----
FI_O.setTotal_hP( FI_I.ht + (htIdealOut - FI_I.ht)/eff, FI_O.Pt );

dht = ( FI_O.ht-FI_I.ht );
//-----
// Determine the power for output
//-----
pwr = -dht * W * C_BTUtoFT_LBF / C_HPtoFT_LBF_PER_SEC;

//cout << "pwr is " << pwr << endl;

trq = C_HP_PER_RPMtoFT_LBF * pwr / Nmech;

//-----
// Set values in the ports
//-----
Sh_O.trq = trq;

} //End calculate

} //End element

#endif

```

B.4 Included Turbine Element

```

#ifndef __TURB02__
#define __TURB02__

//*****
// * NASA Glenn Research Center
// * 21000 Brookpark Rd

```

```

// * Cleveland, OH 44135
// *
// *****
#include <InterpIncludes.ncp>

class Turb02 extends Element{

//-----
// ***** DOCUMENTATION *****
//-----

/*
  title =
  "      TURB02 ELEMENT

      -----
      |      |      |---> FI_O
FI_I --->| Turb02 |
      |      |      |---> Sh_O
      -----
      |
      V
      socket: S_map
      socketType: TURB02_MAP
      return: eff, W

  ",
  ;
*/

  description = isA() + " calculates the performance of a turbine that is being driven by a single
  constituent fluid";

  usageNotes =
  "
  - This element works by determining the exit conditions based on either
  user supplied or subelement calculated values of efficiency and weight
  flow.

  - The inertia is kept in the mechanical port. The user should set the value
  directly there (Sh_O.inertia).

  - There are no solver independents and dependents directly associated
  with this element.

  ",

//-----
// ***** SETUP VARIABLES *****
//-----
  real dht {
    value = 0.0; IOstatus = OUTPUT; units = BTU_PER_LBM;
    description = "Change in enthalpy";
  }

```

```

}
real dhtIdeal {
    value = 0.0; IOstatus = OUTPUT; units = BTU_PER_LBM;
    description = "Ideal enthalpy change";
}
real eff {
    value = 0.0; IOstatus = OUTPUT; units = NONE;
    description = "Efficiency";
}
real gearRatio {
    value = 1.0; IOstatus = OUTPUT; units = NONE;
    description = "Gear ratio on mechanical connection";
}
real Nmech {
    value = 0.0; IOstatus = OUTPUT; units = RPM;
    description = "Rotational speed (after gear ratio applied)";
}
real Nrad {
    value = 0.0; IOstatus = OUTPUT; units = RAD_PER_SEC;
    description = "Rotational speed in radians per sec";
}
real PR {
    value = 0.0; IOstatus = OUTPUT; units = NONE;
    description = "Pressure ratio (seen from ports)";
}
real pwr {
    value = 0.0; IOstatus = OUTPUT; units = HORSEPOWER;
    description = "Overall power";
}
real trq {
    value = 0.0; IOstatus = OUTPUT; units = FT_LBF;
    description = "Torque on the shaft";
}
real Wflow {
    value = 0.0; IOstatus = INPUT; units = LBM_PER_SEC;
    description = "Weight flow";
}

//-----
// ***** SETUP PORTS, FLOW STATIONS, SOCKETS, TABLES *****
//-----

// FLUID PORTS

UnReactedFluidInputPort FI_I{
    description = "Incoming flow";
};

UnReactedFluidOutputPort FI_O{
    description = "Exiting flow";
};

// FUEL PORTS

```



```

// BLEED PORTS

// THERMAL PORTS

// MECHANICAL PORTS

ShaftOutputPort Sh_O{
    description = "Mechanical connection";
}

// FLOW STATIONS
UnReactedFlowStation FI_Oi{
    description = "Ideal exit conditions";
}

// SOCKETS

Socket S_map {
    allowedValues = { "eff" , "Wflow" }
    description = "Turbine map";
    //socketType = TURB02_MAP;
}
Independent ind_W{
    varName = "Wflow";
    //autoSetup = TRUE;
    description = "Varies the weight flow";
}

//-----
// ***** VARIABLE CHANGED METHODOLOGY *****
//-----

//-----
// ***** OPTION VARIABLE SETUP *****
//-----
Option switchDes{
    allowedValues = { DESIGN, OFFDESIGN } //default is DESIGN
    description = "Design mode switch indicator [DESIGN / OFFDESIGN]";
    trigger = 0;
    rewritableValues = FALSE; // Enables converter optimization.
}

//-----
// ***** PERFORM ENGINEERING CALCULATIONS *****
//-----
void calculate() {

//-----
// Determine the mechanical speed from the shaft and gear ratio
//-----
Nmech = gearRatio * Sh_O.Nmech;

```

```

//-----
// Switch the mechanical speed to radians per sec
//-----
Nrad = Nmech * 2 * PI / 60;

//-----
// Determine PR
//-----
PR = FI_I.Pt / FI_O.Pt;

//-----
// determine the ideal enthalpy change
//-----
FI_Oi.copyFlow( "FI_I" );
FI_Oi.setTotalSP( FI_I.s, FI_O.Pt );
dhtIdeal = FI_I.ht - FI_Oi.ht;

//-----
// Calculate turbine torque
//-----
dht = dhtIdeal * eff;
FI_O.setTotal_hP( FI_I.ht - dht, FI_O.Pt );
trq = C_BTUtoFT_LBF * Wflow * dht / Nrad;
pwr = dht * Wflow * C_BTUtoFT_LBF / C_HPtoFT_LBF_PER_SEC;

//-----
// set the conditions in the shaft port
//-----
Sh_O.trq = trq;

//-----
// set the flows
//-----
FI_I.W = Wflow;
FI_O.W = Wflow;

} //End calculate

} //End element

#endif

```

Appendix C : TDK Code

This is TDK input and output developed for use with the DEAN NPSS model file.

C.1 TDK Input for DEAN Upper Stage Engine

```
TITLE DEAN_contour100%
DATA
$DATA
SCRJET = 1, PLANAR = F,
ODE = 1, ODK=1, TDK=1, MABL = 2, IMABL = 0, MABLK = T,
RSI = 2.084, RWTD = 0.05, RZERO = -1,
IWALL= 2, THETA = 25, RMAX = -0.01, ZMAX = 3.2,
LWALL = 1, THALW = 2.5, XLW(1) = 0, YLW(1) = -1.11, XCOWL = 0.1, ICOWL = 1,
JET = T, PINF = 0.1, MINF = 16.4, GINF = 1.4,
$END
REACTANTS
H 2.                100.   -2154.L  20.27F .0709
O 2.                100.   -3102.L  90.56O 1.149

NAMELISTS
$ODE
RKT = T, PSIA = T, XP = 1, DELH = 0,
OF = T, OFSKED = 7, PSJ = 1739, TSJ = 6586, MSJ = 3.0,
$END
REACTIONS
H + H = H2    ,M1, A = 6.4E17, N = 1.0, B = 0.0, (AR) BAULCH 72 (A) 30U
H + OH = H2O  ,M2, A = 8.4E21, N = 2.0, B = 0.0, (AR) BAULCH 72 (A) 10U
O + O = O2    ,M3, A = 1.9E13, N = 0.0, B = -1.79,(AR) BAULCH 76 (A) 10U
O + H = OH    ,M7, A = 3.62E18, N = 1.0, B = 0.0, (AR) JENSEN 78 (B) 30U
END TBR REAX
O2 + H = O + OH , A = 2.2E14, N = 0.0, B = 16.8, BAULCH 72 (A) 1.5U
H2 + O = H + OH , A = 1.8E10, N = -1., B = 8.9, BAULCH 72 (A) 1.5U
H2 + OH = H2O + H , A = 2.2E13, N = 0.0, B = 5.15, BAULCH 72 (A) 2U
OH + OH = H2O + O , A = 6.3E12, N = 0.0, B = 1.09, BAULCH 72 (A) 3U
LAST REAX
THIRD BODY REAX RATE RATIOS
M1 = 25*H,4*H2,10*H2O,25*O,25*OH,1.5*O2,
M2 = 12.5*H,5*H2,17*H2O,12.5*O,12.5*OH,6*O2,
M3 = 12.5*H,5*H2,5*H2O,12.5*O,12.5*OH,11*O2,
M7 = 12.5*H,5*H2,5*H2O,12.5*O,12.5*OH,5*O2,
LAST CARD
$ODK
EP = 125,
$END
$TRANS
$END
$MOC
$END
$MABL
ADBATC= 0, NTQW=2, TQW=2*2000, XTQW=-1.E6,1.E6,
DXI=10E-4, NDXI=50, NYI=105, DCIMAX = .005, DXLIM(1) = .04,.75,
```

```

INNER = F,
OFC=1, DISTRB=0, XC0=-2.16, XCE=5.13,
$END
$MABL
ADBATC= 0, NTQW=2, TQW=2*2000, XTQW=-1.E6,1.E6,
DXI=10E-4, NDXI=50, NYI=105, DCIMAX = .005, DXLIM(1) = .04,.75,
INNER = T,
OFC=2, DISTRB=0, XC0=-2.16, XCE=5.13,
$END
0TITLE DEAN_contour100%
0DATA
$DATA
SCRJET = 1, PLANAR = F,
ODE = 1, ODK=1, TDK=1, MABL = 2, IMABL = 0, MABLK = T,
RSI = 2.084, RWTD = 0.05, RZERO = -1,
IWALL= 2, THETA = 25, RMAX = -0.01, ZMAX = 3.2,
LWALL = 1, THALW = 2.5, XLW(1) = 0, YLW(1) = -1.11, XCOWL = 0.1, ICOWL = 1,
JET = T, PINF = 0.1, MINF = 16.4, GINF = 1.4,
$END

```

C.2 TDK Performance Summary for the DEAN

```

1 TDK PERFORMANCE SUMMARY : DEAN_contour100%
*****FIRST TDK SOLUTION : WITH RAMP AND COWL BOUNDARY
LAYER*****

```

```

REAL WALL CONTOUR  1 ZONES          EXIT PLANE

```

```

FIRST
TDK/MABL SOLUTION

```

THRUST CHAMBER OPERATING CONDITIONS

CHAMBER PRESS [PSIA]	1739.000
CHAMBER TEMP [R]	6586.000
MIXTURE RATIO [-]	7.000000
H (OXID) [CAL/MOLE]	0.000000
H (FUEL) [CAL/MOLE]	0.000000
HCHAM (ODE) [BTU/LB]	-394.6774
DELH (AVERAGE) [BTU/LB]	0.000000
DELH1 (AVE) [BTU/LB]	0.000000

THRUST CHAMBER GEOMETRY

ECRAT [-]	4.000000
RI [-]	0.1000000E-01
THETA1 [DEGREES]	30.00000
RWTU [-]	1.000000
RSI [INCHES]	2.084000
RWTD [-]	0.5000000E-01
NIT [-]	248.0000
THE [DEGREES]	13.06846
THETA [DEGREES]	25.00000
EP (NOZZLE) [-]	1.000010

ASURF [IN**2] 41.76751

EXIT FLOW PROPERTIES

P (AXIS,EXIT) [PSIA] 324.6112
P (WALL,EXIT) [PSIA] 688.3699
T (WALL,EXIT) [R] 6363.542
V (WALL,EXIT) [FT/SEC] 14975.46
MA (WALL,EXIT) [-] 2.963189

ONE-DIMENSIONAL FLOW PERFORMANCE

ISP (ODE) [SECONDS] 509.8608
ISP (ODK) [SECONDS] 571.7090
ISP (ODF) [SECONDS] 509.8608
CSTAR (ODE) [FT/SEC] 0.0000
CSTAR (ODK) [FT/SEC] 1462.3
CSTAR (ODF) [FT/SEC] 0.0000

TWO-DIMENSIONAL FLOW PERFORMANCE

CD [-] 0.000000
CF (TDK) [-] 2.831902
CSTAR (TDK) [FT/SEC] 6302.546
THRUST (TDK) [POUNDS] 67192.85
WDOT (TDK) [LB/SEC] 121.1250
ISP (TDK) [SECONDS] 554.7396

BOUNDARY LAYER PARAMETERS

DFOPT (MABLK) [POUNDS] 1176.185
DF (MABLK) [POUNDS] 1025.826
DISP (MABLK) [SECONDS] 8.469148
THETA (EXIT) [INCH] 0.8708488E-03
DEL* (EXIT) [INCH] 0.9801783E-03
DEL* (THROAT) [INCH] 0.7956905E-03
EP (REGEN) [-] 1.222427
SQDOT (REGEN) [BTU/SEC] 6711.148
SQDOT (LOSS) [BTU/SEC] 0.000000
SUM QDOT [BTU/SEC] 6711.148
DH (SUM QDOT) [BTU/LBM] 55.40678

THRUST CHAMBER PERFORMANCE

THRUST (TC) [POUNDS] 66167.02
CF (TC) [-] 2.790799
WDOT (TC) [LB/SEC] 121.1250
ISP (TC) [SECONDS] 546.2704

1 TDK SCRAMJET SUMMARY : DEAN_contour100%

*****FIRST TDK SOLUTION : WITH RAMP AND COWL BOUNDARY
LAYER*****

THRUST ON THROAT PLANE (FX BE) = 61740.66 (LBF/FT)
THRUST ON EXHAUST NOZZLE (FX WALL) = 4867.923 (LBF/FT)

THRUST ON COWL (FX COWL) = -441.5600 (LBF/FT)
 TOTAL AXIAL THRUST (FX TOTAL) = 66167.02 (LBF/FT)
 RADIAL THRUST ON THROAT (FY BE) = 0.000000 (LBF/FT)
 RADIAL THRUST ON NOZZLE (FY WALL) = 0.000000 (LBF/FT)
 RADIAL THRUST ON COWL (FY COWL) = 0.000000 (LBF/FT)
 TOTAL RADIAL THRUST (FY TOTAL) = 0.000000 (LBF/FT)

COWL LENGTH (XCOWL) = 0.1736667E-01 (FEET)
 COWL LENGTH (XCOWL) = 0.1000000 (NONDIM)

XBAR WALL (XB WALL) = 0.000000 (FEET)
 XBAR WALL (XB WALL) = 0.000000 (NONDIM)
 WALL TORQUE (FY WALL)*(XBAR WALL) = 0.000000 (FT*LB/FT)
 YBAR WALL (YB WALL) = 0.000000 (FEET)
 YBAR WALL (YB WALL) = 0.000000 (NONDIM)
 WALL TORQUE (FX WALL)*(YBAR WALL) = 0.000000 (FT*LB/FT)

XBAR BRNR (XB BRNR) = 0.000000 (FEET)
 XBAR BRNR (XB BRNR) = 0.000000 (NONDIM)
 BRNR TORQUE (FY BRNR)*(YBAR BRNR) = 0.000000 (FT*LB/FT)
 YBAR BRNR (YB BRNR) = 0.000000 (FEET)
 YBAR BRNR (YB BRNR) = 0.000000 (NONDIM)
 BRNR TORQUE (FX BRNR)*(YBAR BRNR) = 0.000000 (FT*LB/FT)

XBAR COWL (XB COWL) = 0.000000 (FEET)
 XBAR COWL (XB COWL) = 0.000000 (NONDIM)
 COWL TORQUE (FY COWL)*(XBAR COWL) = 0.000000 (FT*LB/FT)
 YBAR COWL (YB COWL) = 0.000000 (FEET)
 YBAR COWL (YB COWL) = 0.000000 (NONDIM)
 COWL TORQUE (FX COWL)*(YBAR COWL) = 0.000000 (FT*LB/FT)

TOTAL TORQUE ABOUT THE EXIT PLANE = 0.000000 (FT*LB/FT)

PERCENTAGES OF THRUST COMPONENTS (RELATIVE TO AXIAL THRUST)
 THRUST ON THROAT PLANE (FX BE) = 93.31 %
 THRUST ON EXHAUST NOZZLE (FX WALL) = 7.36 %
 THRUST ON COWL (FX COWL) = -0.67 %
 RADIAL THRUST ON THROAT (FY BE) = 0.00 %
 RADIAL THRUST ON NOZZLE (FY WALL) = 0.00 %
 RADIAL THRUST ON COWL (FY COWL) = 0.00 %
 TOTAL RADIAL THRUST (FY TOTAL) = 0.00 %
 THRUST VECTOR ANGLE = 0.00 DEG

Appendix D : I_{sp} Calculation

This appendix shows a simple calculation to demonstrate the impact or I_{sp} hinted to in Chapter 1. Equation 19 is the change in velocity absent drag and gravity.

$$\Delta u = g_o I_{sp} \ln \frac{M_o}{M_b} \quad (19)$$

In Equation 19, Δu is the change in velocity, g_o is acceleration due to gravity, I_{sp} is the specific impulse, M_o is the initial mass, and M_b is the burnout mass or the mass at the end of the thrust period. Using the gross mass of the Centaur IIA 19,073 kg as the initial mass⁵¹, the empty mass of 2293 kg as the burn out mass⁵¹, and the stated I_{sp} of 449 s⁵¹, result is in a Δu of:

$$\Delta u = 9.81 \frac{m}{s^2} * 449s * \ln \frac{19073kg}{2293kg} = 9235 \frac{m}{s}$$

Now keeping the same Δu goal, same initial mass, but increasing the I_{sp} by one second yields a burn out mass of:

$$9235 \frac{m}{s} = 9.81 \frac{m}{s^2} * 450s * \ln \frac{19073kg}{M_b} \rightarrow M_b = 2354kg$$

In this analysis it is assumed the propellant mass is the initial mass minus the burn out mass. For the lower I_{sp} the propellant mass is 16,780 kg and for the higher I_{sp} the propellant mass is 16,719 kg. This less fuel is required to perform the same Δu maneuver with an increase in I_{sp} . The result is a savings of 61 kg (134.5 lbm). This weight savings can mean less fuel, as shown, or larger satellites.

Appendix E : Wall Temperatures

This section displays the results for different materials and their affect on the wall

temperature. Table 19 shows tested materials for the hydrogen wall,

Table 19 Hydrogen Wall Materials

	CVH1	CVH2	CVH3	CVH4	CVH5	CVH6	CVH7	CVH8
h_H	0.00437	0.007436	0.011791	0.006182	0.003611	0.003411	0.003332	0.003317
A_H (in²)	54.98	87.96	2.83	120.64	82.94	67.86	60.32	60.32
T_H (R)	6586.32	6586.32	6586.32	6586.32	6586.32	6586.32	6586.32	6586.32
h_C	0.197015	0.131318	0.115463	0.131837	0.147505	0.154929	0.154406	0.154432
A_C (in²)	32.97	65.94	2.2	90.43	52.74	37.68	30.14	30.14
T_C (R)	145.391	270.699	276.61	415.765	477.206	524.952	567.469	609.732
Q (Btu/s)	1439.05	3745.58	185.042	4328.38	1761.69	1349.22	1159.36	1146.54
t (in)	0.02	0.02	0.02	0.02	0.02	0.02	0.02	0.02
<i>Copper</i>								
k (Btu/sRin)	0.005377	0.005377	0.005377	0.005377	0.005377	0.005377	0.005377	0.005377
T_{wc} (R)	371.6508	703.1089	980.9731	771.1716	700.7632	753.2799	813.6587	853.1702
T_{wH} (R)	468.999	861.4854	1224.16	904.613	779.7623	827.2277	885.1436	923.8645
50% T_{melt}	1222.2	1222.2	1222.2	1222.2	1222.2	1222.2	1222.2	1222.2
<i>Silicon Carbide</i>								
k (Btu/sRin)	0.006571	0.006571	0.006571	0.006571	0.006571	0.006571	0.006571	0.006571
T_{wc} (R)	372.2814	705.1291	986.1016	772.5984	701.2952	753.792	814.1962	701.2952
T_{wH} (R)	451.948	834.7393	1185.118	881.8026	765.9455	814.3086	872.697	765.9455
50% T_{melt}	2790	2790	2790	2790	2790	2790	2790	2790
<i>Tungsten</i>								
k (Btu/sRin)	0.002333	0.002333	0.002333	0.002333	0.002333	0.002333	0.002333	0.002333
T_{wc} (R)	367.121	688.5986	944.1369	760.923	696.9423	749.6009	809.7983	696.9423
T_{wH} (R)	591.4695	1053.593	1504.586	1068.452	879.0035	920.021	974.5421	879.0035
50% T_{melt}	3294	3294	3294	3294	3294	3294	3294	3294
<i>Nickel</i>								
k (Btu/sRin)	0.001216	0.001216	0.001216	0.001216	0.001216	0.001216	0.001216	0.001216
T_{wc} (R)	359.7719	665.0572	884.3742	744.2957	690.7434	743.6322	803.5352	690.7434
T_{wH} (R)	790.1648	1365.266	1959.546	1334.263	1040.012	1070.568	1119.582	1040.012
50% T_{melt}	1555.2	1555.2	1555.2	1555.2	1555.2	1555.2	1555.2	1555.2

In Table 19, the important values are the hot-side wall temperature (T_{wH}) and the 50% melting temperature. As expected, the extreme T_{wH} is for the CVH3 element, which represents the throat. Table 19 indicates that all but the Nickel would meet the wall temperature criteria. Moreover, Table 19 shows how the temperature of the wall is affected by the thermal conductivity of the material (k). The oxygen side is presented in Table 20.

Table 20 Oxygen Wall Materials

	CVO1	CVO2	CVO3	CVO4	CVO5	CVO6
h_H	0.011217	0.005725	0.003248	0.003003	0.002891	0.002833
A_H (in²)	3.14	165.88	180.96	108.96	180.96	180.96
T_H (R)	6586.32	6586.32	6586.32	6586.32	6586.32	6586.32
h_C	0.087317	0.062727	0.053795	0.049671	0.046118	0.03672
A_C (in²)	1.57	90.43	105.5	105.5	105.5	105.5
T_C (R)	179.391	303.911	379.602	452.208	531.483	616.862
Q (Btu/s)	177.326	5107.5	3305.34	3019.91	2859.56	2702.71
t (in)	0.02	0.02	0.02	0.02	0.02	0.02
<i>Copper</i>						
k (Btu/sRin)	0.005377	0.005377	0.005377	0.005377	0.005377	0.005377
T_{wc} (R)	1446.081	1188.386	955.7072	806.6633	1113.574	1308.098
T_{wH} (R)	1656.12	1302.903	1023.642	909.7455	1172.346	1363.647
50% T_{melt}	1222.2	1222.2	1222.2	1222.2	1222.2	1222.2
<i>Silicon Carbide</i>						
k (Btu/sRin)	0.006571	0.006571	0.006571	0.006571	0.006571	0.006571
T_{wc} (R)	1453.879	1191.369	956.8652	807.7637	1114.61	1309.278
T_{wH} (R)	1625.768	1285.086	1012.461	892.1228	1162.707	1354.737
50% T_{melt}	2790	2790	2790	2790	2790	2790
<i>Tungsten</i>						
k (Btu/sRin)	0.002333	0.002333	0.002333	0.002333	0.002333	0.002333
T_{wc} (R)	1390.07	1166.962	947.3899	798.7596	1106.13	1299.628
T_{wH} (R)	1874.125	1430.879	1103.952	1036.323	1241.577	1427.645
50% T_{melt}	3294	3294	3294	3294	3294	3294

Table 20 cont.

<i>Nickel</i>						
k (Btu/sRin)	0.001216	0.001216	0.001216	0.001216	0.001216	0.001216
T_{wc} (R)	1299.199	1132.204	933.8958	785.9367	1094.054	1285.886
T_{wh} (R)	2227.816	1638.505	1234.246	1241.681	1353.897	1531.476
50% T_{melt}	1555.2	1555.2	1555.2	1555.2	1555.2	1555.2
<i>Cobalt</i>						
k (Btu/sRin)	0.00133	0.00133	0.00133	0.00133	0.00133	0.00133
T_{wc} (R)	1299.199	1132.204	933.8958	785.9367	1094.054	1285.886
T_{wh} (R)	2148.247	1595.122	1208.51	1202.63	1331.632	1510.432
50% T_{melt}	1592.1	1592.1	1592.1	1592.1	1592.1	1592.1

Table 20 shows how T_{wh} at the throat, CVO1, excited the 50% melting point for not only copper, but nickel and cobalt as well. Of the materials shown only silicon carbide and tungsten meet the requirements due to their high melting points.

References

-
- ¹ D. DeGeorge & S. Fletcher “The Integrated High Payoff Rocket Propulsion Technology Program and Tactical Missile Propulsion Status”, AFRL-PR-EN-TP-2002-214
- ² Futron Corporation (2006, Sept. 6) “Space Transportation Costs: Trends in Price Per Pound to Orbit 1990-2000”, Retrieved Oct. 26, 2007, from http://www.futron.com/pdf/resource_center/white_papers/FutronLaunchCostWP.pdf
- ³ “RL10B-2”, Pratt & Whitney Rocketdyne, pwr_RL10B-2.pdf, 2005
- ⁴ T. Rudman & D. Del Duca, “Evolution of the Titan IV Launch Vehicle and Propulsion System”, AIAA Paper, 1998-3194.
- ⁵ B. Free, J. Owens, & F. De Poli, “THREE-BURN CENTAUR WITH ELECTRIC PROPULSION UPPER STAGE DELIVERS MAXIMUM PAYLOAD”, AIAA Paper 2002-3968.
- ⁶ R.W. Humble, G.N. Henry, & W. J. Larson, *Space Propulsion Analysis and Design*, 1995, McGraw-Hill Inc, New York, p.128-138.
- ⁷ P. Hill, & C. R. Peterson, *Mechanics and Thermodynamics of Propulsion*, second edition, 1992, Addison-Wesley Publishing Company, p. 124–130.
- ⁸ D.K. Huzel., & D.H. Huang, *Modern Engineering for Design of Liquid-Propellant Rocket Engines*, Vol. 147, 1992, AIAA, p. 84–104.
- ⁹ S.A. Rahman, & R.J. Santoro, “A Review of Coaxial Gas/Liquid Spray Experiments and Correlations”, AIAA Paper 94-2772, 1994.
- ¹⁰ M.D.A. Lightfoot, S.A. Danczyk, & D.G. Talley, “Atomization in Gas-Centered Swirl-Coaxial Injectors”, DETIC Paper 50260548, 2006.
- ¹¹ G.A. Dressler, & J.M. Bauer, “TRW Pintle Engine Heritage and Performance Characteristics”, AIAA Paper 2000-3871, 2000.
- ¹² R.D. Woodward, K.L. Miller, V.G. Bazarov, G.F. Guerin, S. Pal, & R.J. Santoro, “Injector Research for Shuttle OMS Upgrade Using LOX/Ethanol Propellants”, AIAA Paper 98-3816, 1998.
- ¹³ G. Hagemann, H. Immich, T. Van Nguyen, & G. Dumnov, “Advanced Rocket Nozzles”, *Journal of Propulsion and Power* Vol. 14, No. 5, September-October 1998.
- ¹⁴ G. Hagemann, H. Immich, & M. Terhardt, “Flow Phenomena in Advanced Rocket Nozzles - Plug Nozzle”, DLR-74239/D-81663, 1998.
- ¹⁵ T. Ito, K. Fujii, & A. Hayashi, “Computations of the Axisymmetric Plug Nozzle Flow Fields – Flow Structures and Thrust Performance”, AIAA paper 99-3211, 1999.
- ¹⁶ T. Ito, & K. Fujii, “Flow Field Analysis of the Base Region of Axisymmetric Aerospike Nozzles”, AIAA Paper 2001-1051, 2001.
- ¹⁷ F. Nasuti, & M. Onofri, “Analysis of In-Flight Behavior of Truncated Plug Nozzles”, AIAA Paper 2000-3289, 2000.
- ¹⁸ T. Ito, & K. Fujii, “Numerical Analysis of the Base Bleed Effect on the Aerospike Nozzles”, AIAA Paper 2002-0512, 2002.
- ¹⁹ Incropera, DeWitt, Bergman, & Lavine, *Fundamentals of Heat and Mass Transfer*, sixth edition, 2007, John Wiley & Sons, Inc.
- ²⁰ U.H. Von Glahn, “Correlation of Gas-Side Heat Transfer for Axisymmetric Rocket Engine Nozzles”, NASA TM X-1748, 1969.
- ²¹ R.L. Schacht, R.J. Quentmeyer, & W.L. Jones, “Experimental Investigation of Hot-Gas Side Heat-Transfer Rate for a Hydrogen-Oxygen Rocket”, NASA TN D-2832, 1965.
- ²² D.R. Boldman, J.F. Schmidt, & A.K. Gallagher, “Laminarization of a Turbulent Boundary Layer as Observed from Heat-Transfer and Boundary-Layer Measurements in Conical Nozzles”, NASA TN D-4788, 1968.
- ²³ R. Quentmeyer, & E. Roncace, “Hot Gas Side Heat Transfer Characteristics of a Subscale Plug Nozzle Rocket Calorimeter Chamber,” NASA Technical Paper 3380, 1993.
- ²⁴ D. Preclik, D. Wiedmann, W. Oechslein, & J. Kretschmer, “Cryogenic Rocket Calorimeter Chamber Experiments and Heat Transfer Simulations”, AIAA Paper 1998-3440, 1998.

-
- ²⁵ Jong-Gyu Kim, Kwang-Jin Lee, Seonghyeon Seo, Yeoung-Min Han, Hong-Jip Kim, & Hwan-Seok Choi, "Film Cooling Effects on Wall Heat Flux of a Liquid Propellant Combustion Chamber", AIAA Paper 2006-5196, 2006.
- ²⁶ M.H. Naragi, S. Dunn, & D. Coats, "DUAL REGENERATIVE COOLING CIRCUITS FOR LIQUID ROCKET ENGINES", AIAA 2006-4367, 2006.
- ²⁷ M.J. Chiaverini, J.A. Sauer, & S.M. Munson, "Laboratory Characterization of Vortex-Cooled Thrust Chambers for Methane/O₂ and H₂/O₂", AIAA 2005-4131, 2005.
- ²⁸ H. Immich, & M. Caporicci, "STATUS OF THE FESTIP ROCKET PROPULSION TECHNOLOGY PROGRAMME", AIAA Paper, 1997.
- ²⁹ G. Schmidt, M. Popp, & Th. Frohlich, "Design Studies for a 10 Ton Class High Performance Expander Cycle Engine", AIAA Paper 1998-3673, 1998.
- ³⁰ R. Sorge, C. Carmicino, & A. Nocito, "Design of a Lab-Scale Cooled Two-Dimensional Plug Nozzle for Experimental Tests", AIAA Paper 2002-4039, 2002.
- ³¹ A. Kumakawa, T. Tomita, & H. Sakamoto, "A Study of Plug-Nozzle Rocket Calorimeters", AIAA paper 96-2583, 1996.
- ³² T.S. Wang, "Analysis of Linear Aerospikes Plume Induced Base-Heating Physics and Fence Effect", AIAA Paper 99-3682, 1999.
- ³³ S. Tsutsumi, K. Yamaguchi, S. Teramoto, & T. Nagashima, "Clustering Effects on Performance and Heating of a Linear Aerospikes Nozzle", AIAA Paper 2007-122, 2007.
- ³⁴ S. Peer & A. Minick, "Design and Development of an Advanced Expander Combustor", AIAA 98-3675, 1998.
- ³⁵ L. Schoenman, "4000°F Materials for Low Thrust Rocket Engines", AIAA 93-2406, 1993.
- ³⁶ A. Kumakawa, T. Onodera, M. Yoshida, M. Atsumi, & I. Igarashi, "A STUDY OF AEROSPIKE-NOZZLE ENGINES", AIAA Paper 98-3526, 1998.
- ³⁷ P.W. Gloyer, W.H. Knuth, & R.A. Crawford, "Oxygen Rich Gas Generator Design and Performance Analysis", AIAA Paper 93-2159, 1993.
- ³⁸ W. Brown, "Enhanced Heat Transfer Rocket Combustor Technology Component Hot-Fire Test Results", AIAA Paper 90-2182, 1990.
- ³⁹ J. Carlile, "An Experimental Investigation of High-Aspect-Ratio Cooling Passages", AIAA 92-3154, 1992.
- ⁴⁰ M.F. Wadel, & M.L. Meyer, "Validation of high aspect ratio cooling in a 89 kN (20,000 lbf) thrust combustion chamber", AIAA 96-2584, 1996.
- ⁴¹ F. Neuner, D. Preclik, M. Popp, M. Funke, & H. Kluttig, "Experimental and Analytical Investigation of Local Heat Transfer in High Aspect Ratio Cooling Channels", AIAA 98-3439, 1998.
- ⁴² R. Schuff, M. Maier, O. Sindiy, C. Ulrich, & S. Fugger, "Integrated Modeling and Analysis for a LOX/Methane Expander Cycle Engine: Focusing on Regenerative Cooling Jacket Design", AIAA 2006-4534, 2006.
- ⁴³ "NPSS User Guide", NASA Glenn Research Center, Cleveland, OH, version 5, 30 May, 2006.
- ⁴⁴ S.S. Dunn & D.E. Coats, "TDK'04™ Two-Dimensional Kinetics (TDK) Nozzle Performance Computer Program User's Manual", Software & Engineering Associates, Inc. January 2005.
- ⁴⁵ L. Schoenman, "Final Report Oxygen Materials Compatibility Testing", NASACR-182195, January 1989.
- ⁴⁶ N.M. Laurendeau, "The Ignition Characteristics of Metals in Oxygen Atmosphere", NASA Technical Report No. 851, October 1968.
- ⁴⁷ M.A. Arguello, "The Conceptual Design of a Split Flow Liquid Hydrogen Turbopump", AFIT Thesis, March 2008.
- ⁴⁸ W.S. Strain, "Design of an Oxygen Turbopump for Dual Expander Cycle Rocket Engine", AFIT Thesis, March 2008.
- ⁴⁹ "Thermophysical Properties of Fluid Systems", National Institute of Standards and Technology, Retrieved Jan. 28, 2008, from <http://webbook.nist.gov/chemistry/fluid/>, 2005.

⁵⁰ M.H. Jaskowiak, S.K. Elam, & M.R. Effinger, “Lightweight, Actively Cooled Ceramic Matrix Composite Thrustcells Successfully Tested in Rocket Combustion Lab”, NASA Glenn and NASA Marshall.

⁵¹ Mark Wade, “Centaur IIA”, Encyclopedia Astronautics, Retrieved Feb. 1, 2008, from <http://www.astronautix.com/stages/cenuriia.htm>, 2007.

Vita

2Lt David F. Martin II graduated with the class of 2006 from Embry-Riddle Aeronautical University (ERAU) Prescott, AZ campus. There he completed the world-renowned aerospace engineering program, ending with a Bachelors of Science in aerospace engineering and a Minor in math and defense studies. As a college student, he was a member of the aeronautical honor society Sigma Gamma Tau. For the final design project, he was a member of a group to be the first to design and fly a student built UAV at ERAU.

2Lt Martin was commissioned through Detachment 028 at ERAU Prescott. After completing the Air and Space Basic Course (ASBC), his first assignment was at the Air Force Institute of Technology beginning in August 2006. Upon graduation, he will be assigned to the 0029 Intel Squadron at Ft. Meade Army Base, Maryland.

REPORT DOCUMENTATION PAGE				Form Approved OMB No. 074-0188	
<p>The public reporting burden for this collection of information is estimated to average 1 hour per response, including the time for reviewing instructions, searching existing data sources, gathering and maintaining the data needed, and completing and reviewing the collection of information. Send comments regarding this burden estimate or any other aspect of the collection of information, including suggestions for reducing this burden to Department of Defense, Washington Headquarters Services, Directorate for Information Operations and Reports (0704-0188), 1215 Jefferson Davis Highway, Suite 1204, Arlington, VA 22202-4302. Respondents should be aware that notwithstanding any other provision of law, no person shall be subject to a penalty for failing to comply with a collection of information if it does not display a currently valid OMB control number.</p> <p>PLEASE DO NOT RETURN YOUR FORM TO THE ABOVE ADDRESS.</p>					
1. REPORT DATE (DD-MM-YYYY) 14-03-2008		2. REPORT TYPE Master's Thesis		3. DATES COVERED (From – To) March 2002 – March 2003	
4. TITLE AND SUBTITLE COMPUTATIONAL DESIGN OF UPPERSTAGE CHAMBER, AEROSPIKE, & COOLING JACKET FOR DUAL-EXPANDER ROCKET ENGINE				5a. CONTRACT NUMBER	
				5b. GRANT NUMBER	
				5c. PROGRAM ELEMENT NUMBER	
6. AUTHOR(S) Martin, David F., 2Lt, USAF				5d. PROJECT NUMBER	
				5e. TASK NUMBER	
				5f. WORK UNIT NUMBER	
7. PERFORMING ORGANIZATION NAMES(S) AND ADDRESS(S) Air Force Institute of Technology Graduate School of Engineering and Management (AFIT/EN) 2950 Hobson Way, Building 640 WPAFB OH 45433-8865				8. PERFORMING ORGANIZATION REPORT NUMBER AFIT/GAE/ENY/08-M20	
9. SPONSORING/MONITORING AGENCY NAME(S) AND ADDRESS(ES) Mr. Michael Huggins Building: 8353 Room: 216B 5 Pollux Drive, Edwards CA 93524				10. SPONSOR/MONITOR'S ACRONYM(S)	
				11. SPONSOR/MONITOR'S REPORT NUMBER(S)	
12. DISTRIBUTION/AVAILABILITY STATEMENT APPROVED FOR PUBLIC RELEASE; DISTRIBUTION UNLIMITED.					
13. SUPPLEMENTARY NOTES					
14. ABSTRACT <p>To increase the performance of the current US satellite launch capability, new rocket designs must be undertaken. One concept that has been around since the 50s but yet to be utilized on a launch platform is the aerospike, or plug nozzle. The aerospike nozzle concept demonstrates globally better performance compared to a conventional bell nozzle, since the expansion of the jet is not bounded by a wall and therefore can adjust to the environment by changing the outer jet boundary. A dual-expander aerospike nozzle (DEAN) rocket concept would exceed the Integrated High Payoff Rocket Propulsion Technology initiative (IHPRPT) phase three goals. This document covers the design of the chamber and nozzle of the DEAN. The validation of the design of the DEAN are based on the model in Numerical Propulsion System Simulation (NPSSTM), added with the nozzle design from Two-Dimensional Kinematics (TDK 04TM). The result is a rocket engine that produces 57,231 lbf (254.5 kN) of thrust at an I_{sp} of 472 s. Additionally, the oxygen wall is made of silicon carbide, with a melting point of 5580 R (3100 K), and has a maximum temperature at the throat of 1625 R (902 K). The hydrogen side is made of copper, with a melting point of 2444 R (1358 K), and has a maximum wall temperature of 1224 R (680 K) at the throat. Based on these result, future investigation into this design is merited since it has the potential to save \$19 million in the cost to launch a satellite. NPSS proved to be a powerful tool in the development of rocket engines. TDK, however, was left wanting in the area of aerospike design.</p>					
15. SUBJECT TERMS Aerospike, Plug Nozzle, Regenerative Cooling, Expander Cycle, Cooling Channels, NPSS, TDK					
16. SECURITY CLASSIFICATION OF:			17. LIMITATION OF ABSTRACT	18. NUMBER OF PAGES	19a. NAME OF RESPONSIBLE PERSON
a. REPORT	b. ABSTRACT	c. THIS PAGE			Richard Branam, Maj, USAF
U	U	U	UU	135	19b. TELEPHONE NUMBER (Include area code) (937) 255-3636 ext. 4559 (richard.branam@afit.edu)